Aus dem Bereich Biophysik
Theoretische Medizin und Biowissenschaften
der Medizinischen Fakultät
der Universität des Saarlandes, Homburg/Saar

ORGANIC ELECTROCHEMICAL TRANSISTORS BASED ON PEDOT:PSS FOR THE SENSING OF CELLULAR SIGNALS FROM CONFLUENT CELL LAYERS DOWN TO SINGLE CELLS

Dissertation
zur Erlangung des Grades eines
Doktors der Naturwissenschaften

der medizinischen Fakultät
der UNIVERSITÄT DES SAARLANDES
2019

vorgelegt von
Felix Wolfgang Hempel
geb. am 29.03.1988 in Lahr

Homburg 2019

Dekan: Prof. Dr. Menger

Erstgutachter: Prof. Dr. Hoth

Zweitgutachter: Prof. Dr. Lipp

Tag der mündlichen Prüfung: 09.06.2020

For my beautiful daughter

Table of Contents

Abbreviations

AFM ..... *Atomic force microscope*
$A_{Source/Drain}$ ..... *Area of the source or drain contact lines*
bpm ..... *Beats per minute*
c… ..... *Concentration*
$CaCl_2$ ..... *Calcium chloride*
C_b… ..... *Bulk capacitance*
C_d… ..... *Contact line capacitance*
C_{Drain} ..... *Capacitance of the drain*
C_{FM}… ..... *Capacitance of the free membrane*
C_{JM} ..... *Capacitance of the junction membrane*
C_M ..... *Membrane capacitance*
C_P… ..... *Pipette capacitance*
C_{Source} ..... *Capacitance of the source*
$C_{Source/Drain}$ ..... *Parasitic capacitance of the source and drain contact lines*
d… ..... *Thickness of the passivation layer*
DI… ..... *Deionized*
D_{K+} ..... Diffusion coefficient of potassium
e_0… ..... Elementary charge
E^{Ca}… ..... *Nernst potential calcium*
ECIS ..... *Electric cell-substrate impedance sensor*
EG ..... *Ethylene glycol*
EGTA ..... *Ethylene glycol-bis(2-aminoethylether)-N,N,N',N'-tetraacetic acid*
E_i… ..... *Nernst potential for the ions*
E^K… ..... *Nernst potential potassium*
E^L… ..... *Nernst potential for the leakage*
E^{Na}… ..... *Nernst potential sodium*
f… ..... *Frequency*
FET ..... *Field-effect transistor*
f_g… ..... *Cutoff frequency of the operational amplifier*
FM… ..... *Free membrane of the cell*
G^{Ca} ..... *Specific ion conductance calcium*
G^i… ..... *Conductance of the ions*
G_J… ..... *Junction conductance*
G^K ..... *Specific ion conductance potassium*
G^L… ..... *Conductance of the leakage*
$g_{m...}$ ..... *Tranconductance*
G^{Na} ..... *Specific ion conductance sodium*
GOPS ..... *(3-Glycidyloxypropyl)trimethoxysilane*
h… ..... Cleft height
H… ..... *Transfer function*
HEK ..... *Human embryo kidney cells*

HL-1 ..... *Cardiac muscle cells*
I… ..... *Ionic strength*
I_0… ..... Modified Bessel function
IDE ..... *Interdigitated electrode*
I_{DS} ..... *Drain-source current*
I_{GS} ..... *Gate-source current*
I_p… ..... *Current source of the cell membrane*
j… ..... *Imaginery unit*
JM… ..... *Junction membrane of the cell*
k_B… ..... Boltzmann constant
KCl ..... *Potassium chloride*
L_D… ..... Debye length
MDCK ..... *Madin-Darby canine kidney cells*
MEA ..... *Microelectrode array*
$MgCl_2$ ..... *Magnesium chloride*
N_A ..... *Avogadro's number*
NaCl ..... *Sodium chloride*
n_{tot}^B ..... Ion density of surrounding bath solution
OECTs ..... *Organic electrochemical transistors*
ONO ..... *Layer of oxide-nitride-oxide*
PBS ..... *Phosphate buffered saline*
PDMS ..... *Polydimethylsiloxane*
PEDOT ..... *poly(3,4-ethylenedioxythiophene)*
PEDOT:PSS ..... *Poly(3,4-ethylenedioxythiophene) polystyrene sulfonate*
PSS ..... *polystyrene sulfonate*
r… ..... Cell radius
Ra ..... *Arithmetic average of absolute values of surface height deviations*
R_D ..... *Diffusion resistance*
R_{Drain} ..... *Resistance of the drain*
R_{DS} ..... *Output resistance*
R_{el} ..... *Combined resistance of the reference electrode and the electrolyte*
$R_{feedback}$ ..... *Feedback resistance*
$R_{J...}$ ..... *Junction resistance*
rpm ..... *Revolutions per minute*
Rq ..... *Root mean square average of height deviation*
R_S… ..... *Series resistance of the pipette*
R_{Seal} ..... *Seal resistance*
R_{Source} ..... *Resistance of the source*
T… ..... Temperature
TC ..... *Transfer characteristics*
t_D… ..... *Diffusional time constant*
TTF ..... *Transistor-transfer function*
UV… ..... *Ultraviolet*
V_1… ..... *Voltage across the contact line capacitance*
V_{DS} ..... *Drain-source voltage*
V_{GS} ..... *Gate-source voltage*

V_{in} ..... *Input voltage*
V_J ..... *Junction potential of the cell*
V_M ..... *Intracellular voltage*
V_{out} ..... *Output voltage*, *Output voltage*
V_S ..... *Source voltage*
w ..... *Angular frequency*
z ..... *Valency of the ions*
Z ..... *Impedance*
Z_W ..... *Warburg element*
ε_0 ..... *Absolute permittivity of the vacuum*, *Permittivity of the vacuum*
ε_{0x} ..... *Relative permittivity of the silicon dioxide passivation*
ε_r ..... *Dielectric constant*

Abstract

Summary:

Organic electrochemical transistors based on the polymer poly(3,4-ethylenedioxythiophene) polystyrene sulfonate (PEDOT:PSS) are biosensors which use the movement of cations into and out of the polymer layer to generate a behavior that mimics p-type transistors. The device configuration has a source contact, a drain contact, and a gate electrode, which is separated from the polymer layer by an electrolyte. The cations of the electrolyte enter the PEDOT:PSS and compensate the pendant sulfonate anions on the PSS which increases the hole density in PEDOT. This results in a decrease of the drain current and a switching of the device into the off state. Using this device behavior, several biological signals can be detected. The OECTs can be used for the detection of action potentials of electrogenic cells, but also enable the measurement of the adhesion of cells to the device. The utilization of these devices for the measurement of confluent cell layers down to single cells in combination with a mathematical description was not shown so far.

Results:

In order to achieve versatile, highly sensitive, and transparent sensors, the fabrication of the devices with standard cleanroom processes was established in a unique and simplified way. Deteriorating factors such as exposure to ultraviolet radiation and contact with water were eliminated from the fabrication process. The sensors were characterized in regards to their electrical performance and stability in dry and wet conditions. The gathered results were used to generate a protocol for the best performing chips. Based on the generated data protocols for the fabrication, chemical post-treatment, as well as device operation, were established. Different sensing areas of the polymer layer were tested to determine their advantages for biosensing. The crucial factor for the devices was based on the volume of the deposited polymer layer. By keeping the volume of the PEDOT:PSS constant the transconductance remains the same, however thicker PEDOT:PSS layers resulted in devices with a comparatively lower cutoff frequency while thinner polymer layers resulted in a comparatively higher cutoff frequency. Therefore, an optimized chip layout had to be made to guarantee the functionality of the devices for their applications. Different cell types were used to test the devices towards their cell-sensing capabilities. Cardiomyocytes were used to establish the sensors for action potential measurements, and it was found that the sensors inherit a high signal-to-noise ratio making these devices ideal candidates for

action potential measurements. At the same time, the impedimetric capabilities of the devices were investigated according to transistor-transfer function measurements which were not shown before with PEDOT:PSS based organic electrochemical transistors. By using densely growing cells, such as the Madin-Darby canine kidney cells, the change in impedance spectra towards changes in gap junction resistance could be proven. Human embryo kidney cells were used to investigate the behavior of dense cell cultures when no gap junctions are present. Since the observation of dense cellular cultures only allows for experiments on an arbitrary amount of cells, a protocol was established, and the devices were tested for measurements on a single cell level. The devices showed the capability for measurements of action potentials with the additional impedimetric data in high precision and reproducibility. Devices utilizing transistor-transfer function measurements with organic electrochemical transistors down to single cell level have not been shown so far. In addition, a new mathematical model was developed in order to calculate the cell-related parameters which demonstrate the distance between the cell and the polymer, offering a closer insight into the cellular attachment and detachment behavior. In combination with the fitting, the present platform was established with several possible applications ranging from confluent cells down to single cells while also offering the possibility of optically controlling the cell behavior due to the transparency of the devices.

Outlook:

The established devices offer an excellent biosensing platform which can be used in several future applications. The devices are not limited to the shown applications and can be altered to fit the desired use.

Zusammenfassung

Einleitung:

Organisch elektrochemische Transistoren basierend auf dem Polymer poly(3,4-ethylenedioxythiophene) polystyrene sulfonate (PEDOT:PSS) sind Biosensoren, welche p-Typ Transistor Charakteristika zeigen basierend aus der Bewegung von Kationen in und aus der Polymerschicht. Die Sensorkonfiguration besteht aus drei Kontakten: der Source, dem Drain und der Gate-Elektrode, wobei die Polymerschicht durch einen Elektrolyten von der Gate-Elektrode getrennt ist. Die Kationen aus dem Elektrolyten werden durch die angelegte Spannung in das PEDOT:PSS geleitet, wo sie die offenen Sulfonat-Anionen des PSS kompensieren. Dies wiederum erhöht die Dichte der Löcher im PEDOT, was zu einem Abfall des Drain-Stroms führt. Dieser Stromabfall resultiert in der Ausschaltung des Sensors. Dieses Sensorverhalten kann für die unterschiedlichsten biologischen Messungen verwendet werden. Die OECTs können für die Detektion von elektrisch aktiven Zellen genutzt werden und erlauben gleichzeitig auch die Messung der Zelladhäsion. Die Nutzung dieser Sensoren für die Messung von Daten aus konfluenten Zellschichten bis zu Einzelzellmessungen in Kombination mit einer mathematischen Beschreibung der Ergebnisse wurde bisher noch nicht gezeigt.

Ergebnisse:

Um universal einsetzbare, hoch-sensitive und transparente Sensoren zu produzieren, wurden etablierte Reinraumprozesse in neuer und vereinfachter Weise genutzt. Faktoren die während der Sensorherstellung zu Schädigungen der Polymerschicht führen könnten, wie z.B. Ultraviolettstrahlung, wurden komplett eliminiert. Die Sensoren wurden bezüglich ihrer elektrischen Fähigkeiten und ihrer Stabilität in nassen sowie trockenen Umständen getestet. Das Testverfahren ermöglichte die Festsetzung der optimalen Parameter für die Herstellung der organisch elektrochemische Transistoren. Als wichtigster Faktor für das Sensorverhalten wurde das Volumen der Polymerschicht bestimmt. Das Volumen des PEDOT:PSS bestimmt die elektrischen Eigenschaften der Sensoren. Bleibt das Volumen der Polymerschicht für die Sensoren konstant, so wird die gleiche Transkonduktanz gemessen, eine Änderung in der Schichtdicke führt jedoch zu einem andern Verhalten bezüglich der Grenzfrequenz. Dünnere Schichten zeigen eine Erhöhung der Grenzfrequenz, wobei dickere Schichten einen gegenteiligen Effekt zeigen. Aus diesem Grund musste ein optimiertes Design erstellt werden, um die richtige Funktion der Sensoren für die

geplanten Experimente zu gewährleisten. Unterschiedliche Zelltypen wurden genutzt, um ein breites Spektrum an Anwendungen für die fabrizierten Sensoren zu testen. Herzzellen wurden für die Messung von extrazellulären Aktionspotenzialen eingesetzt. Die getesteten Sensoren zeigten ein sehr gutes Signal-Rausch-Verhältnis mit schnellen Messzeiten, was sie zu idealen Sensoren für Aktionspotenzialmessungen macht. Zur selben Zeit wurden Transistor-Transferfunktionsmessungen durchgeführt, um die Fähigkeiten der Sensoren im Bereich der Impedanzmessungen zu ergründen. Diese Art von Messungen wurde bisher noch nicht publiziert. Durch die Verwendung von dicht wachsenden Madin-Darbey Kidney Zellen konnte die Änderung der Zellimpedanz durch Änderungen in den Zellverbindungen gemessen werden. Im Gegensatz zu den Madin-Darbey Kidney Zellen wachsen Human Embryo Kidney Zellen ohne Zellverbindungen. Da die Messung von dichten Zellkulturen nur Aussagen über die Population von Zellen als Ganzes erlaubt, wurden neue Protokolle entwickelt, um auf Einzelzelllevel zu messen. Die organisch elektrochemische Transistoren zeigten die Fähigkeit, Aktionspotenziale von Zellen sowie deren Adhäsion mit hoher Reproduzierbarkeit und Präzision zu messen. Organisch elektrochemische Transistoren, die die Transistor-Transferfunktion bis hinunter auf Einzelzellebene nutzen wurden bisher noch nicht gezeigt. Zusätzlich wurde ein mathematisches Modell entwickelt, um die Zellparameter aus den gewonnenen Daten zu ermitteln. Das mathematische Modell dient dabei der Verbesserung des Verständnisses bezüglich der Interaktion von Zellen und den Sensoren. Die Kombination aus den gezeigten Biosensoren mit optischer Transparenz und der Möglichkeit des mathematischen Fittens der Daten erlauben die Möglichkeit für unzählige Experimente.

Ausblick:

Die gezeigten Sensoren bieten eine exzellente Plattform für die Biosensorik mit der Möglichkeit für viele zukünftige Anwendungen. Die Sensoren sind dabei nicht auf die gezeigten Anwendungen limitiert, sondern können mit einfachen Mitteln für die unterschiedlichsten Zwecke angepasst werden.

1 Introduction

1.1 Biosensors

Biosensors are analytical devices, which use biological, or biologically derived, recognition systems integrated with a type of transducer. The recognition system reacts specifically to an analyte, generating a biological signal, which can be transformed into an electrical signal by the transducer (LOWE, 2007). Ideally, the response of the biosensor is highly specific, fast, in real-time, and reproducible. Other features biosensors can possess include reusability, ease of fabrication, cost-efficient manufacturing, multiplexing, and others. While biosensors can be used in many fields, their operational principle is the same. In general, a biologic recognition system is a biological component which enables the detection of a specific analyte, such as cells, enzymes, antibodies, DNA, organelles, tissues, and others. The presence of the analyte causes changes in the recognition system in the form of pH, currents, charges, magnetic fields, heat, or deformation of the biological component. These changes can be converted into electrical signals by the transducer and are then measured and observed by the readout electronics. This means that the transducer is just as important to the biosensor system as the biological components. The transducer has to be able to detect whichever biological signal is desired from the system and has to be able to convert these signals in a way that a readout system can use the electronic information. The relation between the biological recognition element and the transducer is rather complex and can be researched as an individual field of study. Biosensors can be categorized based on their biological recognition element and the used transducer principle (PERUMAL, HASHIM, 2014). Typically used bioreceptors are enzymes, antibodies, DNA, cells, and biomimetics, while the most common transducer principles for biosensors are based on electrochemical, piezoelectric, calorimetric, thermal, and optical reactions. However, this categorization is quite basic, since by now several biosensors have been developed, which are able to use a combination of the mentioned categories in order to increase sensitivity or boost versatility (CUNNINGHAM et al., 2002; LEI et al., 2004; LUCARELLI et al., 2008). Of course, even within the mentioned categories, there are still more distinctions to be made between individual sensors since different sensor principles use combinations of biological materials and transducers. Another leading force in this process is the

development of so-called new material biosensors in which nanomaterials or other materials are used in a new way to achieve high sensitivity biosensors with phenomenal properties (BALASUBRAMANIAN, BURGHARD, 2006; KERGOAT et al., 2012). Biosensors utilize some materials in the nanometer range where completely different surface properties apply. It is also possible to push to way higher sensitivities when applying new materials by increasing the conductivity or reducing the sheet resistance etc. Many new devices are being investigated every year, which leads to a very competitive field of research.

In the case of cell-based biosensors living cells, either primary cells or immortalized cell lines, are immobilized on the devices and combined with different transducers. Typically cell-based biosensors are used to detect intracellular and extracellular signals and activities such as cell migration and physiological parameters as the reaction of the cells towards stimuli. Many applications for these kinds of sensors have been shown in recent years. These sensors have been shown for the use in biomedicine (WANG et al., 2005b), pharmaceutical screening (ASPHAHANI, ZHANG, 2007), environmental sensing (XIE et al., 2004), food analysis (VERMA, SINGH, 2003) and more. Because of that, the sensors have been established as powerful tools.

Some of the most commonly used devices for cell-based biosensors today include field-effect transistors (FETs), microelectrode arrays (MEAs), electric cell-substrate impedance sensors (ECIS), surface plasmon resonance etc. (LIU, WANG, 2009). While cell-based biosensors, just as other biosensors, rely on high selectivity, high specificity, fast operation time, and reliability, the use of living cells shows to be a completely different challenge to the use of biological components (WANG et al., 2005a; ZIEGLER, 2000). Naturally, biocompatibility is one of these factors determining the success of a cell-based biosensor (DING et al., 2008; LAN et al., 2005). If the transducer material of the sensor does not show good biocompatibility, the required cell coupling cannot occur. While the base material might not show sufficient biocompatibility, a modification of the surface has to be an option for cells to attach to the sensor. Another valuable property might be the transparency of the device. Many assays work with fluorescently labeled components, e.g., live-dead assays (NILES et al., 2007), where transparency would greatly benefit the electrical readout since the data can be confirmed optically. It is worth noting, that while there are also options for uplight measurements of fluorescence, the vast majority of fluorescence scanners operates with inverted microscopes. Also, the size of the devices plays a major role in cell sensing since not all sensors can be miniaturized, and their application down to a single cell level may not be possible. However, only the investigation of individual cells can be used for certain applications (WANG, BODOVITZ, 2010; ZARE, KIM, 2010).

Many impedimetric measurements utilize planar gold electrodes with several hundred square micrometers in size (HONG et al., 2011; PANCRAZIO et al., 1999). The downsizing of gold electrodes, however, is limited by the increase in impedance caused by the reduction of the gold area (PRICE et al., 2009). It is imperative to choose a suitable biosensor for the desired purpose and in accordance with the measurements that have to be performed. A single biosensor for cell-based measurements cannot combine all the properties that are needed for all kinds of measurements, and subtle device changes can have a huge impact on the performance. The immobilized cells react to a variety of stimuli, which can be electric, chemical, thermal, or drug-induced. These stimuli physiologically change the cells, leading to changes in action potentials, ion distribution, membrane density, and others. The main goal for the biosensors is to take these changes of the cell and translate them into electronically readable signals. This leads to the main challenges that cell-based biosensors have to face. Since the natural environment for the cells has to be mimicked, the devices have to be stable in these conditions for longer periods of time, and the device surface has to be compatible with the cells used. In addition, the sensors have to be selective and sensitive to the desired biological signals.

1.2 Organic Electrochemical Transistors

In this work organic electrochemical transistors (OECTs) made of the polymer poly(3,4-ethylenedioxythiophene) polystyrene sulfonate (PEDOT:PSS) were investigated. PEDOT:PSS is a water-soluble polymer which is a mixture of two ionomers, namely poly(3,4-ethylenedioxythiophene) (PEDOT) mixed with sodium polystyrene sulfonate (PSS). While PEDOT carries positive charges, PSS is charged negatively due to its deprotonated sulfonyl groups (Figure 1). PEDOT:PSS has been shown to have excellent biocompatibility and semiconducting properties (BERGGREN, RICHTER-DAHLFORS, 2007) and makes an ideal candidate for biosensing applications. Other favorable properties are its transparency, high conductivity (up to 4600 S/cm) and also its ductility, which enables the use of PEDOT:PSS for flexible sensors. A variety of PEDOT:PSS based organic electrochemical transistors have been investigated in order to record different cellular recordings.

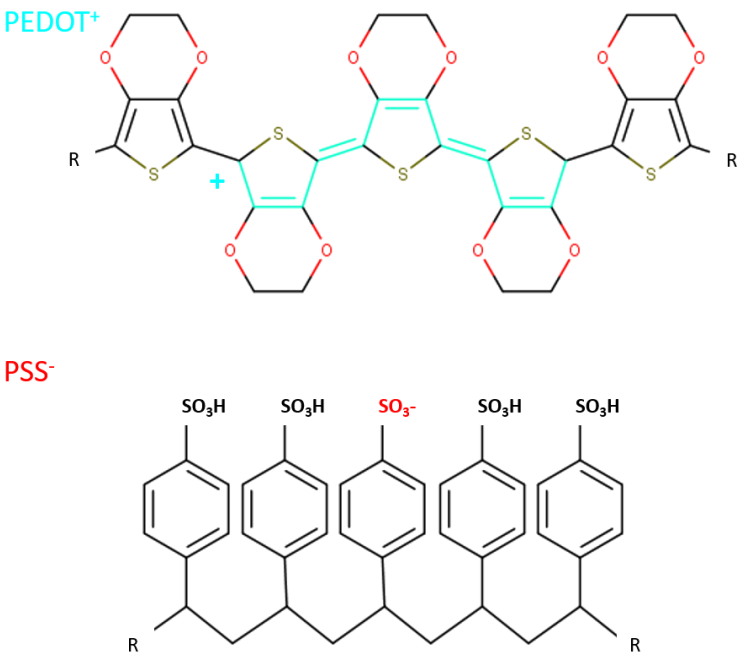

Figure 1: Schematic drawing of the chemical structure of PEDOT:PSS. PEDOT carries positive charges and every third or fourth thiophene carries a positive charge. At the same time, PSS is negatively charged due to deprotonated sulfonyl groups (ELSCHNER et al., 2012).

In the field of biosensing, PEDOT:PSS is often utilized as a transducer layer between electrodes. These sensors are usually built by connecting a source and a drain contact (usually gold) with PEDOT:PSS while a gate electrode (typically silver/silver-chloride) is immersed into an electrolyte on top of the polymer. PEDOT:PSS is a conductive but water-soluble polymer and needs to be chemically modified to be used as a transducer layer. Unlike field-effect transistors, the gating mechanism is not based on the opening/closing of a channel in a semiconductor material with a differently implanted sensing area. The gating mechanism of PEDOT:PSS based OECTs is of electrochemical nature, where a gate-source voltage in a positive range causes cations from the electrolyte to move into the polymer layer. The cations bind to the pendant sulfonate anions on the PSS and therefore decrease the hole density in PEDOT. The result is a decrease in conductivity, measured as a decrease of the drain current (KHODAGHOLY et al., 2013). A schematic representation of the ion movement can be seen in Figure 2, where the positive potential at the reference electrode creates a flow of positively charged cations towards the PEDOT:PSS layer.

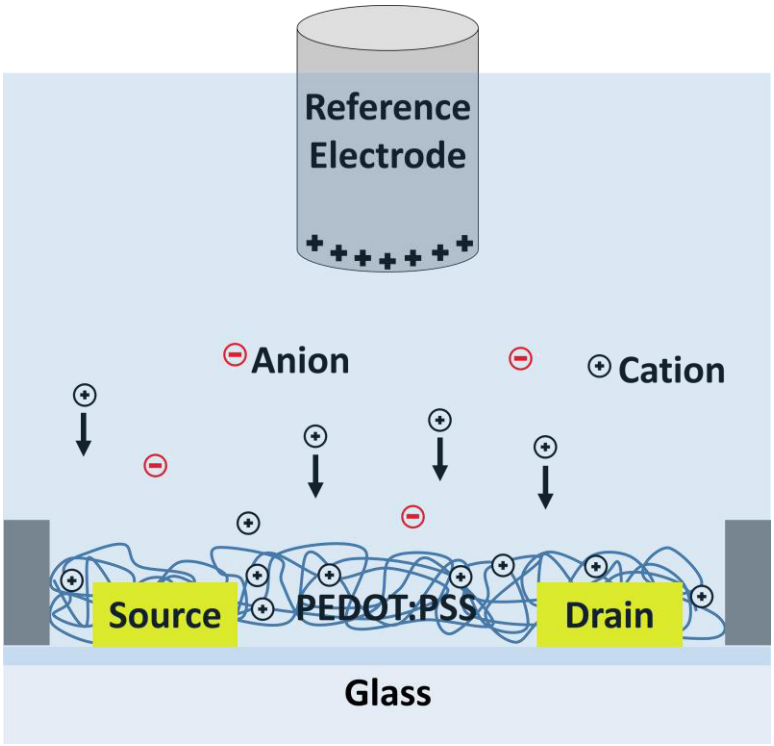

Figure 2: Schematic representation of the ion movement in an OECT based on the potential that is applied to the reference electrode. The positive potential causes a movement of the positively charged cations towards the polymer layer.

The influx of cations is enhanced by the swelling of the polymer while in contact with water. However, this swelling also causes the delamination of the polymer layer (JÖNSSON et al., 2003), which can be measured as an electrical deterioration. Therefore PEDOT:PSS is often modified with a second dopant to achieve higher stability in a liquid environment. Secondary dopants are usually applied to the aqueous phase of the PEDOT:PSS or applied as a post-treatment after the PEDOT:PSS solution is dried. It has been shown that different dopants can have different effects on the polymer film, not only depending on the dopant itself but also in which phase the dopant is applied. In general, all dopants address one of two characteristics of PEDOT:PSS. First, the dopants are added in order to increase the stability of the polymer layer towards liquids, and second, the dopants are supposed to increase the conductivity of the polymer beyond its base level. Dopants can have different effects on the stability of the polymer layer, one of which is an improved crosslinking (OUYANG, 2013). This improved crosslinking is thought to be a reason for the simultaneous increase in conductivity of the polymer. An additional suggested effect of the dopants is the removal of PSS from the surface region of the polymer layer, which increases the conductivity, as shown with X-ray photoelectron spectroscopy as an effect of the addition to aqueous PEDOT:PSS solution (CRISPIN et al., 2003). Another effect is the change of conformation of the PEDOT as shown with Raman

spectroscopy (OUYANG et al., 2004) which suggested a change of the benzoid PEDOT chain to a quinoid structure after the treatment with ethylene glycol (EG). This would suggest the change of PEDOT coils towards more linear and expanded structures. Several secondary dopants have been tested in combination with PEDOT:PSS. Polar organic solvents such as dimethyl sulfoxide, dimethylformamide, and tetrahydrofuran have been investigated as additives to an aqueous PEDOT:PSS solution (KIM et al., 2002). The maximum increase of the conductivity was achieved with dimethyl sulfoxide, with an increase of two orders of magnitude. In addition, other organic solvents or solids were tested, and it was found that organic solvents with a high boiling point like EG, nitromethanol or glycerol could significantly increase the conductivity of PEDOT:PSS. Organic solids, such as D-sorbitol were also found to have a similar effect. Ionic liquids can also be used to increase the conductivity of PEDOT:PSS in solution (DÖBBELIN et al., 2007). For ionic liquids, the concentration had a crucial effect on the conductivity as tested with 1-butyl-3-methylimidazolium tetrafluoroborate and 1-butyl-3-methylimidazolium bromide. Surfactants can be used as additives, both ionic and anionic surfactants were tested and were able to increase the conductivity by a factor 20 (DE IZARRA et al., 2018; FAN et al., 2008; LIM et al., 2012; LIPOMI et al., 2012; OUYANG et al., 2002; VOSGUERITCHIAN et al., 2012). These additives as secondary dopants are usually added to the PEDOT:PSS solution in order to achieve higher conductivities in the dry state. Another tested method is the conductivity enhancement by a chemical post-treatment, where the chemical dopants are added after the polymer layer is dried. Major enhancements were found by a post-treatment with EG or dimethyl sulfoxide (OUYANG et al., 2004) but also salts, cosolvents and acids showed significant effects (XIA, OUYANG, 2009, 2010b, a, 2011; XIA et al., 2010). Several other components were tested as post-treatment modifications to PEDOT:PSS such as formaldehyde and acetone as well as alcohols, and many more (DÖBBELIN et al., 2007; LUO et al., 2013; NARDES et al., 2008; XIA, OUYANG, 2012). For biosensor applications, however, mainly EG, dimethyl sulfoxide and, as of lately, divinyl sulfone (FAN et al., 2008; MANTIONE et al., 2017; OUYANG, 2013) are preferred due to their ease of use and significant conductivity and stability enhancement. Other additives also greatly enhance the device stability, one of the most commonly used chemical additives is (3-Glycidyloxypropyl)trimethoxysilane (GOPS) (HÅKANSSON et al., 2017). GOPS is mainly affecting the crosslinking of the PEDOT:PSS while also showing a negative impact on the conductivity. It was found that above a certain concentration of added GOPS a saturation of the conductivity occurred. It was proposed that the GOPS reacts with the PSS matrix and does not affect the PEDOT or the PEDOT:PSS interactions.

Seeing that additives have a huge impact on device performance, every sensor can be tailored to fit certain needs. However, some other regulations exist while working with PEDOT:PSS OECTs. The device characteristics are generated by the volume and also the thickness of the polymer on the devices (RIVNAY et al., 2015). Thinner devices work on the limit of complete dedoping and can reach higher frequency operation since the dedoping requires a smaller penetration depth of ions. This, however, would also decrease the drain current, leading to a lower sensitivity. Keeping the volume of the polymer constant and just altering the thickness would lead to a constant sensitivity while altering the response times. Due to this, the OECTs can be altered in very interesting ways. It is possible to increase or decrease the frequency cutoff, which influences how fast the sensors can operate and which signals can be detected. In the same way the transconductance (g_m) can be altered, which is the working point with the highest sensitivity. This means that the optimal device configuration has to be found for the desired application. The fabrication method can therefore be a limiting factor for the device performance. Material printing can be used to add a layer of PEDOT:PSS on top of already fabricated devices. However, due to the nature of this method, the miniaturization of the polymer layer area is limited. An area is created by overlapping droplets in a way that inhomogeneous layers are formed. These layers do not show the same consistency as achieved by spin coating fabrication (TEICHLER et al., 2013). Spin coating is utilized to achieve homogeneous PEDOT:PSS patterns with the possibility of achieving micrometer-sized structures with very thin layers when combined with cleanroom fabrication (LIN, YAN, 2012; MABECK, MALLIARAS, 2006). However, the integration of spin coating processes to the fabrication of the devices is more challenging than the material printing processes. The spin coating of the polymer layer has to be included in the cleanroom fabrication, while the material printing can be performed after the manufacturing of the devices.

OECTs with PEDOT:PSS have been used in a number of applications such as ion sensors (BERNARDS et al., 2008b; XIONG et al., 2017) humidity sensors (KUŞ, OKUR, 2009; NILSSON et al., 2002), glucose sensors (BERNARDS et al., 2008a; SHIM et al., 2009; TANG et al., 2011), immunosensors (KIM et al., 2010; MACCHIA et al., 2017), DNA sensors (LIN et al., 2011; TAO et al., 2017) and cell-based sensors (BOLIN et al., 2009; HEMPEL et al., 2017a; LIN et al., 2010) amongst others. Currently, many different ways for the fabrication of OECTs for biosensing exist, as briefly discussed in this chapter. The differences in preparation, as well as occurring limitations in equipment, lead to a widespread distribution of device performances (DONAHUE et al., 2018; DORIS et al., 2018; GUALANDI et al., 2018; MACCHIA et al., 2017). The main problems involving the use of PEDOT:PSS based OECTs for cell

sensing applications lie within the device parameters. Where OECTs are able to achieve very high sensitivity, the miniaturization of the sensors with a stable sensitivity is difficult. At the same time, the development of a mathematical model is necessary in order to properly interpret the measured data. There have been no applications shown for PEDOT:PSS based OECTs that can be used for confluent cell layers down to single cells with a suitable mathematical model to represent the results and gather information about the cell-related parameters in the process. A universally usable OECT for all different kinds of cell morphologies and signals would be of immense value to the field.

1.3 Electrical Cell Analysis

Several different cell signals can be measured with modern devices, so much so, that even the secretion of single biological components can be sensed with a very low limit of detection (DENG et al., 2014; LI et al., 2016).

The main electrical analysis methods for cellular detection include cellular action potentials and cell impedance. Action potentials of electrogenic cells are of high interest for cardiology and neuroscience research (SPIRA, HAI, 2013). While impedimetric measurements are widely used for the study of cellular adhesion in the form of e.g., proliferation, metastasis, and migration (XU et al., 2016). Both methods provide a non-invasive measurement of the observed cells. These two methods are amongst the most common and intensively studied methods to gain electrical data from cell-based assays.

While the detection of action potentials relies on adherent, electrically active cells, impedance measurements can be performed with any kind of adherent cells since the adhesion of the cells is causing the electrical change that can be measured with the devices.

In the event of an action potential, the membrane voltage is changing over time, crossing a cell-specific threshold which leads to the opening of sodium channels in the cell membrane. A positive current is entering the cell, which can be measured as a depolarization until the amount of positive charges inside the cell repels additional ions. After 1-3 ms the sodium channels close and the potassium channels open. The flow of potassium ions out of the cell lowers the membrane potential. This repolarization restores the membrane potential where the ions are on the wrong side of the cellular membrane. A hyperpolarization can often be observed when too many potassium ions

leave the cell. Ion pumps inside the membrane, namely the sodium-potassium pumps, restore the ion distribution between intracellular and extracellular space after this event happens. One of the most valuable techniques to analyze intracellular action potentials of cells is the patch-clamp method, where a glass pipette is connected with a living cell (ZHAO et al., 2008). This method offers real intracellular recordings with a good signal-to-noise ratio and a temporal resolution. However, the intracellular detection methods lack the possibility to easily measure several cells at the same time, which limits the possibility to measure cellular networks or the communication between a larger population of cells. Moreover, these methods are invasive and lead to the death of the measured cell after the pipette is removed. Therefore, noninvasive methods utilizing micro- or nanometer-sized electrodes have become an attractive alternative (SPIRA, HAI, 2013). Noninvasive methods allow for the stimulation and recording of cellular signals by various kinds of electrodes with high signal-to-noise ratios with the possibility to observe a whole cellular network on a big surface over a long period of time. Even though several device and electrode configurations are possible the main devices used for action potential measurements are MEAs (BAKKUM et al., 2013; SPIRA, HAI, 2013; WAGENAAR et al., 2004) and FETs to a certain extent (BERGVELD, 1972). New developments in readout systems and fabrication models enable the devices to have several hundred or even thousands of measurement points (ITO et al., 2014; JÄCKEL et al., 2017; MÜLLER et al., 2015) or transistor gates in nanometer size, able to detect intracellular signals (DUAN et al., 2012; TIAN et al., 2010). MEAs come in different sizes and shapes, offering stimulation and recording with high spatial and temporal resolution (NORMANN et al., 2001). Typically, MEAs contain metal electrodes with stable physical and chemical properties to monitor the activity of the cells. The measurement principle is based on the change in field potential caused by the action potentials in adherent cells and tissues. Cellular electrical activity is always based on an ionic-current flow through the cell membrane and therefore through the surrounding extracellular fluid. This ionic-current flow is directly related to the extracellular voltage gradient. This voltage gradient changes with the movements of the ions in and out of the cell. The gold electrodes transduce these ion currents into electron currents (PINE, 1980). The shape and amplitude of the recorded action potentials vary from the transmembrane potential. Since several electrically active cells can be measured at the same time, similarly to the multilayers of cells in tissues, the output signal may contain a mixture of multiple electric fields. The measured intensity of the signals increases with decreasing distance between the cell and the electrode which emphasizes the importance of the cell-electrode coupling (FRANKE et al., 2012; JÄCKEL et al., 2017). At the same time, the electrical field of cells outside of the

electrode area might still be detected in a weakened way due to their distance to the electrode (OBIEN et al., 2015). Signals are usually fed to external preamplifier stages with the signals being sampled and displayed by readout software afterward. In contrast to MEAs with planar metal electrodes, FETs offer a different approach in cellular sensing. FETs usually consist of three electrodes, the source, drain, and gate electrode. Where planar gold electrodes are typically used for MEAs, FETs are typically based on silicon semiconductor technology. In general, two different categories can be found for cell-based FET sensors (FANIGLIULO et al., 1996), first, sensors to detect the cell metabolism (FANIGLIULO et al., 1996; THEDINGA et al., 2007) and second, sensors to detect extracellular potentials of cells (BERGVELD et al., 1976; OFFENHÄUSSER, KNOLL, 2001). When detecting the metabolism of cells, a reaction of the cells towards a stimulus is typically recorded as a change in pH (FINN et al., 2002) or ion concentration (WROBEL et al., 2005). When adherent cells create action potentials a surface potential change of the dielectric layer occurs, resulting in a change in the current modulation in the FET channel (LEE et al., 2009). However, not all cells show electrical activity which means that for these cells other measurement methods have to be used. Just like the detection of field potentials, the ECIS method is a noninvasive measurement tool to monitor cell adhesion, kinetics, and spreading on a surface (WEGENER et al., 2000). Changes in the AC impedance of gold electrodes are monitored due to the change in surface potential induced by cell adhesion. In short, a signal amplitude with a certain frequency is applied to the electrodes, while the impedance is calculated from the change in voltage between the electrodes. Based on a model, the specific impedance of the cell covered electrode can then be calculated. A more advanced impedimetric measurement method using the transistor-transfer function can also be utilized for cell impedance measurements. A stimulation voltage is scanned over a frequency range giving a bandpass spectrum for the measurement system. The recorded spectra are a combination of the bandwidth limiting components of the system including effects caused by the reference electrode, electrolyte, the device, the readout system, and the biological component. This method enables the extraction of the dielectric properties of the biological component by a model (SCHÄFER et al., 2009).

While some devices are able to detect action potentials as well as the impedance changes caused by cell adhesion usually the devices excel at only one of these measurement methods and are not used for both measurement types at the same time. In general, impedance measurements down to single cell level are usually not employed since large gold electrodes are often used for these kinds of measurements. The development of a device platform that can be used for action potential

measurements and impedance measurements might provide interesting opportunities for advanced cellular sensing for different fields.

1.4 Modeling Basics

The modeling of cell-transistor coupling is a very important tool to understand and evaluate the measurement system as a whole or in single parts. A good model enables the adjustment of any given parameter in a simulation which predicts the outcome in the real measurement. Usually, mathematical models can be adjusted and expanded based on the desired application while varying in complexity. The base of cell modeling usually traces back to the Hodgkin-Huxley model (HODGKIN, HUXLEY, 1952) of a cell in combination with the point contact model proposed in 1989 (REGEHR et al., 1989). Both are the basis to describe the generation of action potentials in cells in a mathematical way. As for the Hodgkin-Huxley model, described in Figure 3, the lipid bilayer is described by a membrane capacitance (C_M) in parallel to the specific ion conductances for sodium (G^{Na}), calcium (G^{Ca}), and potassium (G^K). The Nernst potentials for these ions are included for sodium (E^{Na}), calcium (E^{Ca}), and potassium (E^K) as well. In addition, the specific ion conductance for the leakage (G^L) and the corresponding Nernst potential of the leakage (E^L) are shown. The current source (I_p) represents ion pumps and exchangers in the membrane.

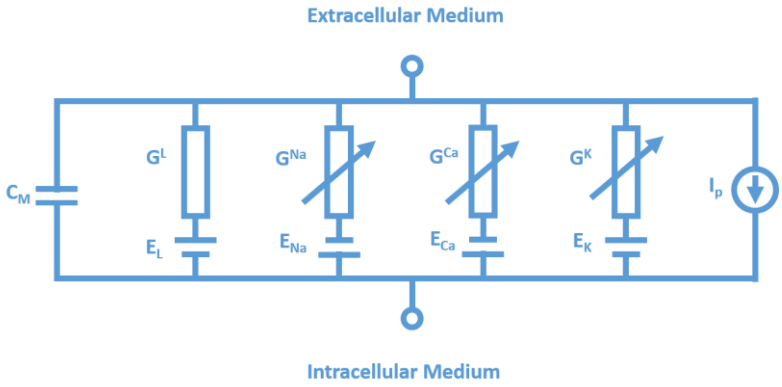

Figure 3: Schematic illustration of the Hodgkin-Huxley model of an electrically active cell with the lipid bilayer capacitance, the specific ion conductances and the corresponding Nernst potentials. Ion pumps and exchangers are considered as the current source (HODGKIN, HUXLEY, 1952).

This model can be used to understand the development of action potentials of electrically excitable cells as a function of time. Naturally, this model was improved over the years to make it more applicable for different situations, but as a base model,

it is still very useful. For the point contact model (Figure 4), a patch pipette is used in order to measure the intracellular voltage (V_M). The pipette capacitance (C_P) and the series resistance (R_S) are representing the pipette while the cell is divided into the free membrane (FM) and the junction membrane (JM). Hodgkin-Huxley elements (HODGKIN, HUXLEY, 1952) are used to describe the membrane function in both cases. The two membrane parts consist of the membrane capacitance (C_{FM} , C_{JM}) with their conductances of the leakage (G^L), the conductances of the ions (G^i) and the correlating Nernst potentials for the leakage (E_L) and the ions (E_i). The cleft between the cell and the transistor is represented by a junction conductance (G_J) and a seal resistance (R_{Seal}). The last parameters to complete this model are the junction potential (V_J), the bulk capacitance (C_b), and the applied voltage (V_S).

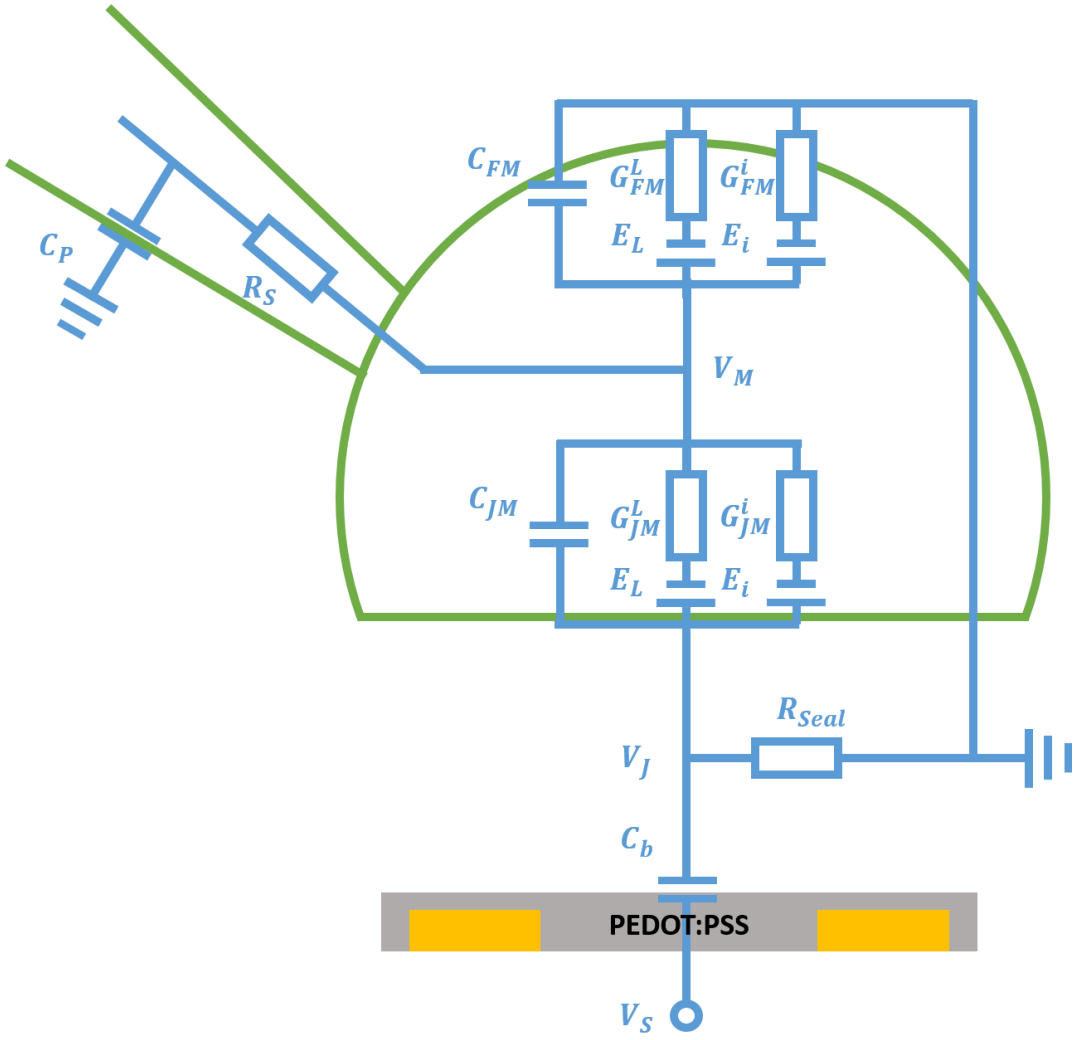

Figure 4: Schematic illustration of the point contact model for an adherent cell on an OECT (SUSLOPAROVA, 2016).

Both presented models can be applied to describe the cell-related parameters in a cell-based biosensor setup. In order to generate a model, the device-related parameters and the setup-related parameters have to be added.

The setup related parameters mainly focus on a transimpedance amplifier circuit. A schematic for such a circuit can be seen in Figure 5. The transimpedance amplifier consists of an operational amplifier and a feedback resistance ($R_{feedback}$) with a voltage source. It converts the drain-source current (I_{DS}) based on the applied drain-source voltage (V_{DS}) to an output voltage (V_{out}) for further amplification.

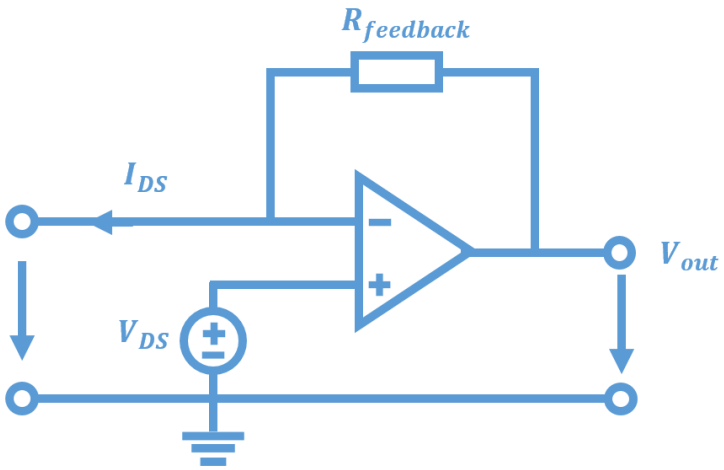

Figure 5: Schematic illustration of a transimpedance amplifier circuit, consisting of an operational amplifier, $R_{feedback}$ and the voltage source (SUSLOPAROVA, 2016).

The output voltage of such a circuit is calculated by the Equation (1.1):

$$V_{out} = V_{DS} + R_{feedback} I_{DS} \tag{1.1}$$

Based on Equation (1.1), $R_{feedback}$ is scaling the output voltage. This means an increase in amplification with increased $R_{feedback}$.

1.5 Aim of the Work

This work aimed to establish the fabrication, characterization, and application of PEDOT:PSS based OECTs for cell-based biosensing from confluent cell layers down to single cells. An OECT had to be developed with high sensitivity, stability, and transparency, which could be utilized for several biosensing applications, including the detection of cellular action potentials as well as the cell impedance. While cell measurements have been shown in the literature already the combination of these types of measurements on the same device with high accuracy and reproducibility has not been shown so far. The use of the transistor-transfer function (TTF) for these devices should be investigated as a new way of measuring these devices, and a model should be developed to mathematically represent the measured data in order to access different levels of the measurement procedure. By mathematically modeling the sensors a better understanding of the device properties and the measurements was expected which should give new insights on the OECT platform in general. The result was supposed to be a well understood and established sensor platform that can be fabricated easily and in a cost-effective manner, ideally showing the biggest possible versatility for a variety of cell-based applications. New methods should be used, not only for the fabrication but also for the application and the mathematical representation of the whole measurement setup. The shortcomings of already established device were to be overcome with an innovative approach.

2 Materials and Methods

In this chapter, the utilized materials and methods will be described. The shown methods are meant to enable the reproduction of the performed experiments.

2.1 Device Fabrication

The fabrication of the OECTs followed standard cleanroom processes; the detailed parameters are summarized in the supplementary chapter (Supplementary 1). Different sensing area sizes were fabricated to manufacture devices with 16 gates each in a common source configuration; the sizes were 200×200 µm^2, 100×100 µm^2, 50×50 µm^2, 20×20 µm^2. The finger width stayed constant over the different devices and was 5 µm in width and distance between the fingers. An exemplary structure of a wafer is given in Figure 6.

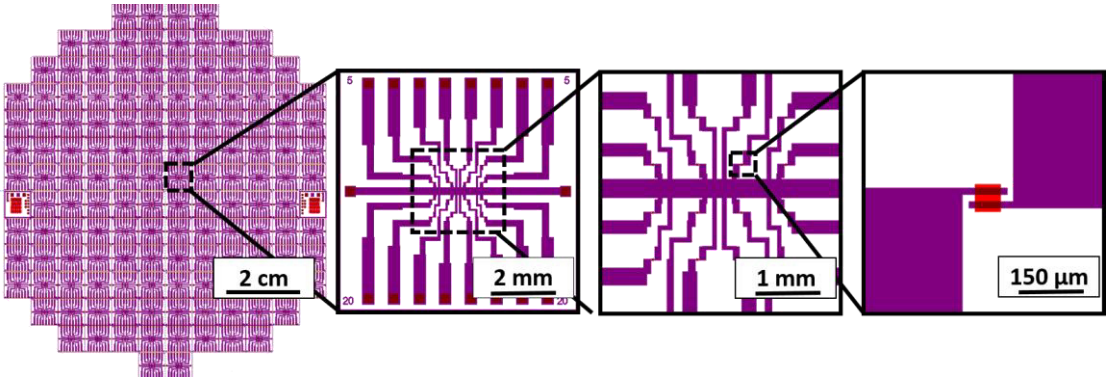

Figure 6: Mask used for the OECT structures with gate dimensions of 50×50 µm^2 and 20×20 µm^2 distributed over the whole 4-inch wafer. The contact lines which fabricated in gold are purple while the opening of the sensing area is red.

As a summary, the process can be described as follows. Interdigitated electrode (IDE) structures made of gold were chosen as the electrode material for the OECTs. The base is a 4-inch wafer made of silicon or glass. The wafers are cleaned in an ultrasound bath for 5 minutes in acetone, isopropanol, and deionized (DI) water respectively. Afterward, the wafers are cleaned in Caro's acid at 115 °C for 10 minutes, rinsed, dried, and kept in an oxygen plasma at 350 W for 5 minutes. AR-U-4030 image reversal resist (ALLRESIST GmbH, Germany) is spin coated onto the wafers at 2000 revolutions per minute (rpm) for 1 minute and dried at 85 °C for two minutes. After a cooling down time

of 10 minutes, the wafer can be exposed with a mask aligner (MA/BA6, SÜSS MicroTec SE, Germany) and the mask containing the contact lines. Hard contact mode is used to gain a maximum resolution. With the image reversal resist a post bake step is necessary at 115 °C for 5 minutes. After cooling down for 10 minutes, the whole wafer is exposed for 25 seconds before the resist is developed. In order to obtain the gold structures, the wafer is cleaned in oxygen plasma at 50 W for 30 seconds before the gold is thermally evaporated. A titanium, gold stack is evaporated with layers of 300 Å and 3000 Å, respectively. The wafers are then stripped from the excess gold in an ultrasound bath by 5 minutes of acetone immersion, followed by isopropanol and DI water. The wafer is then again cleaned in oxygen plasma at 350 W for 5 minutes before it is passivated in the physical enhanced chemical vapor deposition machine (Plasmalab System 13, Oxford Instruments, UK). Following the passivation step, another lithography step is performed just as mentioned before in order to open the 16 sensor areas and the contact pads for wire bonding. Reactive ion etching is used to open the contact pads (SI 591 M, SENTECH Instruments GmbH, Germany) for 10 minutes. From this point onwards the wafers can be cut and used with a material printer, however in order to generate the OECTs with spin coating fabrication other steps have to be taken. The glass wafer is then cut 300 µm in the back while the more brittle silicone is cut in front with a depth of 50 µm. By doing this, the wafer will not have to be cut after the application of PEDOT:PSS and the individual chips can be separated manually. Before the wafer is cut with a wafer saw (DAD-2H/6T, DISCO Corporation, Japan), a protective photoresist AZ 520d (Microchemicals GmbH, Germany) is applied and dried. After cutting, the wafer is stripped with the successive rinsing of acetone, isopropanol and DI water that was mentioned before. To perform the spin coating of PEDOT:PSS the wafer is coated again with AR-U 4030 photoresist with the same mask that is used to etch open the sensing areas and contact pads. Once the resist on the wafer is prepared, the wafer is activated at 250 W for 30 seconds in an oxygen plasma. PEDOT:PSS (739316, Sigma-Aldrich, USA) is spin coated at 3000 rpm for 30 seconds before the wafer is baked at 50 °C on a hotplate. The photoresist that is serving as a sacrificial layer, in this case, is removed by ultrasonication in acetone for 5 minutes at low power. EG (324558, Sigma-Aldrich, USA) was used as a secondary dopant in order to enhance the stability and conductivity of the PEDOT:PSS. EG is applied onto the wafer until the wafer is covered, while the wafer is heated to 80 °C for 30 minutes. Afterward, the wafer is rinsed with acetone and dried with nitrogen. At this point, the wafer can be separated manually into individual chips and stored in vacuum.

To apply the PEDOT:PSS with a Dimatix Materials Printer 2800 (Fujifilm, USA) the IDE chips are activated in oxygen plasma at 250 W for 30 seconds before the PEDOT:PSS is applied. The post-treatment with the secondary dopant EG remains the same as well as the storage in vacuum. The prepared OECTs have to be encapsulated in order to be used with the measurement setup as previously described (INGEBRANDT et al., 2003; OFFENHÄUSSER et al., 1997). The chips are glued on a printed circuit board carrier (LeitOn GmbH, Germany) with fast glue (UHU GmbH & Co. KG, Netherlands). The contacts are wire bonded with gold wire (Heraeus Holding GmbH, Germany) with a wedge-wedge wire bonder (West Bond Inc., USA). To protect the wires and in order to create a cell culture suitable device, a glass ring (Glassblowing Becker, Germany) was glued in the center of the chip and on the carrier surrounding the chip in the center. As a final step, the wire bonds and the carrier surface are covered with polydimethylsiloxane (PDMS) (SYLGARD 184, Dow Corning, Germany).

2.2 Measurement Setups

Several electronic setups were used and will be described briefly in this section. Mainly a Keithley Parameter Analyzer 4200A-SCS (Tektronix, USA), a house made TTF box, a lock-in amplifier HF2LI in combination with a HF2TA current amplifier (both Zurich Instruments AG, Switzerland), as well as a 16 channel FET amplifier with a house made preamplifier were used. In general, two measurement configurations were used. First, a two-point measurement between a source and a drain contact was used and second a three-point measurement configuration was used, where an additional silver/silver chloride electrode was immersed into a measurement buffer on top of the devices. The buffer was used as the electrolyte gate contact in this measurement configuration.

The Keithley parameter analyzer was used for the characterization of the chips during the cleanroom fabrication, right after the fabrication was finished, as well as after the encapsulation. Individual chips (separated or on the wafer) were contacted using needle probes while encapsulated chips were connected via an adapter to the Keithley system. Resistance measurements were performed during the fabrication as well as afterward in order to check for the successful opening of the contact pads/gate areas and for the deposition of PEDOT:PSS. For this purpose, a voltage from –1 V to 1 V was applied between the source and drain contacts while the resulting current was measured. After the chemical treatment with EG, the individual chips were

characterized to measure their transistor characteristics (TC). While the setup of source and drain contact remained the same an additional gate electrode was immersed in phosphate buffered saline (PBS) on top of the device. A voltage is applied between the drain and source contact. At the same time a regulatory voltage is applied between the gate and the source contact. The resulting current is then measured and used for the analysis. Typically, V_{DS} was set to -0.6 V with a gate-source voltage (V_{GS}) sweep from 0 V to 0.8 V. The sensitivity of the devices was calculated as the maximum point of the first derivative of I_{DS} over V_{GS}, also known as g_m. The point of highest g_m is equal to the working point with the highest sensitivity. For further measurements, the working point was set to V_{GS} = 0 V and V_{DS} = -0.6 V. The TTF box offers the measurement of the transistor-transfer function for 16 channels in parallel in a portable readout device capable of performing potentiometric and impedimetric readouts. Analog to the Keithley parameter analyzer, transistor characteristics can be evaluated, and the working point can be set. For impedimetric measurements, the TTF was used. The system is based on a phase-selective amplifier system; a direct digital synthesis device is followed by a multiplier and a parallel low pass filter. The OECTs are set to the working point, and a frequency sweep is performed from 1 Hz to 1 MHz. The bandwidth of the signal transfer from the pseudo-reference electrode to the first transimpedance amplifier is monitored by the phase selective amplifier resulting in the spectra. A feedback resistance of 10 kΩ is included in the measurement setup. To sweep the frequency and to stay in the pseudo-linear range, a sinusoidal modulation voltage of 10 mV amplitude is applied to the reference electrode. The spectra can show the voltage, g_m, and TTF values as the y-axis and the frequency as the x-axis. The signal was transferred via USB to a PC with a custom readout software called BioMol, which was implemented in Delphi 5.0 (Borland Software Corporation, USA). To increase the accuracy of the impedimetric measurements, a lock-in amplifier (HF2LI) with a current amplifier (HF2TA) was used in combination with the corresponding software LabOne (all Zurich Instruments, Switzerland). The HF2TA enables the conversion of the input current into a voltage output with a frequency range up to 50 MHz with a low noise and input leakage. The HF2LI is a digital lock-in amplifier that can operate in DC as well as AC with a frequency up to 50 MHz utilizing high-performance digital signal processing. The connection principle with the lock-in amplifier followed the TTF box example. As stated before, the working point was selected for device operation, while a sinusoidal signal with an amplitude of 10 mV was applied to the reference electrode with a varying frequency from 50 Hz to 1000 Hz. For this setup, only a single channel could be measured at a time.

The setup to measure the action potentials is the same that can be utilized for noise measurements and consisted of a pre- and a main amplifier (INGEBRANDT et al., 2001, 2005) connected to a PC with an input/output board (PCI-6071 E, National Instruments, USA) controlled by MED64 software (Alpha MED Scientific Inc., Japan). The devices were characterized using the customized software FETchar (SCHÄFER et al., 2009), and the working point was set. The same working point was kept for the action potential measurements in MED64.

2.3 Cell Culture Methods

The used cells were the cardiac muscle cells (HL-1), the human embryo kidney (HEK) 293 cells, and the Madin-Darby canine kidney (MDCK) cells. All the used cell lines were grown at 37 °C in 5% CO_2 atmosphere. The culturing was performed in a cell-specific medium, as suggested by the manufacturer. A detailed list of the culture media is attached in the supplementary section (Supplementary 2). The device surface was sterilized with ethanol for 5 minutes. Afterward, the ethanol was removed and the chips were air-dried in a sterile cell culture hood. A fibronectin coating (100 µg/ml) was used to benefit cell adhesion. Fibronectin solution (100 µl) was applied to the device surface, and the chips were incubated at 37 °C and 5% CO_2 for at least 4 hours. Before seeding the cells the fibronectin solution was removed under sterile conditions and the cells were applied to the devices in the desired amount. The basic protocols for passaging of the cells only varied slightly and are described in more detail in the individual paragraphs. The used cell types are summarized in Table 1 with their intended applications. The cells were observed regularly to ensure optimal growth.

Table 1: List of the used cell types, their origin, and the performed measurements

HL-1	Cardiac muscle cell line	Impedimetric detection of cell adhesion, action potential measurements
HEK 293	Human Embryo Kidney cell line	Impedimetric detection of cell adhesion from confluent cells down to single cells
MDCK	Madin-Darby Canine Kidney cell line	Impedimetric detection of cell adhesion of confluent cell cultures on sensor surfaces

HL-1 cells

For the experiments, the HL-1 cells (CLAYCOMB et al., 1998) were cultured on top of the OECTs. The devices were coated with 500 µl fibronectin/gelatin, where 1 ml fibronectin (A8350, AppliChem, Germany) was diluted in 199 ml of 0.02 % gelatin solution (G1890, Sigma-Aldrich, Germany)**,** which was left on the chips overnight before cells were plated. Each chip was plated with 50,000 cells in 50 µl medium. The medium was then filled to a total of 500 µl after 1 hour of adhesion time. Once a confluent state was reached (typically 2-4 days *in vitro*), spontaneous cell activity could be measured. In general, fresh, pre-heated medium was added to the cells 30 minutes prior to the measurements. The measurement time was below 5 minutes since the measurements were performed outside of the incubator. After the measurements, the medium could be replaced with the fresh, pre-heated medium again to perform another measurement on the next day. Norepinephrine (Merck, Germany) was used to increase the signal frequency during the measurements as a control for triggering a higher rate of action potentials. The concentration of norepinephrine ranged from 0.1 µM to 10 µM prepared in culture medium and subsequently added to the measured devices.

HEK 293 cells

In order to perform experiments with confluent HEK cell layers, 1,000,000 cells were prepared in 1 ml of medium. 20,000 cells were applied to the device surface in 20 µl medium. Measurements could be performed at the day of the cell seeding with a potential reduction in the adhesion strength of the cells. For the single cell experiments, the cell number per chip was reduced to 1000 cells, seeded in 50 µl per chip. The measurement was performed as soon as cells were covering the sensing areas. Due to the random distribution of the cells, no guaranteed adhesion of a single cell on a single sensing area was possible. In both cases, the cells were removed using 0.5 % trypsin ethylenediaminetetraacetic acid solution (PAN Biotech, Germany) to gain data for the cell detachment. The medium was removed, and 500 µl trypsin was added. The devices were kept in an incubator at 37 °C for 5 minutes before the trypsin was removed and fresh medium was added.

MDCK cells

For the MDCK cells, 50,000 cells were seeded onto the devices in 100 µl. Measurements were performed on the following day, provided that the cells were covering the sensing areas. In addition to the culturing medium, a medium was prepared containing ethylene glycol-bis(2-aminoethylether)-N,N,N′,N′-tetraacetic acid (EGTA, Sigma-Aldrich, Germany) to achieve a concentration of 0.5 M. The chips were incubated with the EGTA containing medium for 30 minutes before measurements were performed. Afterward, the medium was exchanged to the standard medium, and the chips were incubated for two hours to reverse the effect of the EGTA on the cells. As the last step, the cells were removed using trypsin as described before, and the standard medium was used for further measurements of the devices.

2.4 Organic Electrochemical Transistor Modeling

The modeling of the OECTs was performed using Origin software (OriginLab Corporation, USA).
An analytical equation was derived based on an electrical equivalent circuit which can be integrated into the nonlinear curve fitting tab in Origin. Several additional statistical methods can be employed to analyze the results gathered by the fitting procedure. At the same time, Origin was also used to simulate the curve behavior based on the implemented equation.

3 Results

In this chapter, the individual advances and performed experiments with the OECT devices will be described. Exemplary results for the individually performed measurements are shown and elaborated in the context of this thesis. In order to achieve a higher clarity, every subchapter will contain a conclusion with a short summary of the presented results and their impact. Different devices were used throughout the experiments and are mentioned separately if applicable for the experiments. To simplify the labeling of the devices, the OECTs in the following chapters will be named according to their sensing area sizes since the fabrication methods did not vary otherwise from the protocols stated in Chapter 2.1.

3.1 Device Fabrication

In this chapter, an overview of the achieved results in the fabrication of the chips is given. Many improvements led to a straightforward fabrication approach with high reproducibility and stability of the devices. While different methods of OECT fabrication can be used, two main approaches can be made, which are the fabrication of devices utilizing material printing or spin coating processes for polymer deposition. Both pathways can lead to functional OECTs with material printing being able to be applied to nearly all substrates after the device is finished, thus leading to an easy approach for testing. However, material printing does not provide the uniformity and reproducibility as can be expected from spin coating processes due to the difference in size of the droplets (Figure 7). In order to use spin coating processes, however, the PEDOT:PSS deposition has to be implemented in the fabrication process where contact with chemicals has to be avoided to achieve the highest purity of the polymer. In order to gain more insight into the fabrication of OECTs, the material printing technique was established first.

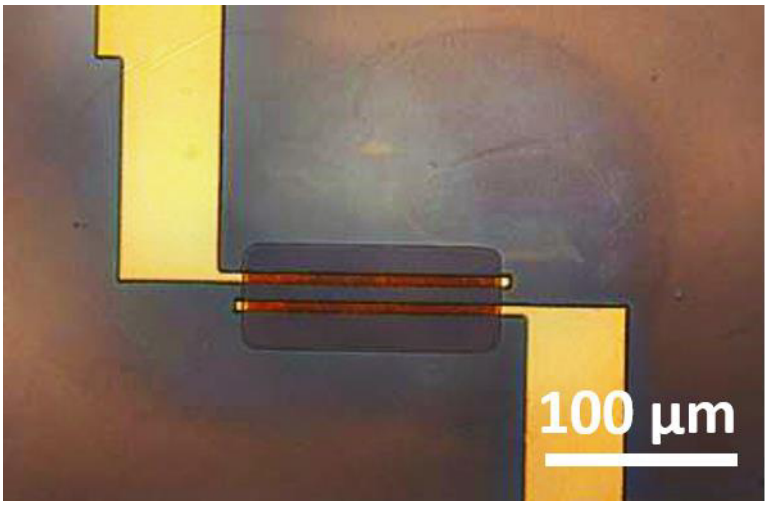

Figure 7: Microscopic image of a single IDE channel with PEDOT:PSS printed layer deposited with the material printer. The droplets can still be seen after drying, showing an inhomogeneous distribution of the polymer.

IDE devices were fabricated according to the protocol shown in Supplementary 1, with the difference that no polymer steps were included, so the wafers were cut after the opening of the sensing area/contact pads. PEDOT:PSS was then printed on individual chips, and the devices were encapsulated for measurements afterward.

To improve the devices using spin coating fabrication, standard cleanroom fabrication methods were supposed to be utilized for the fabrication of OECTs. This meant the use of simple tools without specialized equipment. For the OECTs, the fabrication was supposed to include gold electrodes for source and drain contacts a passivation layer created of stacks of silicon oxide, silicon nitride and silicon oxide (ONO) as to prevent leakage currents. A sacrificial layer had to be implemented in the process, while at the same time a contact of PEDOT:PSS with water or ultraviolet (UV) light had to be avoided. The required sacrificial layer had to be removed after the process without damaging the polymer layer to ensure the device function. Many different approaches were tested with a variation in materials and fabrication parameters. After several optimization steps the process shown in Figure 8 was successfully established. This process provides a new and simplified way to fabricate OECTs with standard cleanroom fabrication methods.

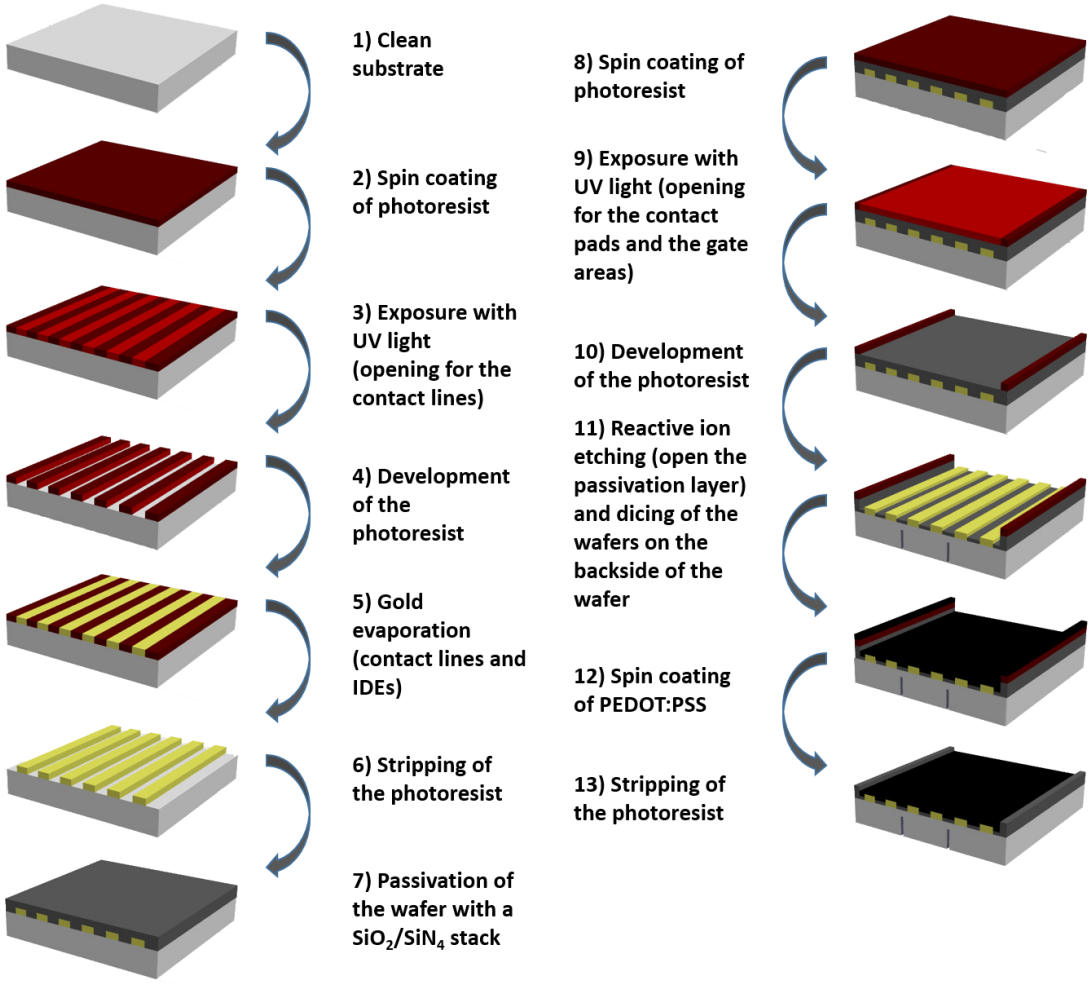

Figure 8: Schematic overview of the new OECT fabrication process, optimized in order not to harm the polymer (HEMPEL et al., 2017b).

IDEs were chosen as electrodes in order to keep the electrode area reproducible between different devices. In this way, a shift of the sacrificial layer would not cause a change in the area of the source/drain electrode. An example of a glass wafer with gold IDEs can be seen in Figure 9. For a parallel readout, a common source approach was implemented with 16 individual drain contacts. This common source was used to apply a voltage to all 16 channels at the same time. However, the configuration also allowed for the switching of the electrode configuration in order to apply the voltage to only one channel.

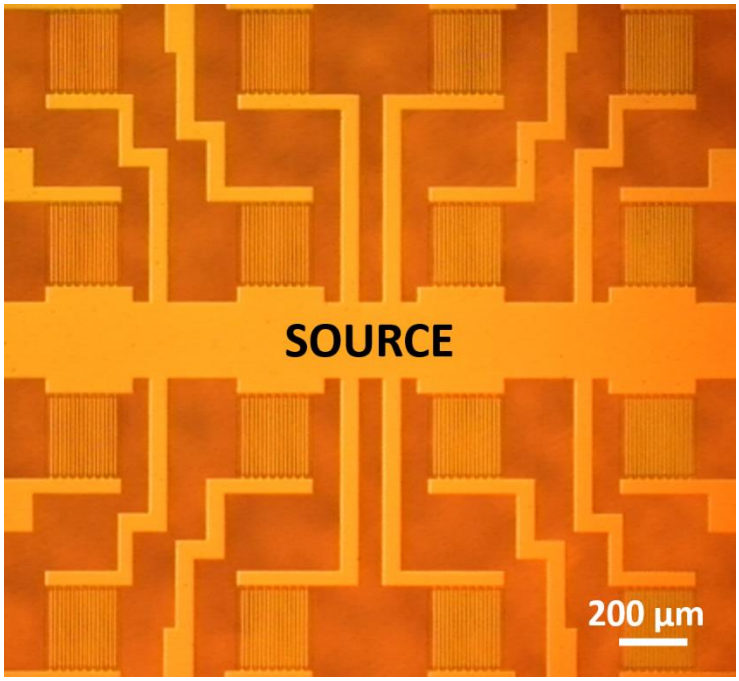

Figure 9: Microscopic image of gold IDEs on a glass wafer, the sensing areas are arranged in a 4x4 pattern.

To avoid contact of the PEDOT:PSS with water, a new dicing method was developed. The finished IDE wafers were cut on the backside for 300 µm at a wafer thickness of 550 µm so that the chips could be separated by hand after the fabrication. By only partially dicing, the wafers could still be used for all the necessary cleanroom fabrication steps avoiding the need for the application of a protective photoresist on top of the polymer layer. An additional advantage of this method is that no thermal stress is introduced to the polymer since no additional photoresist is added which would have to be baked at a certain temperature. Using this method, only one lift-off has to be performed, which again prevents contamination of the polymer layer or a possible damaging by chemicals. It was found that the relation between cutting depth and wafer thickness is crucial for the success of this step. Cutting too deep would make the wafer handling more difficult since the wafer would break easily while handling or using spin coaters or mask aligners. At the right depth, the wafers can be handled like normal wafers, and no limitations were found concerning equipment or methods. It should be noted that the same procedure can be utilized for silicon wafers, where the cutting was performed on the front side of the wafers due to the non-transparency of silicon, only using a depth of 150 µm for wafers with a thickness of 500 µm. Silicon, however, is more brittle than glass and has to be handled with more care during the rest of the fabrication. Photoresists were tested as sacrificial layers due to their easy implementation into the process. While theoretically many photoresists could be used

not all developers were suitable for PEDOT:PSS, especially when water was used in addition to the developer. Furthermore, a high aspect ratio with vertical walls was desired in order to achieve defined PEDOT:PSS patterns. The most reliable and reproducible photoresist to use as the sacrificial layer was the image reversal resist AR-U-4030, which can be easily removed by acetone. The photoresist was spin coated onto the passivated wafers after cutting, and the IDEs were opened. Afterward, the wafers were activated in oxygen plasma for 30 seconds to enhance the binding of PEDOT:PSS to the surface. PEDOT:PSS was spin coated onto the surface for 30 seconds at 3000 rpm and dried at 50 °C for 5 minutes. Higher temperatures at this point prevented the removal of the photoresist, but it was found that the polymer only had to dry to withstand the acetone bath. Optical controls were employed, and the polymer layer could be seen under the microscope (Figure 10). In this stage, the polymer can still be removed by water as long as no chemical post-treatment is applied. It is crucial to perform this treatment after the removal of the sacrificial layer. The application of EG to wafers with the sacrificial photoresist layer intact showed that the photoresist could not be removed anymore.

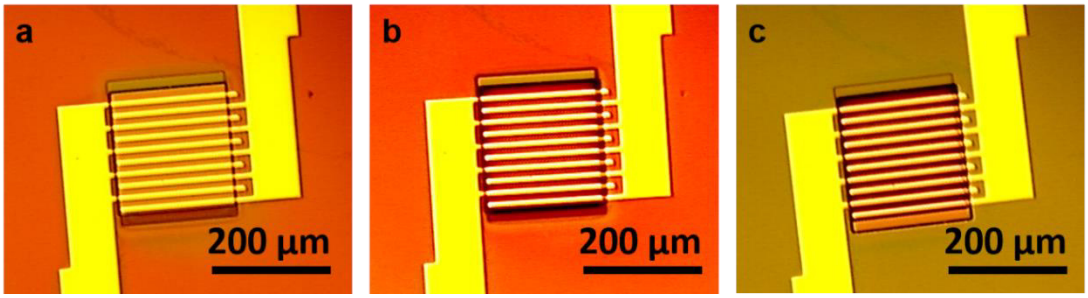

Figure 10: Microscopic images of the same channel during the cleanroom processing: a) channel with sacrificial layer of AR-U-4030 photoresist, a small offset to the passivation opening can be seen, b) channel after the spin coating of PEDOT:PSS for 30 seconds at 3000 rpm, with drying at 50 °C for 5 minutes, the polymer can be seen as a black layer, c) channel after removal of the sacrificial photoresist layer, the polymer can still be seen as a black layer.

A chemical post-treatment with EG was used to further enhance the electrical properties of the PEDOT:PSS and to create stability towards liquid immersions. It was found that the post-treatment is necessary to perform measurements with the devices since contact with water is enough to remove the thin polymer from the wafer surface. EG was chosen as the secondary dopant due to the increase in stability and performance and its ease of application. The fabricated wafers were immersed in EG for 30 minutes at 80 °C and could afterward be separated in individual chips and used for measurements. Longer exposure to EG did not show changes either in stability or

electrical properties. An increase in the temperature for the EG process also showed no effect on the device performance.

After the separation of the chips, they were either stored in a vacuum bag or encapsulated for use as sensors (Figure 11).

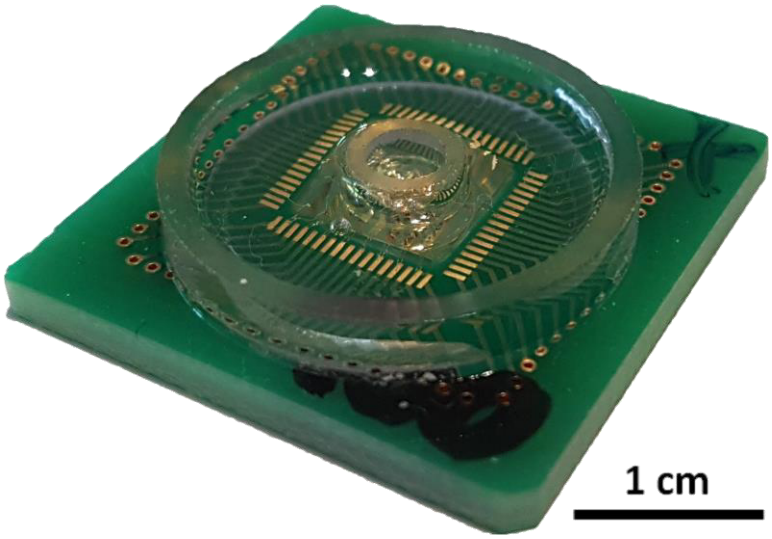

Figure 11: Encapsulated OECT, the glass chip is electronically connected to the PCB carrier by wire bonds. Glass rings create a reservoir for a measurement electrolyte while all the electronic contacts are covered with PDMS.

In this configuration, the devices allow for a parallel readout of 16 channels with 500 µl of liquid on top of the OECTs. The external reference electrode can be attached directly to the carrier or be entirely separated from the device. In order to perform measurements, a carrier holder was built where all existing channels could be connected individually if necessary.

3.2 Electrical and Optical Characterization of the Sensors

The fabricated OECTs had to be characterized towards their usability for biosensing purposes. These characteristic measurements are typically performed for all biosensors prior to their use for assays. Electrical characterization methods are paramount to determine the sensitivity, frequency dependency, and noise of the devices. Especially for cell measurements, these values provide valuable insight towards the device applicability since a high sensitivity with a high signal-to-noise ratio is crucial for clear cell measurements. Additional parameters, such as the device roughness, help to understand the possible cell binding behavior to the sensor surface. The characterizations were performed to gain insight into the basics of the PEDOT:PSS biosensors and for their use in cell-based assays.

3.2.1 Transfer Characteristics and Transconductance

The first step in determining the device function was the measurement of the TC and the g_m. Measurements followed the protocol described in Chapter 2.2. A schematic overview of the measurement configuration can be seen in Figure 12 with a three electrode connection.

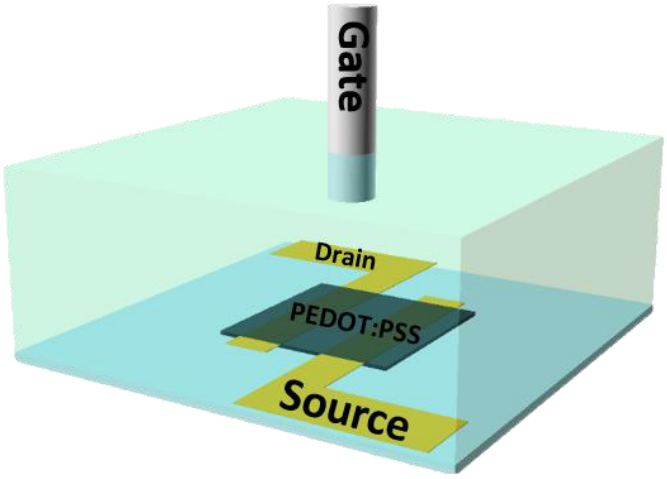

Figure 12: Schematic image of the measurement configuration in an electrolyte solution with the typical source, drain, and gate electrode contacts.

It was found that the simultaneous application of a voltage via the common source contact can deteriorate the device performance faster. This effect did not occur when the channels were measured individually. Since the common source setup only provides benefits for parallel measurements, the switching of the connection was not problematic. The first tested devices were OECTs that utilized material printing as a means of polymer deposition. While these devices could show sufficient g_m values of up to 15 mS depending on the sensing area size, these devices were lacking the uniformity needed for meaningful research. This lack in uniformity originated from the material printing procedure, which caused major differences in the TC on the same device (Figure 13). When measured with the TTF box for 16 channel parallel readout, some measured channels showed major variations from the others.

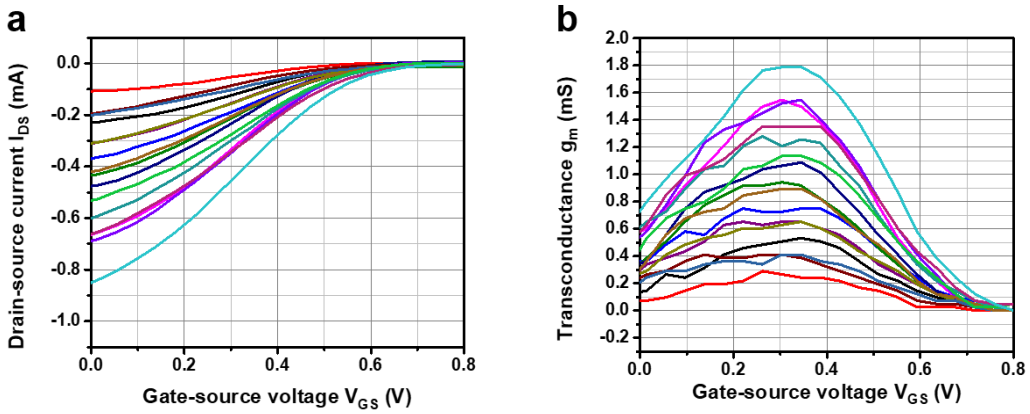

Figure 13: Transfer characteristics of 16 channels of an OECT where the PEDOT:PSS was deposited by a material printer, a) measured I_{DS} over V_{GS}, b) corresponding g_m values as the first derivative of the data shown in graph a.

Individual channels showed similar characteristics, but overall, there seemed to be a random variation of measured currents and g_m values, matching with the randomness of the gate coverage with the polymer. Further analysis was performed to gather information about g_m variation between more devices. The results showed a random distribution for the maximum g_m for 73 channels measured for several OECTs. A range from 0.14 mS to 2.8 mS was measured with an average of 1.05 mS with a standard error of 0.08 mS for 100×100 µm^2 devices at V_{DS} = -0.2 V (Figure 14).

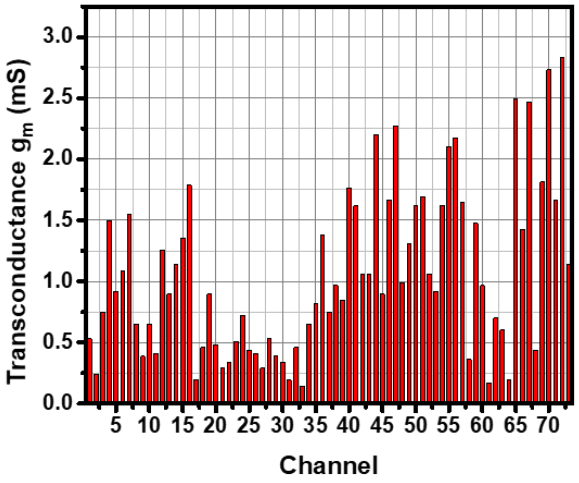

Figure 14: Data of 5 different OECTs with 73 working channels and their g_m values. The devices were from different batches with 100×100 µm² OECTs. PEDOT:PSS was deposited with a material printer.

It can be seen that the variation of the g_m value is big. Some channels show a g_m below 0.2 mS while others have a g_m of more than 2.75 mS. This can be directly attributed to the fabrication method with the uncontrollable overlap of PEDOT:PSS layers. While the devices could still be used for measurements with individual channels, a comparison between the channels could not be performed due to the vast distribution of the g_m values. The differences in the sensitivity, as measured by the g_m, make these devices not suitable for measurements over the whole device. This is what ultimately lead to the need of spin coated OECTs with a lower variation between channels. Figure 15 shows 69 channels of 5 different OECTs that were prepared by spin coating. Unlike in Figure 14, the devices consisted of 200×200 µm² sensing areas.

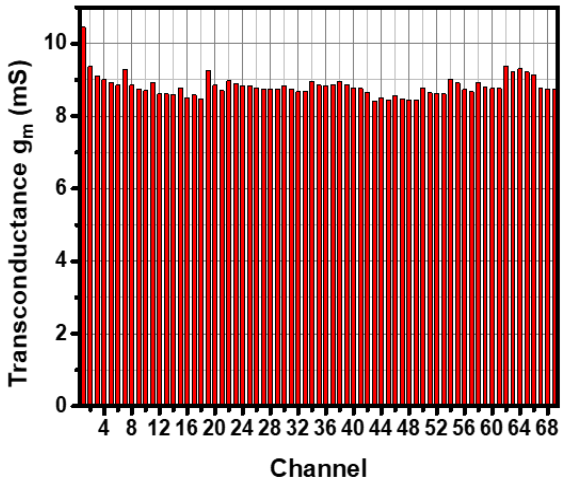

Figure 15: Data of 5 different OECTs with 69 working channels and their g_m values. The devices were from different batches with 200×200 µm² OECTs. PEDOT:PSS was deposited with a spin coater.

It can be seen that the variation in g_m is severely reduced for the device utilizing spin coating to apply the polymer layer. The increase in sensing area size increased the overall measured g_m. Despite the bigger sensing area, with a higher risk of polymer delamination, a high reproducibility for different devices of different batches was achieved. Additional advantages of the spin coated OECTs will be discussed in the following chapters in more detail.

Several dimensions for the sensing areas differing in the number of fingers and area of deposited polymer were established. The fabricated devices had sensing areas of 200×200 µm^2, 100×100 µm^2, 50×50 µm^2, 20×20 µm^2 while the fabrication itself stayed the same, which should result in the same thickness of PEDOT:PSS within the devices. A characterization was performed with devices of the different sensing area sizes. Figure 16 shows the TC of the devices and their corresponding g_m values.

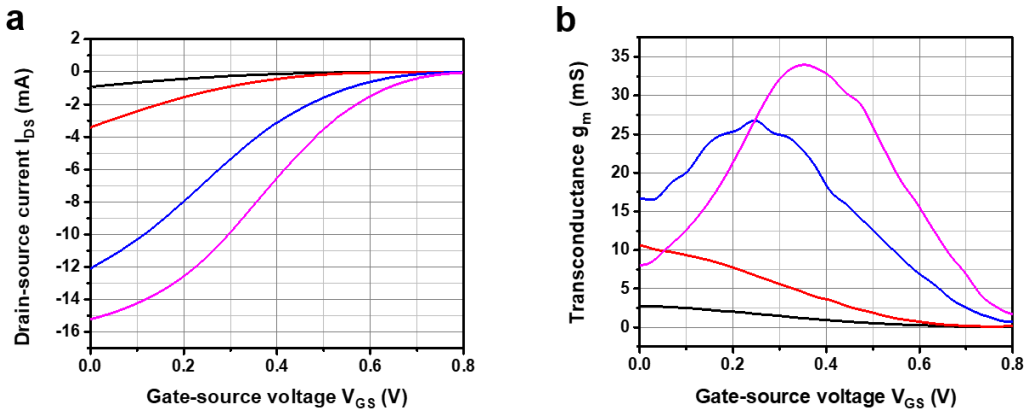

Figure 16: Comparison between the devices with different gate sizes (pink: 200×200 µm^2 blue: 100×100 µm^2, red: 50×50 µm^2, black: 20×20 µm^2) at a V_{DS} of -0.6 V, a) TC curves with b) first derivate to show the g_m values.

As can be seen from the graphs, the measured I_{DS} is decreasing with the decrease of the sensing area. At the same time, the steepness of the curves increases with the increase of the sensing area, which results in higher g_m values being measured. A short overview of the average g_m for three devices with the corresponding voltages for the working point is given in (Table 2). The increase of the sensing area from 400 µm^2 for the smallest devices to 40,000 µm^2 results in an increase in g_m by a factor of 10.

Table 2: Values of I_{DS}, g_m, and working point for Figure 16 as average values for three OECTs with 16 channels each

Chip	I_{DS} max	g_m max	Working point
200×200 µm²	-15.22 mA	35 mS ± 0.23 mS	V_{DS} = -0.6 V; V_{GS} = 0.35 V ± 0.01 V
100×100 µm²	-12.10 mA	25 mS ± 0.42 mS	V_{DS} = -0.6 V; V_{GS} = 0.25 V ± 0.08 V
50×50 µm²	-3.43 mA	10 mS ± 0.22 mS	V_{DS} = -0.6 V; V_{GS} = 0 V ± 0.03 V
20×20 µm²	-2.87 mA	3 mS ± 0.28 mS	V_{DS} = -0.6 V; V_{GS} = 0 V ± 0.08 V

In order to ensure that the measurement of the devices is not leakage driven, the leakage currents (I_{GS}) between gate and source were always measured in parallel. For the devices shown in Figure 16, the leakage currents are summarized in Figure 17.

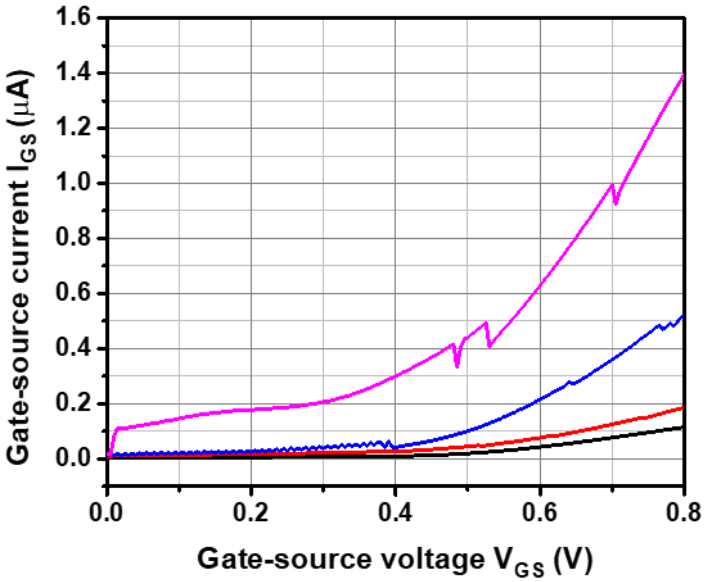

Figure 17: Corresponding leakage current of the devices shown in Figure 16 (pink: 200×200 µm², blue: 100×100 µm², red: 50×50 µm², black: 20×20 µm²).

The leakage current shows a maximum value below 1.4×10^{-6} A for the devices with the biggest sensing area, which is a factor 10,000 lower than the measured I_{DS}.

In an additional approach, V_{DS} was altered and found as a major influence on the chip characteristics (Figure 18). It can be seen that a higher V_{DS} results in a higher I_{DS}. This was found to be consistent, independent from the sensing area size. Two effects occur due to the increase in V_{DS}, first the steepness of the curve increases, which is resulting in higher g_m values, second the position of the working point is shifting towards lower V_{GS}. This allowed for the 20×20 µm² and 50×50 µm² OECTs to be operated at

V_{GS} = 0 V for V_{DS} = -0.6 V. As can be seen from the graphs a further increase of V_{DS} would not lead to a higher g_m since the curve would show a shift to lower V_{GS} which in turn would only reduce the maximum g_m. Setting the working point at V_{GS} = 0 V added the benefit that the working point did not change during performed measurements. Even after deterioration effects occurred, the maximum g_m was always present at V_{GS} = 0 V (with the matching V_{DS}). Therefore, the devices can be set into the working point, even when the exact location of the working point is unknown.

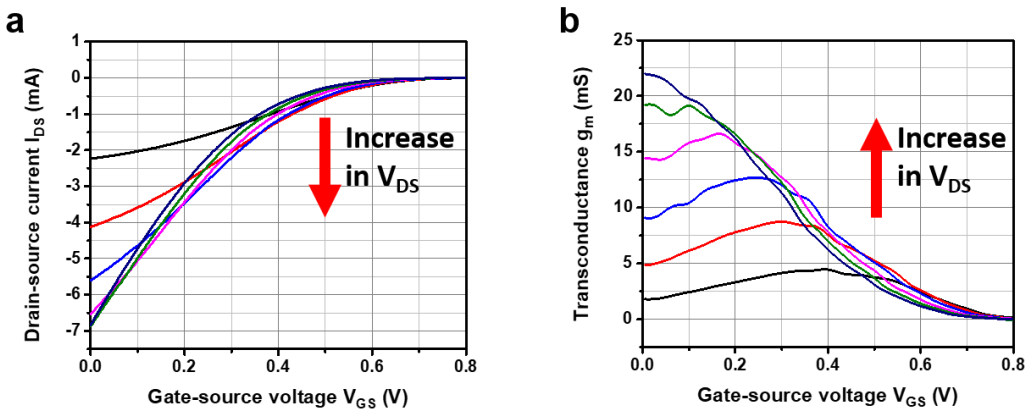

Figure 18: Investigation of the V_{DS} on the performance of an OECT (here 100×100 µm²). a) V_{DS} from – 0.1 V to – 0.6 V in 0.1 V steps, in 10 mS/cm NaCl at pH 7, b) corresponding g_m values. An increase in V_{DS} is causing an increase in the measured I_{DS} and g_m.

In any case, it was found that the measurement range of the devices cannot be changed to negative V_{GS}. Even though the graphs in this section show a shift to lower V_{GS} by lowering the channel size or by increasing V_{DS} it was found that the devices deteriorate and should not be operated in negative gate voltage regimes. More detailed results for this phenomenon are placed in Chapter 3.3.

In summary, the findings about the devices in this subchapter can be described as follows:

- The polymer volume is crucial for device performance.
- V_{DS} scales the measured current, meaning that an increase in V_{DS} is causing an increase in I_{DS} and g_m.
- V_{DS} shifts the working point at constant polymer volume.
- The volume of the polymer scales the measured I_{DS} and g_m.
- The leakage current is very small compared to the output current.

3.2.2 Frequency Response

By usage of the TC, the g_m is determined, which is the crucial factor for cell-impedance measurements. In order to apply TTF measurements, the frequency response, also called bandwidth, of the OECTs had to be tested. Not only does the bandwidth give an estimate of the capability of the sensors for cellular action potential measurements where a certain speed is mandatory, but it can be used as individual sensing method as well. Two measurement systems were tested for this purpose. Both setups vary in their hardware and are used to achieve an estimate of the device function. The first setup was the TTF box mentioned above with 16 channel parallel readout capability, and the second setup used a device connector with the lock-in amplifier. For comparability, the devices with different sensing area sizes should be set in their working point utilizing the same V_{DS} throughout. The measured spectra over the frequency range can be used to determine at which frequencies the devices can be operated. For some measurements the cutoff frequency at the half-power point can be considered as a point to compare the different devices. For that the output voltage is taken at a factor around 0.707 of its maximum value.

For the devices where the PEDOT:PSS was deposited with the material printer, the frequency spectra were determined with the TTF box directly after the characterization. A frequency sweep was performed from 1 Hz to 100 kHz. Figure 19 shows the measured spectra for an exemplary device. For the TTF the y-axis is given as a normalized value, if plotted as voltage or g_m the variations would be more drastic so that in this case the frequency response appears to be more uniform.

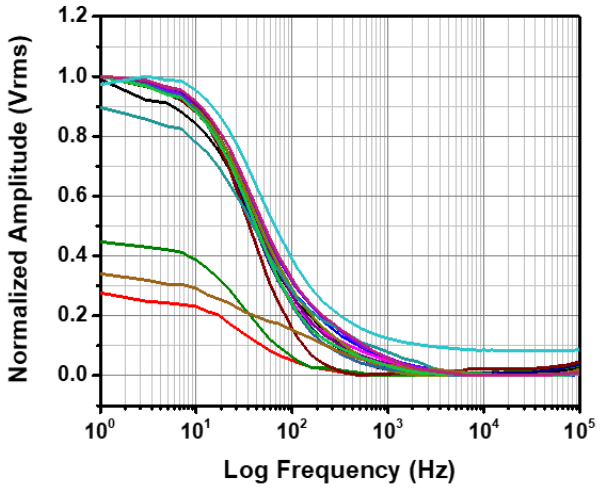

Figure 19: Frequency spectra measured by the TTF box for a material printed OECT (100×100 µm²). Every curve represents one of the 16 channels of the device.

The detected cutoff frequency is below 100 Hz for the printed 100×100 µm^2 devices, which is too low for cellular action potential measurements. In order to detect cellular action potentials, a cutoff frequency of 1000 Hz is usually a prerequisite. Based on the absolute refractory period of 1 ms for cells and a maximum frequency response of 1000 s^{-1}, a frequency of 1000 Hz can be calculated. Typically, the action potential frequency is lower for most cells. However, the devices could still be utilized for impedimetric measurements.

As for the spin coated devices, a higher uniformity concerning the frequency bandwidth on the individual chips was found (Figure 20). It can be seen that the device shows a certain degree of uniformity over 16 measured channels.

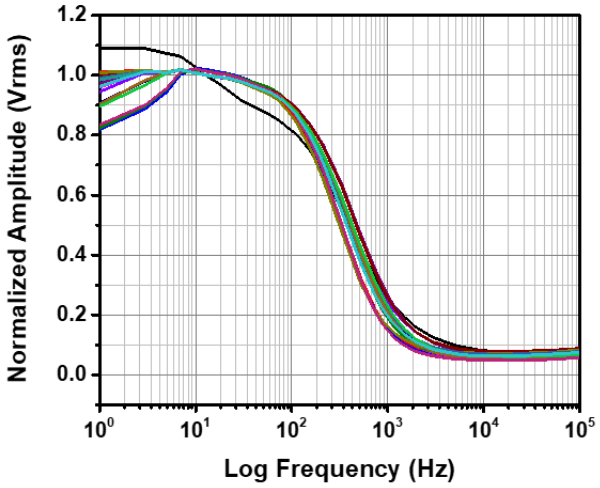

Figure 20: Frequency bandwidth measured by the TTF box for a spin coated 100×100 µm^2 OECT. Every curve represents one of the 16 channels of the device.

The variation that might lead to a shift in the measured cutoff frequency can be attributed to the hardware of the measurement system. It was found that the parallel readout of 16 channels can cause a shift in some channels that is not observed when the channels are measured individually.

The difference in the frequency spectra between the devices with different sensing areas was investigated. For that purpose, the cutoff frequency of the devices was measured in NaCl with a conductivity of 0.5 mS/cm over a frequency range from 1 Hz to 100 kHz while operated at a V_{DS} of -0.6 V. All devices were measured in their respective working points (Figure 21).

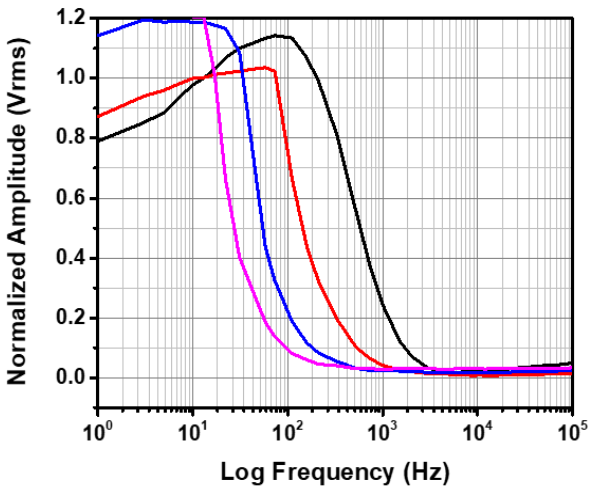

Figure 21: Measurements of the frequency response performed with the TTF box on devices with different sensing areas (pink: 200×200 µm² blue: 100×100 µm², red: 50×50 µm², black: 20×20 µm²). The measurement electrolyte was NaCl with a conductivity of 0.5 mS/cm at a V_{DS} of -0.6 V.

It can be seen that due to a hardware limitation, parts of the graphs are cut, mostly affecting the measurements for the devices with larger sensing areas. For these measurements, a straight line appears in the lower measured frequencies. This effect is based on a hardware limitation of the used National Instruments card, where the card is not able to measure an output voltage higher than 10 V. Every time the output voltage exceeds this limit the measurement is not continued until a lower voltage is reached. Due to the high conductivity of the OECTs, this limit is exceeded for certain types of measurements. Since the cutoff frequency is taken at around 70.7 % of the maximum amplitude, this effect does not alter the measurements and gathered results. Figure 21 suggests the highest cutoff frequency at 385 Hz for the devices with the smallest sensing area at 20×20 µm². The cutoff frequency for the other devices is decreasing with the increase in sensing area. The 50×50 µm² device showed a cutoff frequency of 103 Hz, the 100×100 µm² device was measured at 44 Hz and the 200×200 µm² chip had the cutoff frequency shifted to 21 Hz. This suggests a faster operation when the sensing area is reduced. In order to not exceed the hardware limitations concerning the output voltage, the sensitivity of the OECTs can be reduced by lowering the applied V_{DS}. In Figure 22, V_{DS} was reduced to -0.3 V, which in turn lowered the sensitivity of all the devices when their g_m values were measured. The frequency response, however, stayed constant with respect to their distribution based on the size of the sensing area.

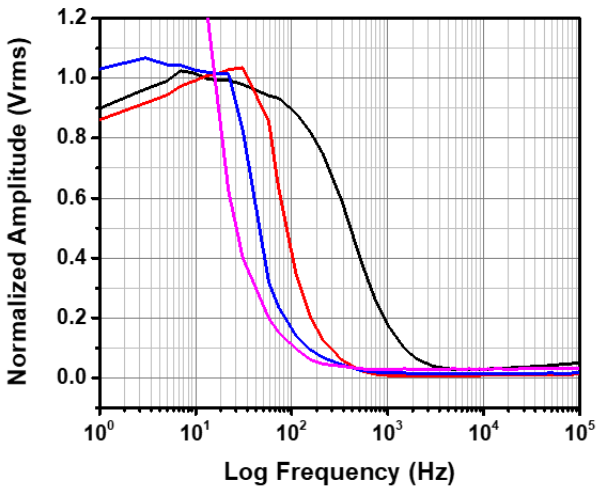

Figure 22: Measurements of the frequency response performed with the TTF box on devices with different sensing areas (pink: 200×200 µm² blue: 100×100 µm², red: 50×50 µm², black: 20×20 µm²). The measurement electrolyte was NaCl with a conductivity of 0.5 mS/cm at a V_{DS} of -0.3 V.

It can be seen that the devices with the smallest sensing area show the highest frequency cutoff. Overall a decrease of the cutoff frequency was measured with the lower V_{DS}. From smallest sensing area to the biggest the frequencies shifted to 230 Hz, 67 Hz, 36 Hz, and 21 Hz. This means a reduction of 40 % for the 20×20 µm² device. When altering the V_{DS} from -0.1 V to -0.6 V in 0.1 V steps the behavior of the cutoff frequency depending on V_{DS} can be seen (Figure 23).

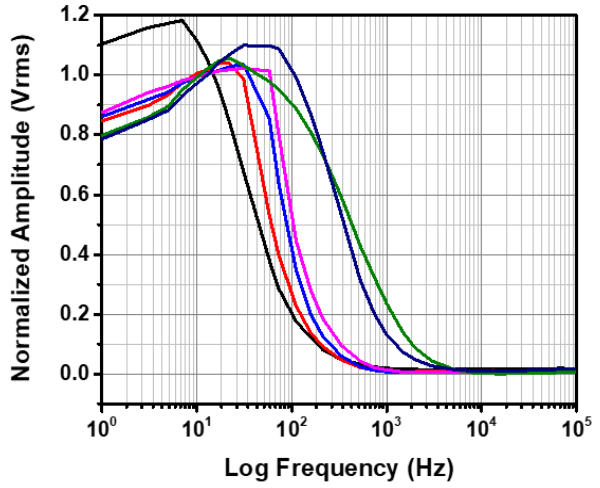

Figure 23: Measurements of the frequency response performed with the TTF box on a 50×50 µm² device with different applied V_{DS} from – 0.1 V to – 0.6 V in 0.1 V steps (black: V_{DS} = -0.1 V, red: V_{DS} = -0.2 V, blue: V_{DS} = -0.3 V, pink: V_{DS} = -0.4 V, green: V_{DS} = -0.5 V, purple: V_{DS} = -0.6 V). The measurement electrolyte was NaCl with a conductivity of 0.5 mS/cm and the devices were always set in their respective working points.

When altering the V_{DS} on the same device, an additional shift of the cutoff frequency can be observed. Figure 23 shows this behavior based on an example device with 50×50 µm^2 OECTs. By increasing the V_{DS} and therefore increasing the sensitivity as measured by the obtained g_m values, the frequency cutoff is increased as well. In these measurements the cutoff frequency shifted from 29 Hz at V_{DS} = -0.1 V to 44 Hz at V_{DS} = -0.2 V, 66 Hz at V_{DS} = -0.3 V, 83 Hz at V_{DS} = -0.4 V and 230 Hz at V_{DS} = -0.5 V and also 230 Hz at V_{DS} = -0.6 V. At the higher V_{DS} the cutoff frequency was the same which could be due to the fact that the g_m for these devices was the same at the applied V_{DS}.

When measured with the lock-in amplifier the chips were characterized beforehand with a parameter analyzer in order to measure the voltages to set the working point, since the lock-in amplifier does not have the capability to directly show the working point out of the current-voltage characteristics. The OECTs are connected to the amplifier, only connecting one channel per measurement. A frequency range from 50 Hz to 200,000 Hz was set, since the scan of the lower frequencies was increasing the measurement time drastically, and only the cutoff frequency was wanted in this experiment. Higher frequencies were excluded because they did not show any further results. The feedback resistance was set to a value of 1 kΩ. It was found that the comparison of the different OECTs is not directly possible. For an ideal comparison, the OECTs would have to use the same working point, which is not possible because of the measured tolerances within the lock-in amplifier. Applying a V_{DS} of -0.6 V for the devices with smaller sensing areas is possible, while for the devices with bigger sensing areas, an overload occurred. This problem could be solved by lowering the V_{DS}, which in return will also lower the cutoff frequency since lower amplitudes will be measured. An example can be seen in Figure 24. Independent from the ability to compare the devices the OECTs with the smallest channel size showed the highest cutoff frequencies. It was observed that an increase in V_{DS} causes a shift to higher frequencies until overloading occurs.

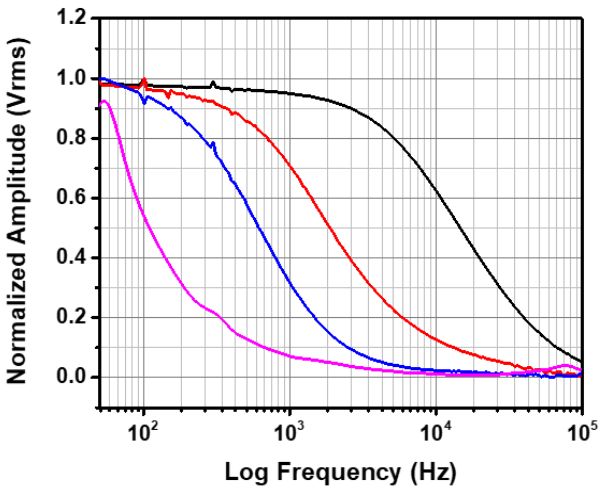

Figure 24: Measured cutoff frequencies for OECTs with different channel sizes as normalized amplitude over frequency. V_{DS} values for the 20×20 µm² (black) and 50×50 µm² (red) devices were -0.6 V, while the 100×100 µm² (blue) and 200×200 µm² (pink) devices were operated at -0.2 V.

Figure 24 shows the normalized curves for the amplitude in logarithmic scale. The cutoff frequencies in this measurement configuration increased when compared to the TTF box measurements. For the 200×200 µm² device a cutoff frequency was measured at 76 Hz, for the 100×100 µm² device it was at 353 Hz. The shift for the 50×50 µm² device was more severe with a cutoff frequency at 1000 Hz while the 20×20 µm² device had a cutoff frequency of 7700 Hz. Based on the limitations for the working point with lower V_{DS} for bigger sensing areas, the cutoff frequency increases with a decrease in polymer volume. This measurement showed that the lock-in amplifier is more suitable to detect the frequency response of the devices. This was not only based on the advanced hardware but also due to the fact that only one channel was connected which seemed to have a big impact on the measurements. That is why for further measurements of the frequency spectra with the TTF box single channels were connected instead of the usual configuration.

3.2.3 Noise Level

In this chapter, a short overview of the noise level of the used devices is given. In order to determine the noise level of the OECTs, the setup for the detection of action potentials of cells was used. A preamplifier with a feedback resistance of 3 kΩ is used in combination with a FET amplifier and MED64 software. This setup also enables the characterization of the devices before the noise measurement is performed. For characterization purposes, single channels were analyzed instead of 16 channels in parallel. The devices are characterized and set to their working point and measured with a sampling rate of 10 kHz. The main interest in the noise was based on the use of the devices for cellular action potential measurements. Low noise is necessary to identify cellular signals and achieve a high signal-to-noise ratio. For the different devices, different working points were set. Just as with the lock-in amplifier, the sensitivity of the devices with bigger sensing area was too high to set a proper working point when V_{DS} = -0.6 V was applied. So a gradual reduction in V_{DS} ensured that the working point could be set. The comparability of the individual devices in this experiment should be viewed critically since the g_m values and working points vary between the devices. The amplification factor as given by the product of the feedback resistance and the g_m has to be considered in this measurement. In order to circumvent the cutting of the signal, V_{DS} had to be reduced on the bigger devices leading to smaller g_m values in general. This experiment was therefore designed to determine the device performance and not as a comparison tool between the OECTs.
In the first approach, the noise of the devices was determined using NaCl with a conductivity of 10 mS/cm (Figure 25) measured over several minutes.

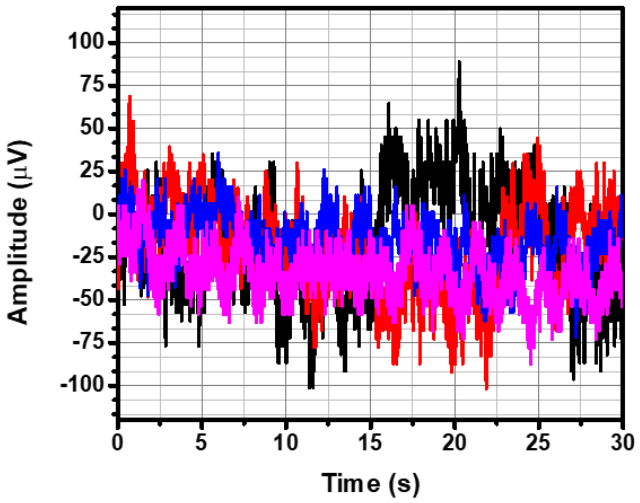

Figure 25: Noise of the OECTs with different sensing areas, measured in a NaCl buffer with a conductivity of 10 mS/cm (black: 20×20 µm², red: 50×50 µm², blue: 100×100 µm², pink: 200×200 µm²).

The noise spectra in Figure 25 show the noise of the OECTs with different sensing area sizes for 30 seconds, as a zoom in of measurements performed over 5 minutes. The amplitude of the noise appears to be quite homogeneous when comparing the different devices. Even though a difference between the different sensing area sizes can be seen, where the noise is increasing with decreasing sensing area. The measured amplitude of the 200×200 µm² devices is around 75 µV, 125 µV were measured for the 100×100 µm² devices. The 50×50 µm² devices came to a value of 175 µV, and the 20×20 µm² devices showed the highest noise with an amplitude of 200 µV. Since a trend could be seen, additional experiments were performed to evaluate the influence of the buffer conductivity on the measured noise level. The devices were set to their respective working points before the noise amplitude was measured (Figure 26). The measurement buffers were changed in order to alter the conductivity. The devices were set to the working point every time the buffer was changed, and the noise level was measured continuously for 5 minutes. As can be seen, the noise levels gathered were similar for the different buffers with a value of around 75 µV for a device with a 200×200 µm² sensing area.

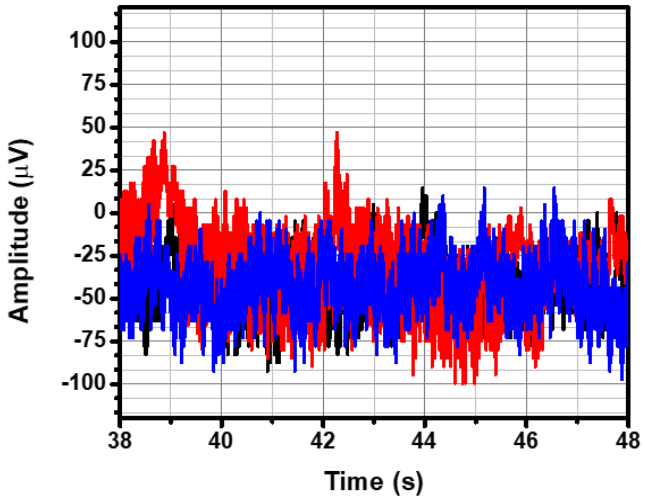

Figure 26: Noise of an OECT (200×200 µm²) measured with NaCl buffer with conductivities of black: 0.5 mS/cm, red: 2 mS/cm and blue: 10 mS/cm.

When compared to the spectra given in Figure 25, the same values can be measured for the devices with the same dimensions.

Due to their high g_m, the 200×200 µm² devices were tested containing the cell culture medium for HL-1 cells after being stored in an incubator under cell-culture conditions for three days. The working point was set at V_{DS} = -0.2 V and V_{GS} = 0.35 V, which resulted in a g_m of 10 mS. Out of the 16 channels, four channels were measured separately, and the results can be seen in Figure 27.

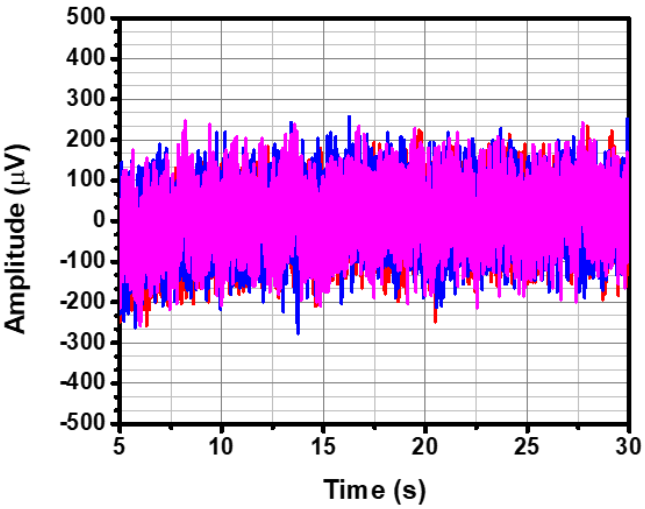

Figure 27: Noise of different channels of one 200×200 µm² OECT shown as an overlay graph.

It can be seen that the noise level is very small and constant within different channels. When compared to the data gathered in Figure 26, the noise level is increased to around 250 µV. This suggests an effect on the devices based on the measurement

being performed in medium or based on the time of the OECTs being stored in a cell incubator to simulate cell-culture conditions. This experiment was designed to evaluate the noise level under measurement conditions to determine the noise level that can be expected during the measurements with adherent cells.

3.2.4 Transparency

PEDOT:PSS is a polymer with a certain degree of transparency depending on its thickness. OECTs may offer the possibility of optical controls as well as optical-based assays, including fluorescence markers and others. In this chapter, transparency investigations regarding the OECTs are shown as measured with a UV-Vis spectrometer for the visible range (Table 3). The polymer was prepared on glass substrates using the same method as used for the OECTs. A blank glass chip was used as a reference.

Table 3: Transparency in percentage measured for different wavelengths in the visible spectrum

	Wavelength (nm)	**350**	**400**	**450**	**500**	**550**	**600**	**650**	**700**	**750**
Glass (reference)	Transparency (%)	100	100	100	100	100	100	100	100	100
One layer PEDOT:PSS	Transparency (%)	88.1	90.1	89.9	90.4	90.5	90.5	90.4	90.2	90.2
Two layers PEDOT:PSS	Transparency (%)	86.2	88.5	88.6	88.4	88.5	88.2	88.6	88.7	88.7
Three layers PEDOT:PSS	Transparency (%)	78.2	78.6	78.5	77.5	78.0	78.2	77.9	78.1	78.1
Drop of PEDOT:PSS	Transparency (%)	23.1	26.2	25.3	21.1	17.4	12.6	8.4	6.4	5.4

The PEDOT:PSS, as used for the OECTs, is represented by the results gathered for the single-layered PEDOT:PSS, it can be seen that the transparency is around 90 % throughout the visible spectrum. The transparency values are gradually decreasing with the number of layers and are the lowest for a glass chip with a dried droplet of

PEDOT:PSS. Under the microscope, a differentiation cannot be made between a single and a double layer of PEDOT:PSS as can also be seen by the measured values. The chips with three layers, however, appeared much darker than the single-layered chips. Since the optical transparency of the devices could be used for a variety of cell assays, measurements with fluorescently labeled cells were performed. MDCK cells were grown on the devices and killed with Triton X-100. Propidium iodide was used to mark the dead cells. Figure 28 shows one image taken with 40x magnification in an inverted microscope of the dead cells, stained with propidium iodide as an exemplary optical assay.

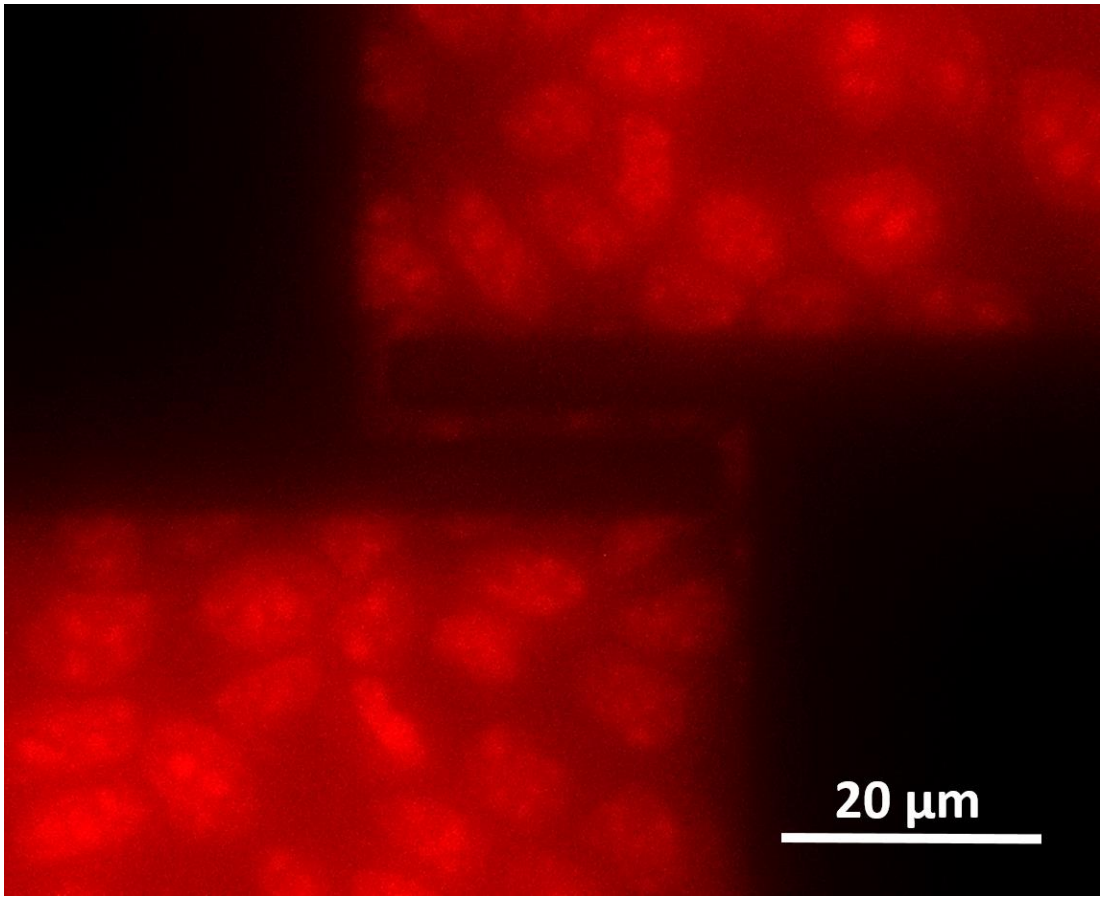

Figure 28: Image of an OECT sensing area (20×20 µm^2) with 40 x magnification in an inverted microscope, with adherent MDCK cells on the device surface. After the death of the cell, the propidium iodide can enter the cell and make them visible even through the gold fingers.

Individual cells can be seen in the gap between the gold fingers (measuring 5 µm) as well as around the gold fingers. The design of the devices, while not perfectly suited for optical assays still allows the observation of the cells through the device. In order to perform better optically-based assays, it would be necessary to increase the distance between the electrode fingers in order to use a smaller magnification factor.

3.2.5 Thickness

The thickness of the polymer layer was determined using atomic force microscope (AFM) measurements. Since the measurement of the same sample could not be performed due to the fabrication procedure, several wafers were prepared following the same treatment. The individual wafers were prepared with the PEDOT:PSS as described before. However, the devices were separated before EG was applied. Chips were taken from the center of the wafers with PEDOT:PSS being removed by cleaning the chips in water, with PEDOT:PSS without the use of EG as a secondary dopant and as completely prepared OECTs with PEDOT:PSS and EG. Since the chips were always taken from the same wafer, the difference in the wafer fabrication can be disregarded for these measurements. Several chips per wafer were tested and compared.

The chips were measured over a 35 µm distance which contained the edge of the sensing area opening, the sensing area, and two gold electrodes (Figure 29). The height was calculated as the difference between the highest point (ONO passivation) and the lower points (bottom of the sensing area, top of gold electrode and area between two electrodes).

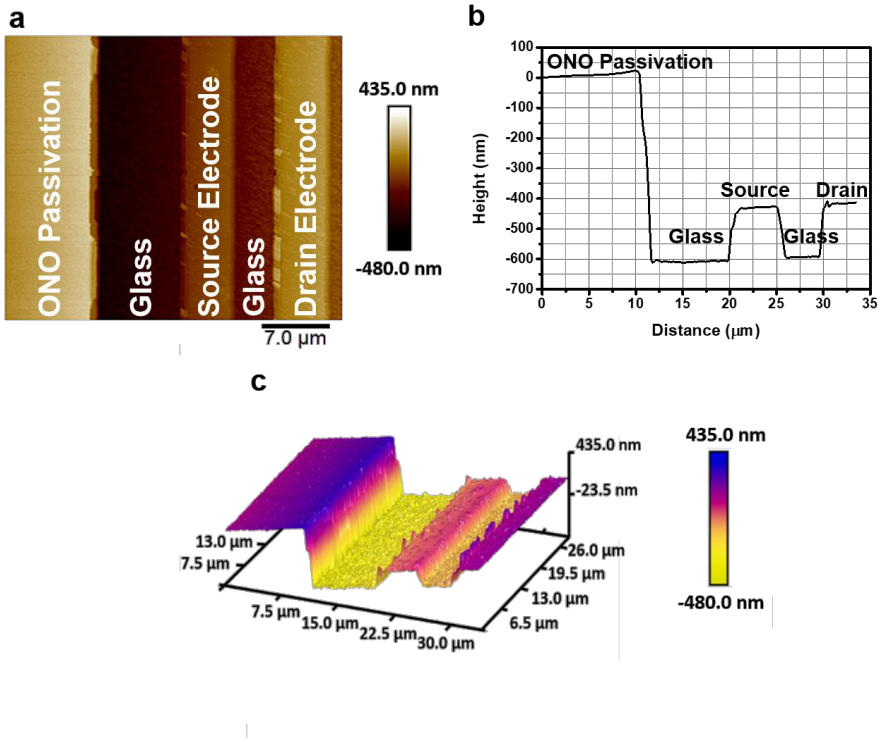

Figure 29: AFM data gathered from one exemplary OECT with PEDOT:PSS and the secondary dopant EG applied, a) image of the surface with the separate device areas indicated, b) AFM height profile for the device, c) 3D mapping of the OECT.

As shown in Figure 29 b the passivation has a height of around 600 nm to build a reservoir for the PEDOT:PSS during the spin coating process, furthermore the sacrificial layer of photoresist would add another additional layer on top of the passivation layer and increase the wall height. The behavior and the distribution of the polymer within the passivation opening, as well as the distribution on top of the gold electrodes, can only be measured with the AFM in a reliable way.
The measurements showed an average thickness of 42.33 nm for the PEDOT:PSS after EG treatment when comparing the height difference measured between the passivation and the bottom of the chip. On the gold electrodes, a thinner polymer layer with an average thickness of 31.16 nm is measured, and between the gold electrodes, an average of 63.16 nm is achieved. In general, thinner layers were measured without the EG treatment, where usually 10 nm less was measured in each case. This can be attributed to the change in composition that occurs due to the addition of EG. The variety in the thickness of the polymer layer is based on the different topography of the devices, with the distance between the passivation layer and the first gold electrode being significantly larger (~20 µm) than the distance between the gold electrodes (~5 µm). In the smaller gap, the movement of the polymer is limited, and other forces may apply, resulting in the thicker layer.

3.2.6 Roughness

The same AFM data was used to determine the roughness changes during the device processing. Roughness measurements can give information about changes in the polymer layer based on the chemical treatment and other factors. The area between the ONO stack and the first gold electrode was used for the measurements of the three device types. The main parameters considered are the root mean square average of height deviation taken from the mean image data plane (Rq) as well as the arithmetic average of the absolute values of the surface height deviations from the mean plane (Ra). These parameters are shown in Table 4 for the tested devices.

Table 4: Values for Rq and Ra based on the measured surfaces with blank glass, PEDOT:PSS without a chemical post-treatment with EG and PEDOT:PSS with the EG modification

Parameter	Glass	PEDOT:PSS	PEDOT:PSS after EG
Rq	10.8 nm ± 2.835 nm	12.7 nm ± 3.752 nm	13.4 nm ± 3.758 nm
Ra	8.41 nm ± 2.258 nm	10.4 nm ± 2.819 nm	10.9 nm ± 2.978 nm

As can be seen based on the results gathered in Table 4, the roughness of the blank glass increases with the deposition of PEDOT:PSS onto the glass surface. There is a minimal increase of the surface roughness after the EG post-treatment is applied to the devices. However, this change is overlapped by the standard error. The increase in surface roughness can be explained simply by the structure of the polymer. PEDOT:PSS possesses an amorphous structure which can be seen with the AFM as an increase in surface roughness. The change in roughness between the glass surface and the polymer layer after the EG treatment is 24.07 % for Rq and 29.61 % for Ra.

3.2.7 Conclusion

In this chapter, the initial performance tests of the fabricated OECTs were shown. Two fabrication methods were established and compared based on their resulting characteristics of the devices. While material printing enables a flexible deposition of PEDOT:PSS after device fabrication, independent from the substrate material, such devices lack the reproducibility and uniformity of spin coated devices. The printing technique relies on a certain randomness during the deposition, since the exact location of the polymer droplets could not be controlled with the used material printer. This lead to a pattern of at least two polymer drops overlapping each other. This created different electrical properties due to the variation in thickness. These variations showed a direct influence on the measured TC, the g_m, and the cutoff frequency. The devices were still useable for measurements since the sensitivity and operational principle were not affected by the fabrication method. However, experiments which rely on a comparison between devices in order to gain statistical values are harder to perform and will show a more significant inaccuracy.

Based on the gathered results, only spin coated devices were used for further experiments since their reliability and uniformity were seen as superior when compared to the printed devices. The devices showed solid characteristics for biosensing applications. The differently sized OECTs could be used for different measurement applications depending on the experimental requirements regarding sensitivity or

voltage restrictions. The devices showed high g_m values up to 35 mS with cutoff frequencies close to 10,000 Hz with very low noise. Moreover, the roughness and transparency offer additional bonuses. However, the exact thickness of the polymer layer cannot be controlled with the proposed fabrication method, since the devices show a variation in thickness based on the position of the polymer on the chip. The main influences were seen as the smaller area between two electrode fingers and the polymer layer on top of the gold electrodes. The averaged thickness of the polymer layer for the OECTs was found to be 42.33 nm, which resulted in a fast operation for the devices with small sensing areas. Due to the fabrication method, only an increase in spin coating rpm could lead to thinner layers while the uniformity should remain constant for the OECTs. As shown in this chapter, an increase in the cutoff frequency with a decrease in g_m would be expected in this situation, which might not be beneficial for the sensors. The roughness increased with the polymer deposition due to the amorphous nature of the PEDOT:PSS. Based on the data, the roughness change was uniform and not dependent on the thickness of the deposited polymer.

3.3 Physical and Electrical Stability of the Sensors

When performing cell-based assays, many requirements have to be fulfilled by the used sensors. Cell media, in combination with frequent medium changes, as well as, variations in temperatures and frequent measurements induce strain on the devices. The stability of biosensors towards these factors has to be investigated. Under normal cell-culture conditions, the device performance has to provide constant and accurate results, independent from the measurement environment. In the following chapter, the stability of the OECTs towards continuous measurements will be described.

3.3.1 Electrical Stability

The stability of the devices had to be evaluated for different situations of usage. Mainly the stability of the device immersed in a liquid is of interest for the performed experiments. This chapter focuses on electrical deterioration as it may occur by successive measurements or by the application of high voltages, as well as, on the deteriorative process that follows by keeping the devices immersed in liquid over several days.

In a first approach the electrical stability was tested in regards to the applied V_{GS} where the applied voltage ranged from -0.6 V to 0.8 V (Figure 30 a) and from 0 V to 0.8 V (Figure 30 b), a measurement was performed every 30 seconds for 20 consecutive minutes. The shown devices were 200×200 µm^2 devices with PBS as the electrolyte. The OECTs were kept with the PBS at room temperature for 5 minutes to enable the polymer layer to swell before the first measurement was started.

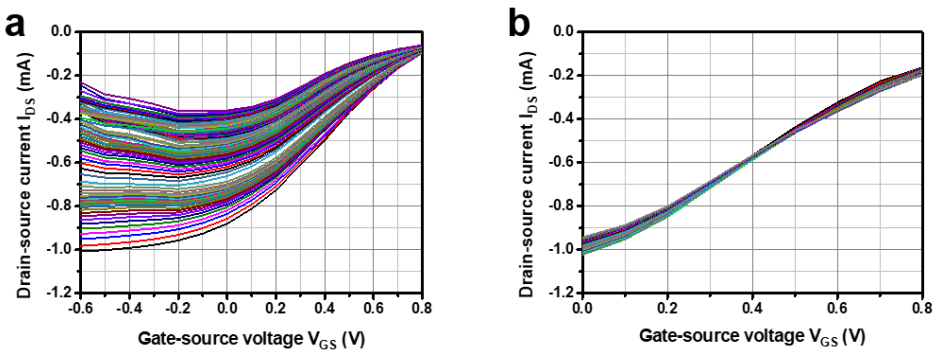

Figure 30: Stability of the devices while being measured every 30 seconds over 20 minutes. a) V_{GS} sweeps from -0.6 V to 0.8 V with a continuous decrease in measured I_{DS} and b) sweep from 0 V to 0.8 V. Every single line represents a performed measurement.

The measurements show a continuous decrease in I_{DS} following the successive measurements while applying V_{GS} starting from a negative range. These shifts of I_{DS} also cause a decrease in curve steepness reducing the g_m of the device gradually. The decrease in I_{DS} for the tested devices was permanent and could not be recovered to former values. While there also seemed to be a broadened beginning and end of the spectra for the devices tested within the positive voltage range the g_m, as well as the position of the working point, did not change. This result was found for all the used OECTs independent from their channel sizes. An increase of the gate voltage beyond 1 V lead to a total failure of the devices, in a similar way the drain voltage could not be increased above 1 V either without causing severe damage to the devices.

After the measurement range of the devices was confirmed, successive measurements of the TC were investigated right after the application of the measurement electrolyte. With this method V_{DS} and V_{GS} are applied every 30 seconds over a certain time. Figure 31 shows the TC curves of a single OECT channel for 7 minutes of measurements. The change after the first immersion in the liquid is the most prominent while all following curves show a very similar profile.

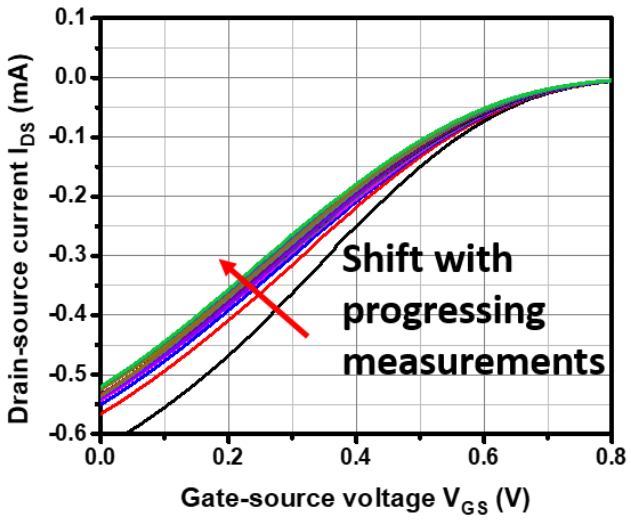

Figure 31: Successive TC measurements on a single channel plotted as IV curve.

It was generally observed, that the first few measurements showed a decrease in measured I_{DS} which can be seen for the first and the second measurements in Figure 31 with the black and the red line of the graph. After the first three measurements, the spectra stayed quite constant over the measured time period suggesting that a change in the PEDOT:PSS was induced by the initial measurements which affected the resulting spectra.

A similar approach is shown in Figure 32, where the g_m values are shown for a single channel of an OECT for 20 minutes of measurement. It can be seen that the g_m values seem to have a downward trend. However, the calculated difference in g_m over the performed measurements showed a value of 0.6 % over these 40 measurements.

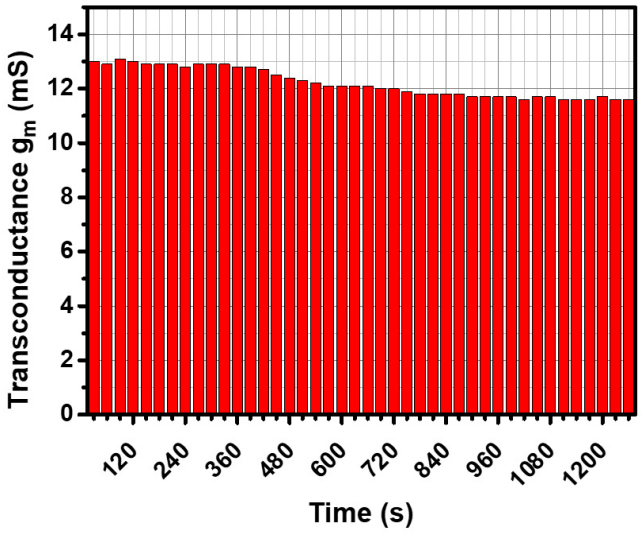

Figure 32: Stability of an exemplary 200×200 µm² OECT measured on a single gate over a time of 20 minutes with a measurement of the TC performed every 30 seconds (HEMPEL et al., 2017b).

Unlike the data presented before, Figure 32 focusses on the value of the g_m, not taking into account an eventually appearing shift in the working point. This causes the initial measurements not to show similar behavior as it was measured focusing on the I_{DS}, where the first measurements showed the biggest changes. As can be seen, the g_m is only affected in a minimal way when consecutive measurements are performed.

The performed measurements give an overview of the stability of the devices when they are measured in fast succession and when being measured more times than required in many cell related experiments. When performing cell experiments, a certain time for cell proliferation has to be included in the preparation procedures. So in order to test the stability of the OECTs in cell culture medium, the devices were kept in an incubator under cell culture conditions. Initial characterizations were performed with warmed cell culture medium and again after three days in the incubator (Figure 33).

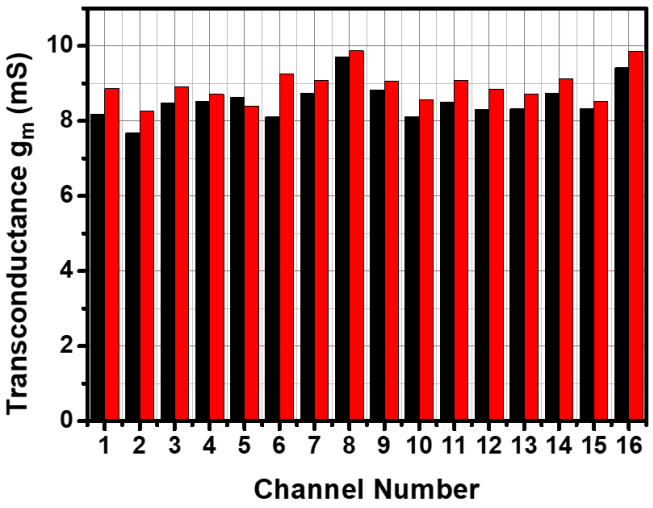

Figure 33: Stability of a 200×200 µm² OECT device tested in cell culture medium (medium for HL-1 cells). Black: Characterization in warm cell-culture medium after immersion. Red: After three days under cell culture conditions (HEMPEL et al., 2017b).

In Figure 33, a comparative increase in g_m can be seen between the measurements that were performed before and after the devices were kept in an incubator for three days. The average g_m of 8.53 mS with a standard deviation of 0.48 mS changed to a value of 8.90 mS with a standard deviation of 0.43 mS. This resulted in an increase of 0.4 ± 0.28 mS, which translates to 4.7 % over three days. This change can be caused by the removal of excess PSS due to the storage in liquid. Removal of PSS directly leads to higher conductivity and therefore a higher g_m. This effect was described previously in the literature (GRECO et al., 2011; LANG et al., 2009), however, without additional experiments, this phenomenon cannot be attributed with absolute certainty to such an effect.

Nonetheless, the experiments show the suitability of the devices with an apparent lack of deteriorative effects of the cell culture conditions on the OECTs at least for this short duration of time. Depending on the planned experiments, longer times might be needed and would have to be checked in addition to the performed experiments.

But not only the change in measured I_{DS} and g_m for consecutive measurements should be considered as the stability of the OECTs. Another important value is the drift of the devices that occurs over time when observing only I_{DS} (Figure 34).

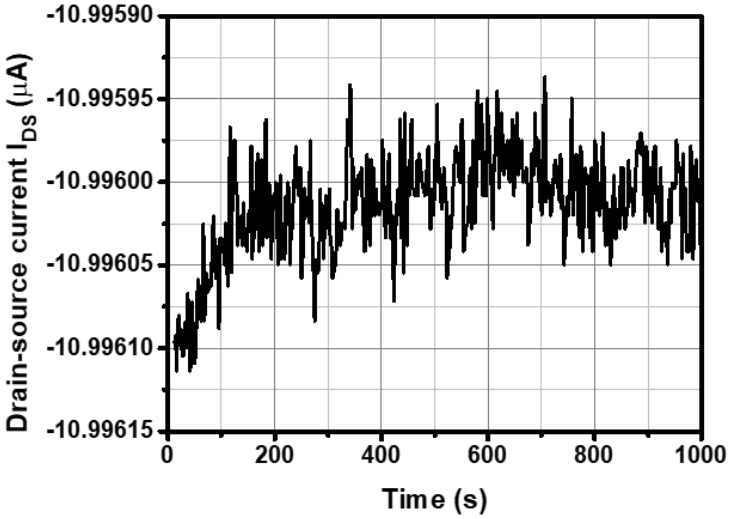

Figure 34: Measurement of I_{DS} over 16 minutes. After an initial drift, the signal stabilizes and remains constant.

The graph shows the measurement of I_{DS} over a time of 16 minutes. After an initial drift in the first three minutes, the curve stabilizes and remains the same over the whole duration of the measurement. The variation in measured current is very low, with a value of around 0.001 µA over the given time frame. Similarly, to the consecutive measurements where continuous TC measurements are performed, this experiment showed stability after an initial immersion of the devices in liquid. A drift did not occur, which enabled the devices to be used for overtime measurements as well.

3.3.2 Cyclic Measurements

An often used characteristic for electrical devices is the hysteresis, where the gate electrode voltage is swept from a initial value to a set value and back to the initial value. The resulting currents of the voltage sweep are measured. In the case of the OECTs, the Keithley parameter analyzer was used to apply the voltage sweep, and the device behavior was observed. The V_{DS} was kept at a constant value, and V_{GS} was applied from the lowest value to the highest value and back. Unlike cyclic voltammetry, the measurements were not looped continuously but were performed after each cycle with a gap of 30 sec.

In Figure 35, 20×20 µm^2 OECTs with a) 0.5 mS/cm NaCl and b) 10 mS/cm NaCl and their measured I_{DS} for a sweep from 0 V to 0.8 V and back to 0 V is presented. The frequency sweep to 0.8 V is analog to the basic TC measurement, with the sweep from

0.8 V back to 0 V a parallel line appears with overall lower I_{DS} values. There was a waiting time of 1 minute in between the individual measurements.

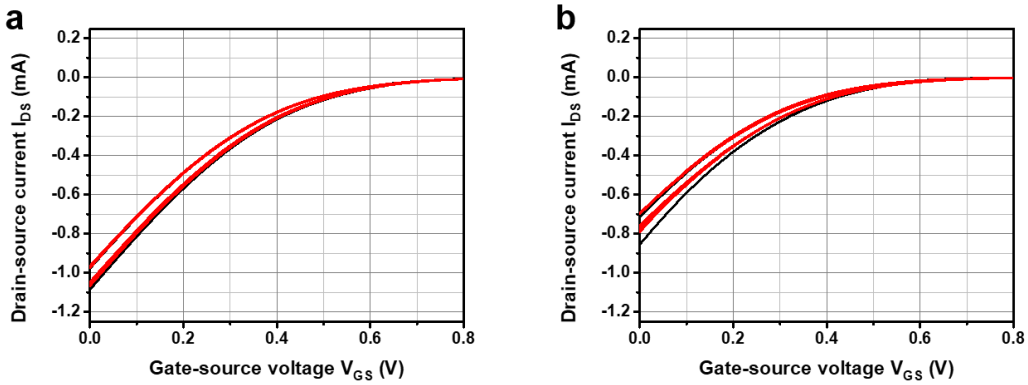

Figure 35: Cyclic measurements of OECTs where V_{GS} was applied from 0 V to 0.8 V to 0 V for 5 times on a) 20×20 µm² OECTs with 0.5 mS/cm buffer and b) same device with 10 mS/cm buffer.

It can be seen that the first measurement after the buffer was applied is an outlier (black curves) as already discussed in previous chapters, which can be attributed to the swelling of the material or the removal of surface-bound PSS, the initially measured I_{DS} is bigger than the values achieved by the successive measurements (red curves). As for the follow-up measurements, the same characteristics for the forward and backward measurements were recorded. The observed effect might be due to the gating mechanism of the OECTs by the cation influx into the polymer layer. The conductivity is depleted by the binding of cations, at a voltage of 0.8 V the cations are bound, and no conductivity is observed. When cycling back, the ions have to leave the polymer layer in order to restore the initial values. This procedure is driven by the applied voltage and the diffusion of the ions.

Since this is not resembling the graphs as usually seen by cyclic voltammetry measurements, the measurement range was increased. The new cycle was performed from -0.3 V to 0.8 V and back, and a shift in the measured current for successive measurements occurred (Figure 36).

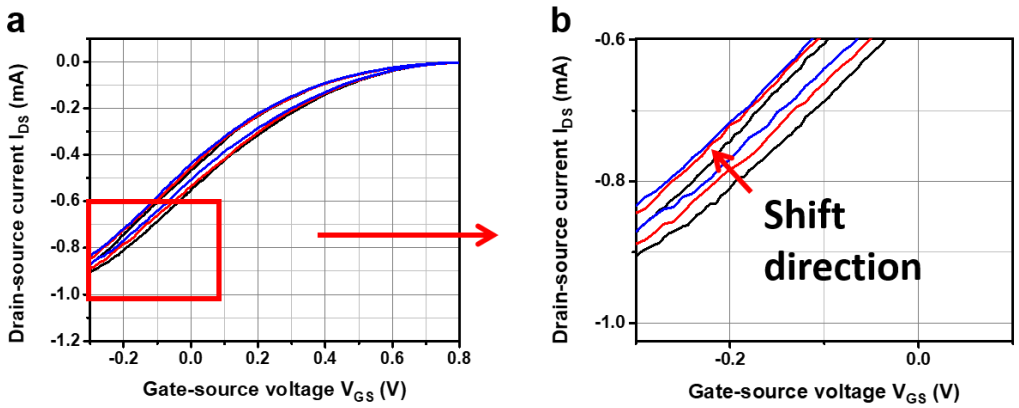

Figure 36: Cyclic measurements of OECTs where V_{GS} was applied from -0.3 V to 0.8 V to -0.3 V on a 20×20 µm² OECTs with a 0.5 mS/cm buffer a) whole measurement range b) the detailed view shows a gradual decrease in measured I_{DS} with an increasing amount of measurements.

Similar to the measurements shown in Figure 35, the backward curve shows an offset towards smaller I_{DS} values; however, a shift can also be observed for all further measurements. The effect appears to be deteriorative in a way that the measured I_{DS} keeps on decreasing for successive measurements. Since a change like this is not observed when the measurement range is set from 0 V and only directed in the positive voltage range for V_{GS}, it can be assumed that an electrical deterioration due to the applied voltage is causing these effects. A recovery of the device function to its initial values was not possible after the measurements were performed. The negative V_{GS} regimes should be completely avoided with the OECTs, while their function is still visible, the deteriorative process keeps on lowering the measured sensitivity, eventually leading to device failure. In order to maintain the reproducibility of the OECTs, measurements were performed from 0 V to 0.8 V throughout the other performed experiments.

3.3.3 Conclusion

The stability of the OECTs is affected by several factors and has to be considered during their application for any kind of assay. It was found that the voltage operation regime is crucial for short and long-term operation since the application of certain voltages leads to a fast device deterioration down to total device failure. This includes negative voltages but also higher voltages in any direction. Based on these results the sensitivity of the devices is electrically limited at a certain point. While an increase in V_{DS} also increases the g_m this procedure can be fatal for the devices. When the sensing

area size is reduced the g_m shifts to lower V_{GS} as can be seen in Chapter 3.2.1. At V_{DS} = -0.6 V for the 20×20 µm^2 devices V_{GS} is already at 0 V which means that for the full spectrum a sweep should start below 0 V which would also harm the devices. All these factors have to be taken into consideration since the dependencies in this case are quite complex and might limit the measurements.
Once the voltage operation is set to the appropriate values, a high stability of the OECTs was measured. The operation of the devices in liquid for several days shows no deterioration in device properties and even an increase in device performance can be measured. However, a deterioration for the devices was found for long exposures to liquids. After two weeks in liquid the device performance was significantly reduced. The deterioration effect is probably due to the water solubility of the polymer and could not be avoided with the presented fabrication protocol.

3.4 Investigation of an Ion Dependency

The working principle of the OECTs, as described in Chapter 1.2, suggests a different behavior based on the anions present in the measurement solution. In order to test this effect on the devices, several different buffers were used. Sodium chloride (NaCl), potassium chloride (KCl), calcium chloride ($CaCl_2$), and magnesium chloride ($MgCl_2$) solutions with conductivities of 0.5 mS/cm, 2 mS/cm, 10 mS/cm, 20 mS/cm and 30 mS/cm, with a pH of 7 were used. Experiments were designed to test for different possible effects caused by either the conductivity of the medium or the type of ions in the solution. Single and double charged ions can have different sizes which might affect their binding behavior and therefore affect the switching of the PEDOT:PSS. This investigation can help to understand the way the OECTs behave when exposed to cellular action potentials. The way the devices react to different ions could make them a selective tool for the sensing of certain ions when released by cells or enable the devices to distinguish between different cell types.

3.4.1 Influence of the Conductivity of the Measurement Buffer

While investigating the effect of the ionic strength, the different buffers were used during characterization. The results of one of these measurements are shown in Figure 37, where the TC and the g_m shift can be seen.

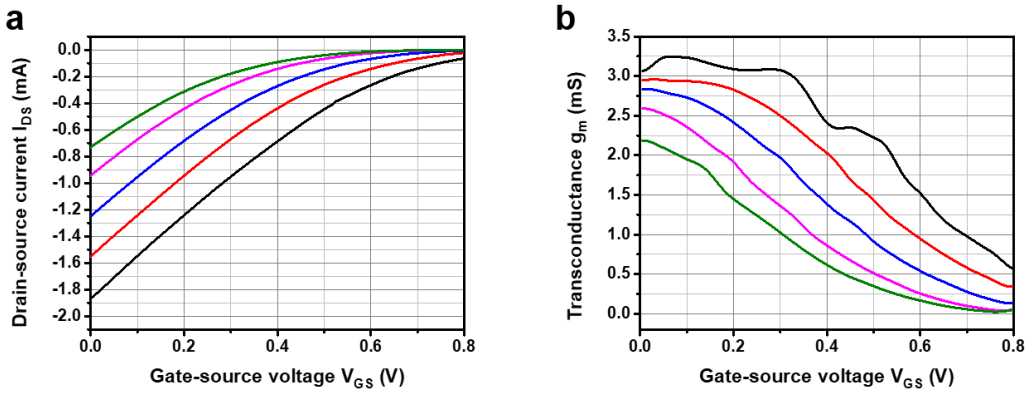

Figure 37: Change in a) TC and b) g_m, when changing the conductivity of the NaCl measurement buffer (black: DI water 10 µS/cm, red: NaCl 0.5 mS/cm, blue: NaCl 2 mS/cm, pink: NaCl 10 mS/cm, green: NaCl 20 mS/cm).

By increasing the conductivity of the measurement buffer, the whole curve shifts to lower V_{GS} values, which means that while keeping a positive V_{GS} for characterization and measurements, the measured I_{DS} is lower in comparison. This directly correlates to the g_m value decreasing by increasing buffer conductivity. An additional phenomenon is the shift of the working point to lower V_{GS}. The shift in measured current based on the conductivity of the medium therefore also causes a shift in the working point. This behavior had to be investigated for the different devices, also in regards to their cutoff frequency (Figure 38, Figure 22). When the conductivity of the electrolyte is increased, the number of ions in the solution is also increased. The data shows that a higher amount of cations leads to a faster dedoping of the polymer layer at lower V_{GS} values.

Figure 38 shows the influence of the conductivity of the measurement buffer on the devices with different sensing areas, while being measured at V_{DS} = -0.3 V. An increase in medium conductivity causes a shift of the TC spectra to lower V_{GS} values as can be seen for all the tested devices. This shifts the working point as well but can also cause different g_m values to be measured. The shift in the measured cutoff frequency increased with increasing buffer conductivity. It is important to point out that this behavior was uniform within the different devices.

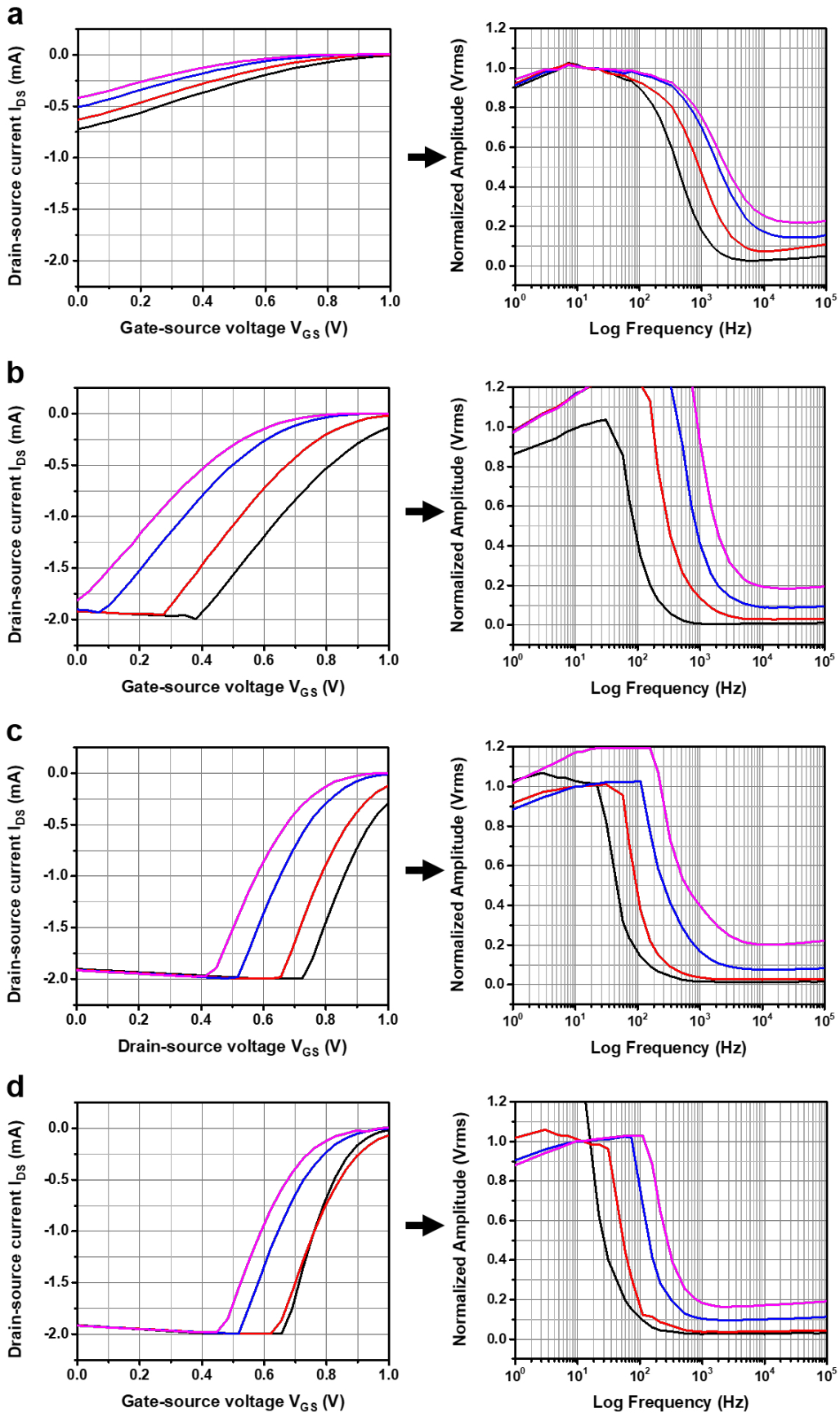

Figure 38: TC and cutoff frequency measurements for the OECTs with different gate sizes with black lines: NaCl 0.5 mS/cm, red lines: NaCl 2 mS/cm, blue lines: NaCl 10 mS/cm, pink lines: NaCl 20 mS/cm for a) 20×20 µm², b) 50×50 µm², c) 100×100 µm², d) 200×200 µm² devices.

3.4.2 Influence of the Ion Type

In a similar fashion, the effect of different cations was investigated by using KCl, NaCl, $MgCl_2$, and $CaCl_2$ with conductivities of 0.5 mS/cm, 2 mS/cm and 10 mS/cm (Figure 39). This experiment was designed to investigate if certain types of anions could be identified by a simple electronic readout.

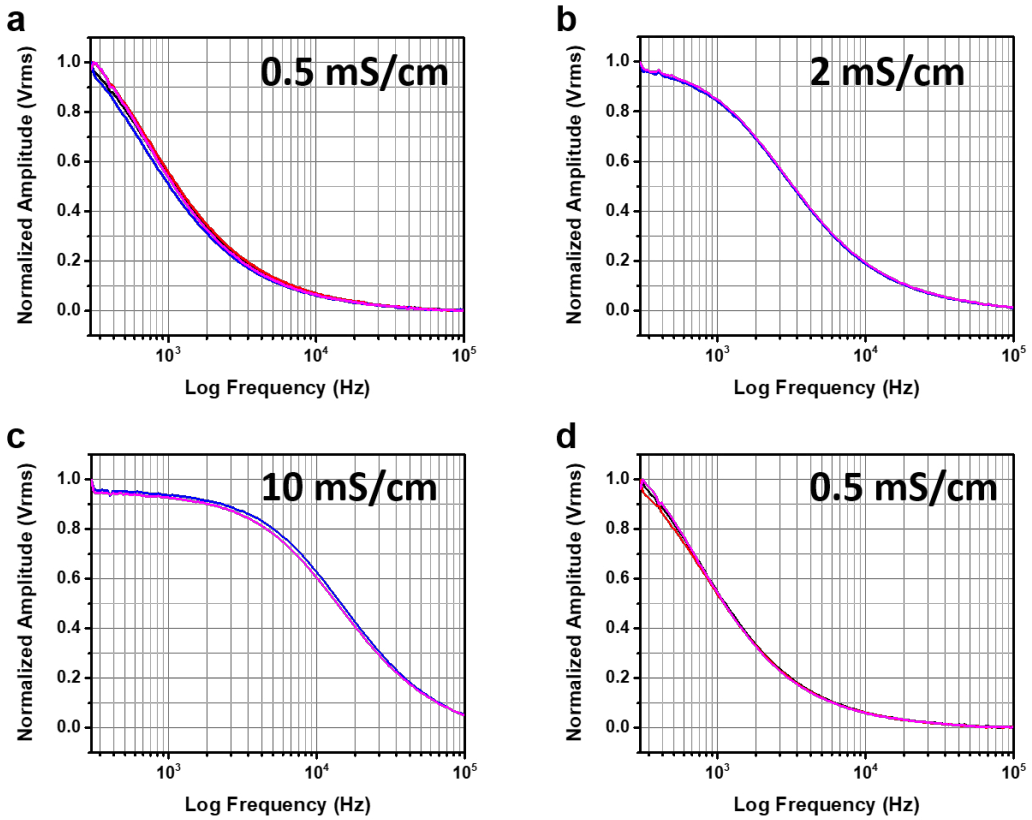

Figure 39: Measurement of the cutoff frequency on a single 20×20 µm² device with KCl (black), NaCl (red), $MgCl_2$ (blue) and $CaCl_2$ (pink) on the same channel. a) 0.5 mS/cm, b) 2 mS/cm, c) 10 mS/cm and back to d) 0.5 mS/cm.

Figure 39 shows the measurements for a device with the different ion type solutions. In most measurements the graphs overlay perfectly, so that no difference between the measurements can be seen. Overall an increase in the cutoff frequency with an increase in conductivity can be seen. For the 0.5 mS/cm solutions a cutoff frequency of 664 Hz was measured. For the 2 mS/cm solutions an increase to 1700 Hz was seen. The measurements showed a cutoff frequency of 7348 Hz for the 10 mS/cm solution. Finally, as last measurements the solution was exchanged for the 0.5 mS/cm buffers. The result was a shift of the cutoff frequency back to 644 Hz.

The conductivity of the measurement buffers directly correlates to the number of charge carriers, their mobility, and the charge. Since the conductivity was kept constant for the different solutions, the type of the used anion could have shown an effect on the measurements. Possible effects could be the size of the anion in solution. Ions in solution differ in size due to the number of electrons in relation to the number of protons, with additional size differences based on attracted water molecules. Therefore, it was assumed that different anions could show a specific spectrum during the measurements, especially regarding the cutoff frequency.
The performed measurements, however, showed no difference between the anions with single or double charge at the same conductivity. There is a shift to higher frequencies when increasing the conductivity as it was found before. For the entirety of the tested buffers, the shifts were consistent and only based on the conductivity of the solutions, independent of the type of ions in solution. The gathered data does not allow to attribute any kind of specificity towards certain anions to the used devices.

3.4.3 Conclusion

The measurements show a strong dependency of the OECT function based on the conductivity of the measurement buffer. A change in the conductivity of the buffer can cause a change in the measured I_{DS} combined with a change in the positioning of the working point and the cutoff frequency. In order to perform measurements, the medium conductivity has to be observed and controlled to keep the experimental conditions constant. Otherwise, false positives or negatives might be measured. The devices should not be set to the working point and then measured for different buffers with uncontrolled conductivities since this would lead to false conclusions.

3.5 Cellular Action Potential Measurements

As one of the pillars of traditional and modern cell biology assays, there is an unbroken interest in the detection of cellular action potentials. A model study was performed with HL-1 cells, and the results will be presented in this chapter. HL-1 cells are an established cell line that maintains the differentiated cardiomyocyte phenotype and retains the morphological, biochemical, and electrophysiological properties. Their behavior is similar to primary cardiomyocytes but with the ease of handling of cell lines. HL-1 cells offer a reliable and stable way of generating cellular action potentials. The cells start beating after three days in culture and offer a well understood and established platform. Since the detection is based on the generation of cellular action potentials, the HL-1 cells can function as a test setup to establish the OECTs for this purpose. The gathered data will be invaluable to transfer the measurement system to a variety of different cells, such as primary neurons.

3.5.1 HL-1 Cardiac Cell Experiments

In order to perform the cellular action potential measurements, the devices and cells were prepared as stated in Chapter 2. 200×200 μm^2 and 100×100 μm^2 OECTs were chosen for these measurements for two main reasons. First, the noise level measurements presented in Chapter 3.2.3 suggested the lowest noise for the OECTs while offering the highest g_m. Second, it was important to have a bigger area for the cells to adhere and generate action potentials since the cell outgrowth cannot be controlled, which might lead to the sensing areas not being covered by electrically active cells. After three days in culture, the devices were measured after an optical control under a microscope, where ideally contractions were spotted before electrical measurements were performed. The devices were characterized and set in their working point before the cellular action potentials were recorded. Exemplary measurements of spontaneous signals can be seen in Figure 40a for the 200×200 μm^2 devices. Figure 40b shows spontaneous signals measured with the 100×100 μm^2 OECTs.

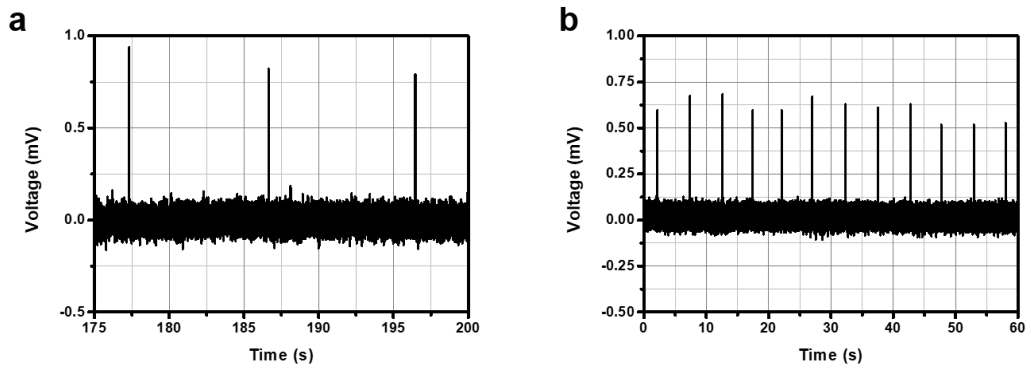

Figure 40: HL-1 signals recorded with an OECTs after three days *in vitro* a) 200×200 µm² device, b) 100×100 µm² device. Both measurements show signals with a maximum amplitude of 0.8 mV for the 200×200 µm² devices and 0.75 mV for the 100×100 µm² devices. The noise levels for both devices are around 100-200 µV.

When comparing both devices, the amplitudes measured with the smaller sensing area appear to be smaller, the measured noise levels, however, appear to be similar with peaking values of around 200 µV peak to peak.

The measured signals vary in amplitude based on the distance of the signal generating cell to the electrode. The sensing areas were chosen big enough to contain several cells and therefore, the exact location of the beating cells cannot be determined easily.

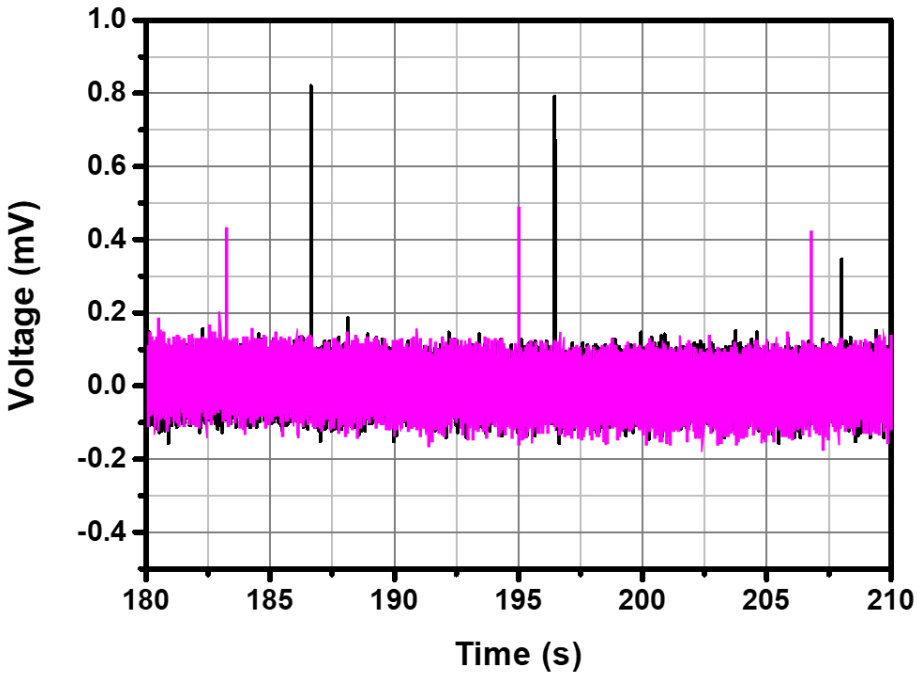

Figure 41: HL-1 signals recorded with an OECTs after three days *in vitro* on a 200×200 µm² device with two neighboring channels measuring the same signal.

Figure 41 shows the overlapping measurement of two channels and the occurring time shift for the same signal measured in two locations. The distance between the sensing areas was 200 µm. A time shift, as well as a variation in amplitude, can be observed between the two measured channels. While both channels operate in the same working point with the same g_m, the amplitudes vary around 0.35 mV between these channels. This effect can be caused by a number of reasons such as the distance of the electrically active cells to the sensing area or by the overlapping of cellular signals that are detected by a single sensing area.

By observing the signals in more detail, the signal shape can be evaluated. When zooming in on single signals fast component of the signal can be seen, while the slow component cannot be seen. Figure 42 visualizes this phenomenon for both device types.

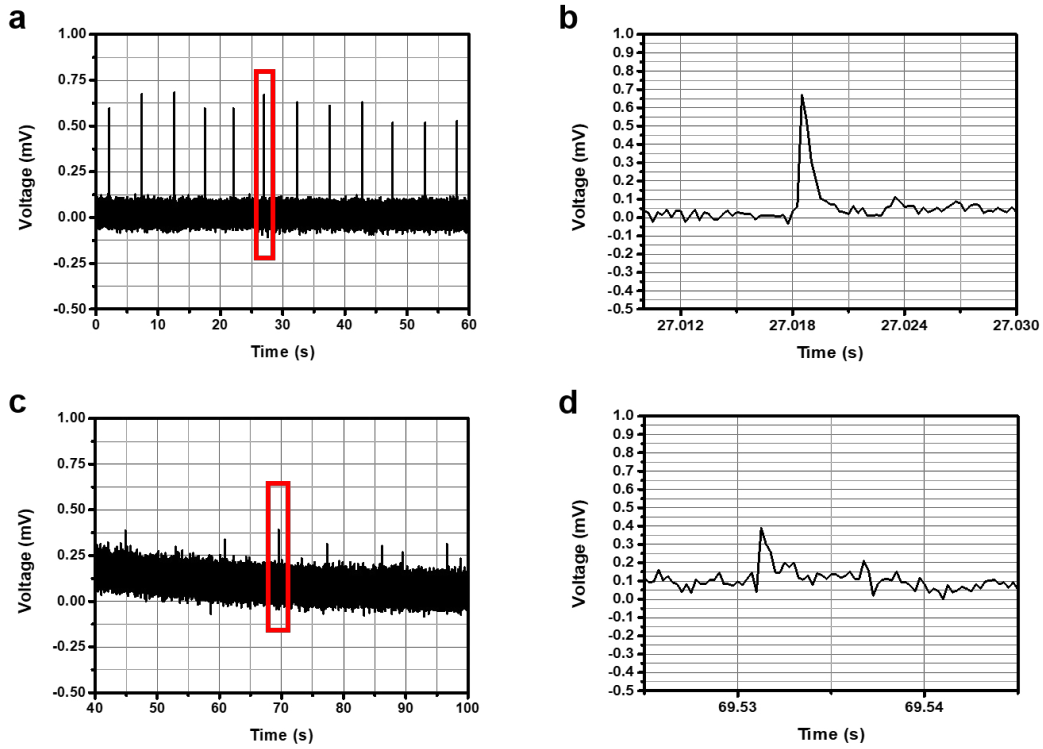

Figure 42: Action potentials as measured by an OECT after three days *in vitro*, a) 100×100 µm² device with b) detailed single signal, c) 200×200 µm² device with d) detailed single signal.

Independent from the used device type, the signal shape was matching throughout the performed experiments. Cell signals appear as peaks with varying amplitudes outside of the measured baseline. Signals appear as sharp peaks over a duration of 1 ms. This data is deviating from signals measured with other measurement methods where the signals usually consist of a positive and negative peak. Due to the obtained noise

levels, the negative peak might be overlapped by the noise and might not be visible in this case.

The performed measurements required a control to confirm that the measured signals were produced by the cells and not by other influences. Typically, a drug assay is performed in such cases to observe the frequency change depending on the administered drug. For HL-1 cells, norepinephrine can be used. The addition of norepinephrine to the culture medium should not change the amplitude of the signals and only show an influence on the frequency of the spontaneous occurring signals. Following this principle norepinephrine was administered to the cells in different concentrations, and the change in beats per minutes (bpm) was investigated (Figure 43). The concentration of norepinephrine was gradually increased until the signals stopped.

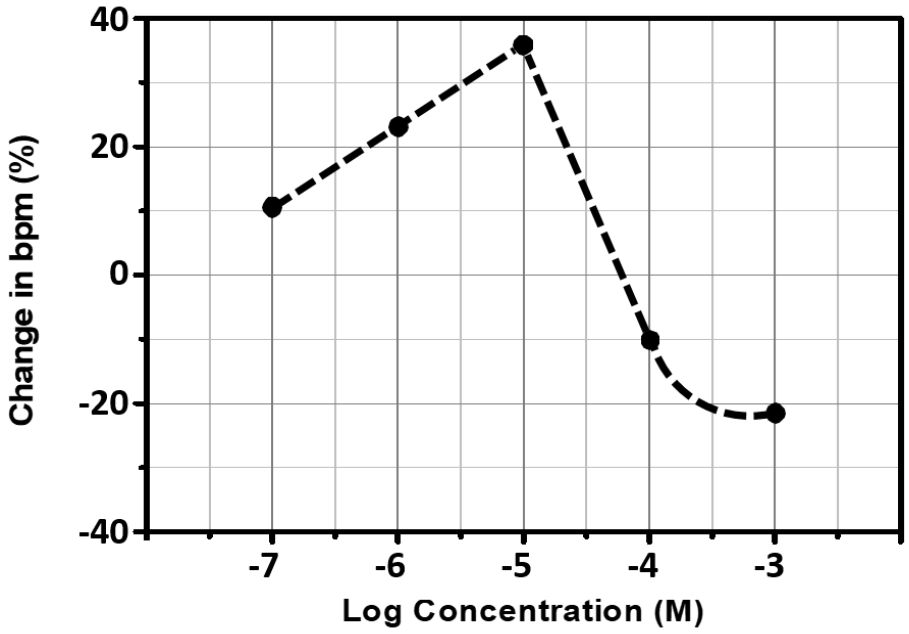

Figure 43: Bpm changes in HL-1 cells after the administration of different concentrations of norepinephrine (0.1 µM – 1 mM) (HEMPEL et al., 2017b).

By adding norepinephrine, the beating rate of the cardiac cells is affected due to the binding to the G-protein coupled receptor. This binding leads to an increase in calcium current activity, which increases the frequency of the measured signals. As can be seen in Figure 43, there is a linear increase of the measured bpm for the concentration range from 0.1 µM to 10 µM up, while from a concentration of 100 µM the termination of the beating can be observed.

3.5.2 Conclusion

The tested OECTs show suitability for cellular action potential measurements based on the used HL-1 cells due to their high signal-to-noise ratio combined with their stability in cell culture medium. The used devices had a big sensing area, which exceeded the size of the cells. Therefore, many adherent cells were located on the device surface. However, the devices showed the detection of action potentials in a reliable way. A decrease of the sensing area causes a higher signal-to-noise ratio when the sensing area is covered with a cell. A tight coverage of the sensing area would block outside influences from other cells. However, the growth behavior of the HL-1 cells cannot be influenced in a way that perfect coverage can be guaranteed. In contrast to spectra obtained by other measurement methods only the fast peaks that seem to contain the depolarization and repolarization of the cell can be observed. The other possible components of the cellular signal cannot be seen within the noise of the device.

3.6 Cell Impedance Measurements

In this chapter, the performed impedimetric measurements are explained, and the gathered data is shown for exemplary devices. To achieve a sensor platform for single cell analysis, confluent cell layers were investigated first, with a stepwise reduction of the cell number. The measurement of confluent cell layers also evaluates the suitability of the devices for a wide range of applications such as wound healing and cell migration. In general, the confluent growth of cells on top of the sensor is achieved easily, since the cellular outgrowth happens naturally. The reduction of the cell number towards single cells, however, requires a more advanced approach. In general, cell-impedance measurements can give insight into the binding behavior of cells, as well as their growth and migration. Since the devices are transparent and highly sensitive, the experiments were performed to understand how the fabricated OECTs pair against the already established platforms.

3.6.1 HEK Confluent Cell Layers

Due to the ease in experimental configuration, cells were seeded on the device surfaces of 200×200 μm^2 chips. The measurements were performed with the TTF box achieving a parallel readout of all the 16 channels (Figure 44). It was observed that the measured signal differed between channels but that the general shift was constant. A shift occurred to lower frequencies when adherent cells were at the surface. After cell removal by trypsinization, the curve shifted to higher frequencies.
Negative controls were performed to ensure that the shift was only happening due to cell adhesion. Therefore, devices without adherent cells were treated the same way as the chips containing cells. However, there was no shift detectable.

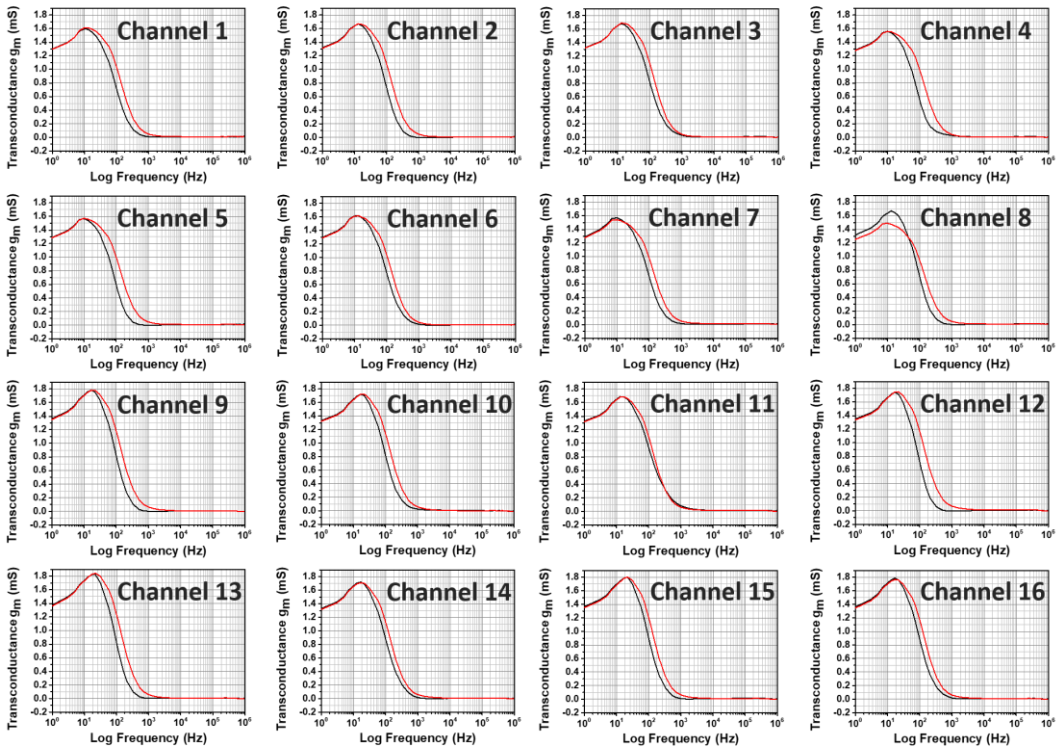

Figure 44: Measurement of 16 channels of an OECT (200×200 µm²) with a shift to lower frequencies due to cell adhesion (black) and shift to higher frequencies after cell removal by trypsin (red).

This platform was then used to test a cell-killing assay, which can be observed by fluorescence microscopy with a parallel electrical readout. In this assay, HEK cells were grown on the devices in various densities, loaded with calcein and then killed by human T-killer cells. As initial positive control experiments, HEK cells were loaded with calcein and then electronically and optically observed while Triton X-100 was added. Triton X-100 is a non-ionic surfactant used for the permeabilization of cell membranes. Its polar head group disrupts the hydrogen bonding in lipid bilayer while it is inserted into the cellular membrane, ultimately destroying the membrane integrity. The effect of Triton X-100 was very rapid and removed the fluorescence created by the calcein staining while adherent cells remained on the device surface. Figure 45 shows the shifts of the TTF spectra before the calcein staining was performed, 5 minutes after the calcein staining had ended and after the addition of Triton X-100 to the culture medium.

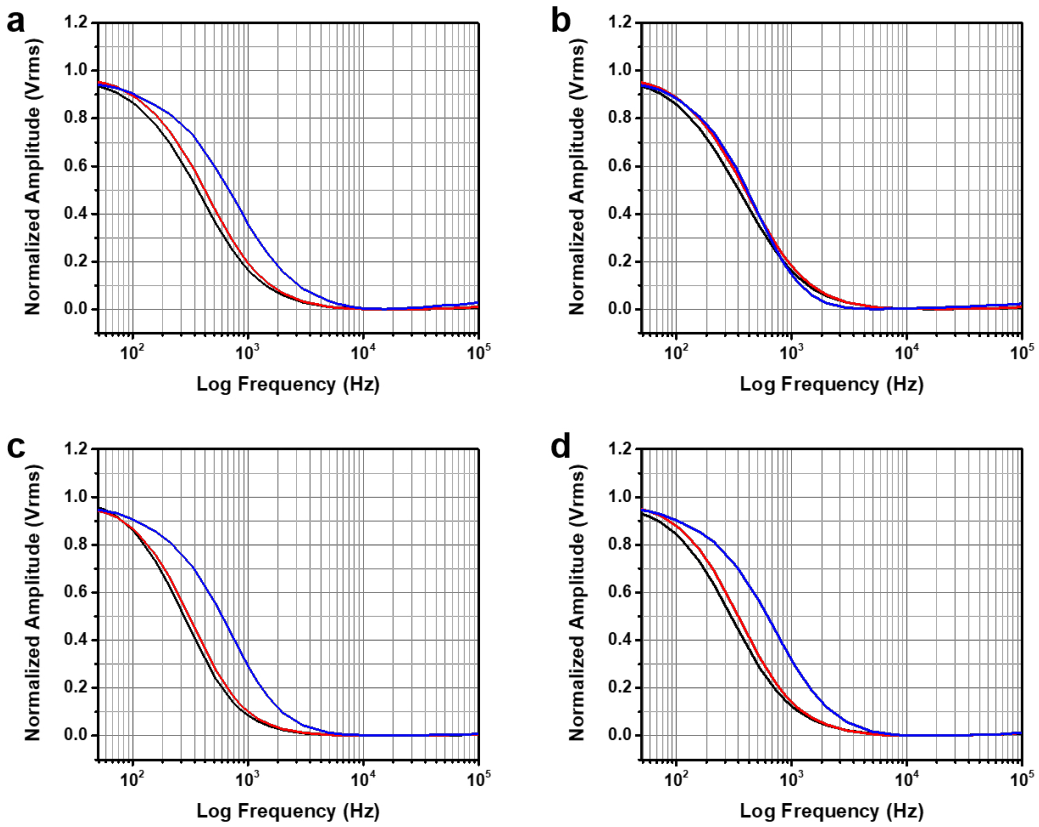

Figure 45: Measurements of the TTF spectra of several channels a) – d) of 200×200 µm² OECTs, with b) as control channel where DI water was added instead of Triton X-100 (black: before calcein staining, red: after 5 minutes with the calcein staining finished, blue: after the addition of Triton X-100).

It can be seen that there is a clear shift to higher frequencies due to the addition of Triton X-100. At the same time, the control chips which were given DI water instead of Triton X-100 showed no shift. The optical control of the experiment can be seen in Figure 46.

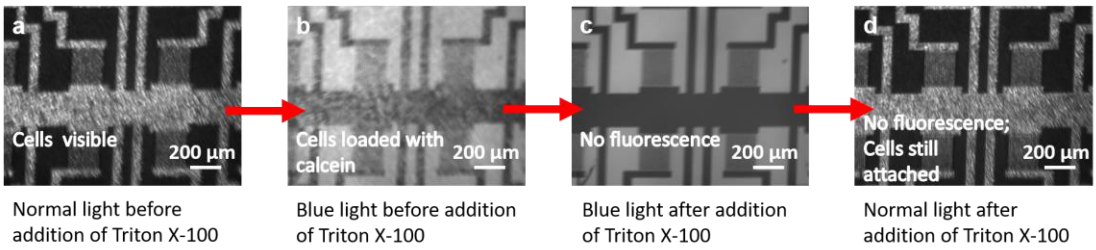

Figure 46: Optical control of the experiment. a) cells visible in normal light, b) cells visible due to the fluorescence of calcein, c) cells not visible due to the addition of Triton X-100, d) cells visible in normal light.

Figure 45 and Figure 46 show the electrical and optical reaction of the cells towards the addition of Triton X-100. Since the cell membranes become more permeable the

shift to higher cutoff frequencies is observed, while the cells remain attached to the surface.

In the next step, human T-killer cells were used on HEK cells, and the experiments were followed electronically. An exemplary result can be seen in Figure 47.

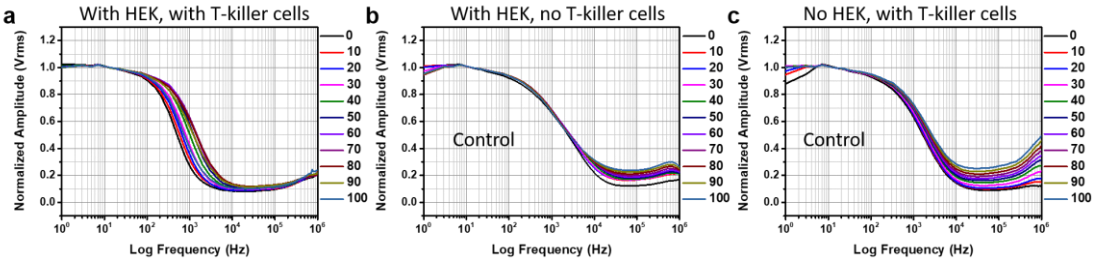

Figure 47: Measurement of several OECTs with exemplary results a) measurement of the device with adherent HEK cells and T-killer cells b) control chip with adherent HEK cells, but without T-killer cells c) control chip without adherent HEK cells, but with T-killer cells.

The data shows a shift to higher frequencies when using the spectra as a marker over time after the addition of T-killer cells the shift is reaching a maximum after 70 minutes. After reaching the 70-minute point, a shift to lower frequencies occurs (Figure 48). Other than that a different behavior in the high frequencies over 10,000 Hz can be seen which appears most prominent when there are no HEK cells on the device surface and still visible with adherent HEK cells but without T-killer cells.

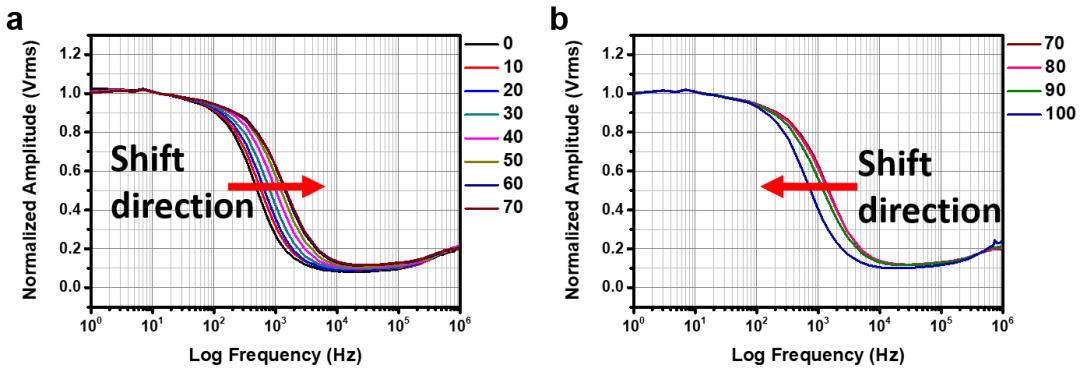

Figure 48: Shift in detail for the graph shown in Figure 47a, a) for the measurement up to 70 minutes a shift to higher frequencies can be seen; b) after 70 minutes a shift to lower frequencies occurs.

The corresponding optical images to this experiment are given in Figure 49, where the before and after state is shown. The HEK cells can be seen as a dense layer on top of the device (Figure 49a). After 100 minutes with T-killer cells, the image looks to be more grainy, as if the cell number increased (Figure 49b).

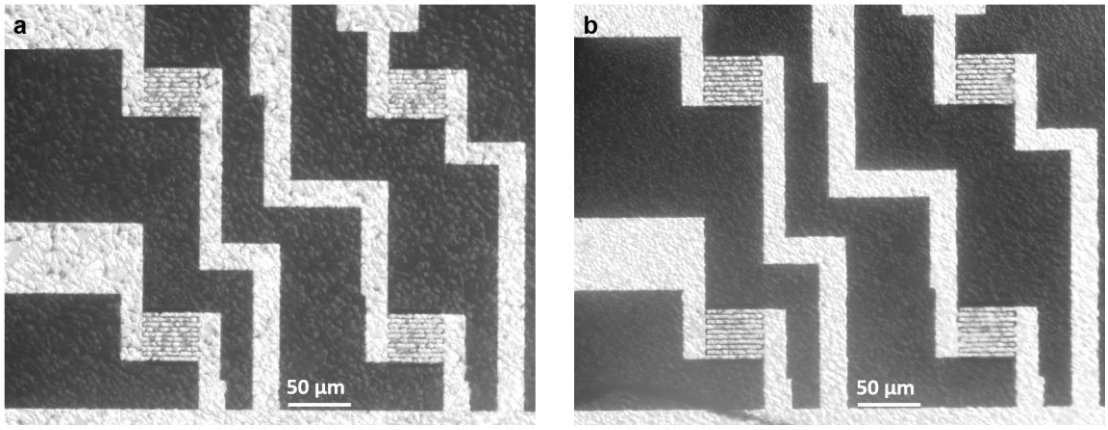

Figure 49: Microscopic images of the OECT in Figure 47a and Figure 48 with a) HEK cells before the addition of T-killer cells and b) after 100 minutes with T-killer cells.

A similar result can be found in Figure 50, where the initial density of HEK cells was lower than the one displayed in Figure 49.

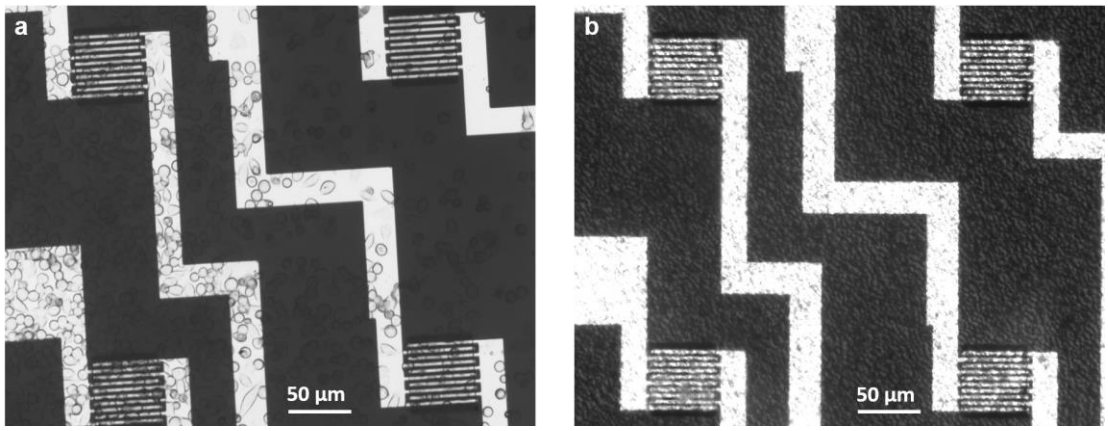

Figure 50: Microscopic images of a) HEK cells before the addition of T-killer cells and b) after 100 minutes with T-killer cells.

Again, it can be seen that the amount of surface-bound cells increases after 100 minutes after the T-killer cells were added to the HEK cell culture. The impedance spectra show this same behavior where the T-killer cells cause the detachment of the HEK cells from the surface by induced apoptosis. By detaching from the device surface, the spectrum is shifting to higher frequencies. This process is then followed by the attachment of the T-killer cells to the OECTs, which is again causing a shift in the spectra but to lower frequency values. The attached T-killer cells can be seen optically and can be identified by their shape and cell number, which is differing from the HEK cells.

3.6.2 HEK Single Cell Measurements

The next task was to investigate the possibility of using the OECTs with a small sensing area for cell measurements. The sensing area of 20×20 μm^2 size was designed to fit a single cell and gain data based on the adhesion due to such a small binding event. To realize this experiment, the cell numbers were reduced significantly while all the other culturing conditions remained the same.

While not all the sensing areas could be covered by exactly one cell, an average of five sensing areas was covered for every single experiment. It was always possible to have at least one empty sensing area which was then used as a control. Figure 51 shows an exemplary adherent cell on the sensor surface, where the cell was not covering the whole sensing area. For the single cell experiments sensing areas covered by only one cell were used. The cell culture medium was replaced by fresh, pre-warmed medium 30 minutes before the measurement was performed. The trypsinization was performed by removing the measurement medium and replacing it with trypsin for 5 minutes until all the adherent cells detached. Afterward, fresh and pre-warmed medium was added to the devices, and the measurements were performed after the OECTs were kept for 30 minutes under cell culture conditions.

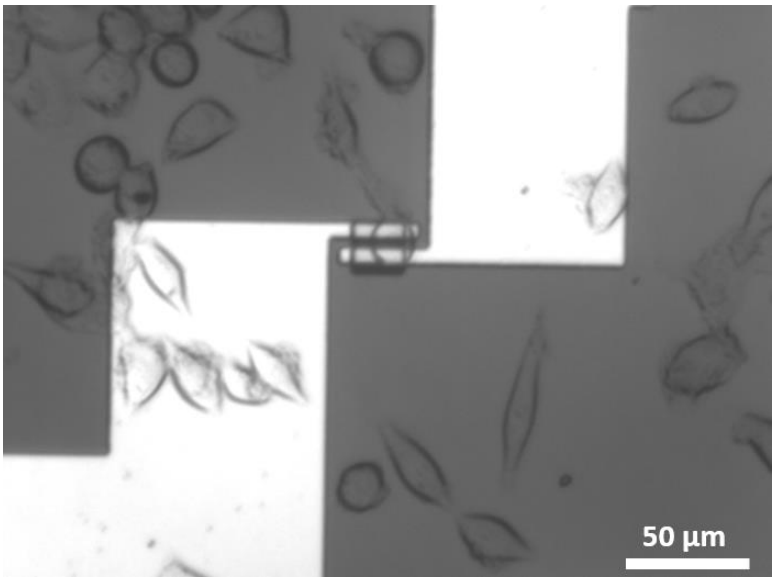

Figure 51: Microscopic image of a single HEK cell attached to one sensing area of the OECT.

The grown cells could be removed chemically by the addition of trypsin, and the corresponding spectra were measured for 20×20 µm^2 OECTs with the lock-in amplifier and with the TTF box (Figure 52, Figure 53, Figure 54).

Figure 52a shows a single sensing area almost completely covered by a single cell. In Figure 52b the cell is removed by trypsinization with the corresponding spectra for the lock-in in Figure 52c and the spectra measured by the TTF box in Figure 52d.

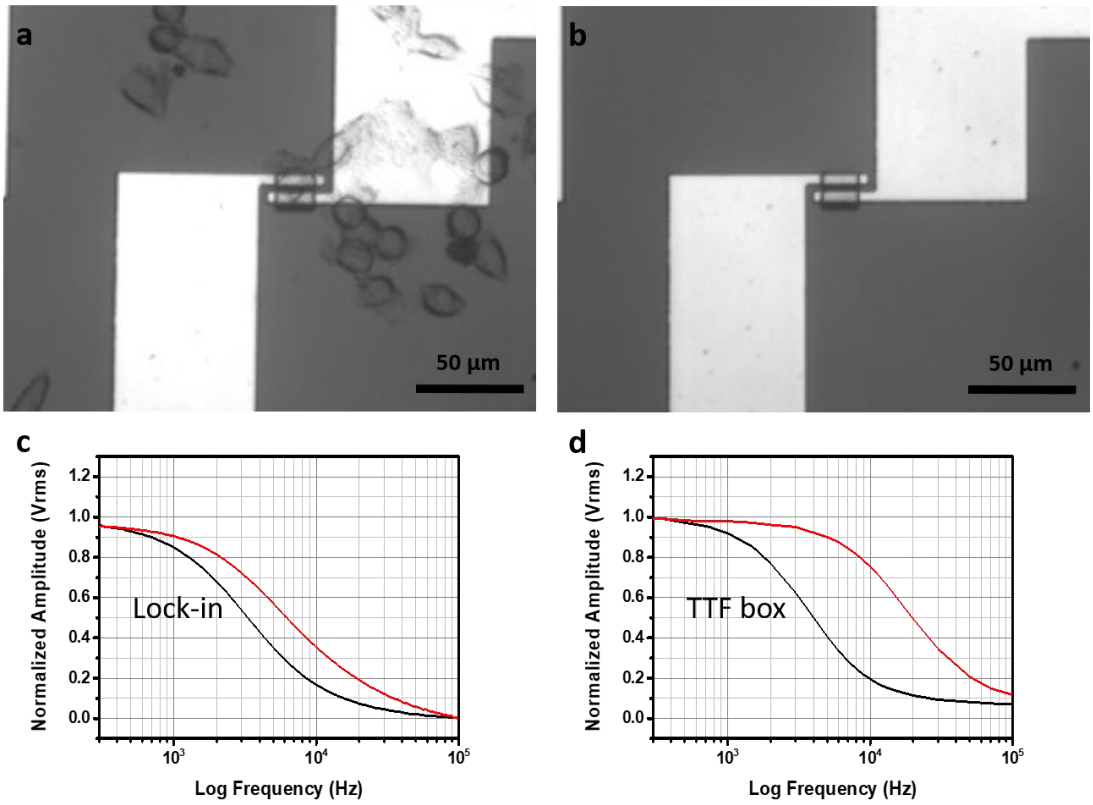

Figure 52: Microscopic image of a 20×20 µm^2 OECT with a) adherent cell; b) after cell removal by trypsin, with the measured spectra for those two states c) measured by lock-in amplifier (black: with adherent cell, red: with removed cell); d) measured by the TTF box (black: with adherent cell, red: with removed cell).

The cells were fully removed from the device surface, and the condition of the medium was kept the same to prevent effects of different salt concentrations or conductivity changes due to the culturing conditions. It can be seen that the results vary between the two measurement methods where a slight shift in the cutoff frequency can be observed. For the lock-in amplifier the cutoff frequency shifts from 1800 Hz when the cell is adherent to 3165 Hz once the cell is removed. For the TTF box the cutoff frequency is shifted from 2400 Hz with the adherent cell to 11,530 Hz once the cell is removed. The differences between cell-covered sensing area and cell-free sensing area are way bigger for the TTF box measurements. Also, the overall shape shows differences between the measurement methods, which does not allow these methods

to be compared directly. However, the results are the same, with a lower cutoff frequency for the cell-covered sensing area and a shift to a higher cutoff frequency for the cell-free sensing area.

Another example is shown in Figure 53, with the attached cell in Figure 53a and the empty sensing area after cell removal in Figure 53b. The cell body shape is different from the previously shown example. The measured spectra show the same results but again with a bigger change for the TTF box (Figure 53c and Figure 53d).

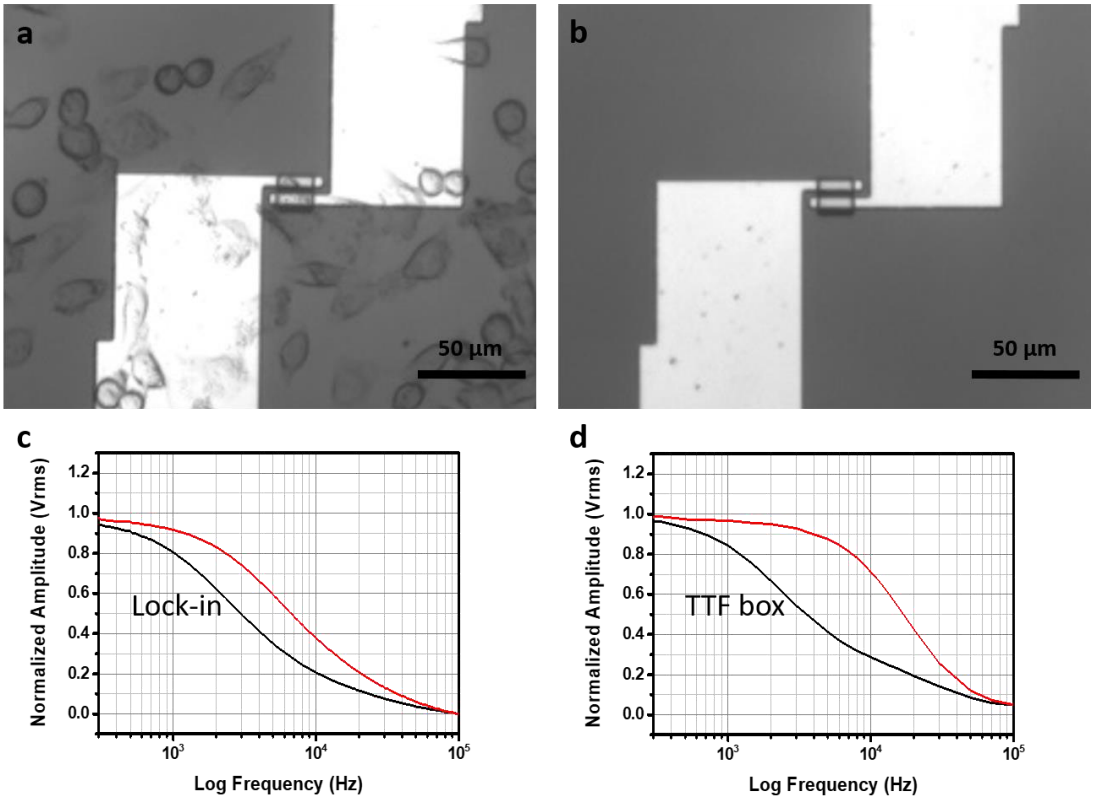

Figure 53: Microscopic image of a 20×20 µm² OECT with a) adherent cell; b) after cell removal by trypsin, and the measured spectra for those two states c) measured by lock-in amplifier (black: with adherent cell, red: with removed cell); d) measured by the TTF box (black: with adherent cell, red: with removed cell).

For the measurement performed with the lock-in amplifier Figure 53 shows the shift of the cutoff frequency from 1497 Hz to 3432 Hz, when the cell is removed. As seen in Figure 52 the change in the frequency spectra is bigger for the measurements with the TTF box. The cutoff frequency changed from 1730 Hz to 10,094 Hz after the cell was removed. To exclude environmental influences on the results control measurements were performed. It had to be shown, that the chemical treatment, as well as the changing of the measurement medium, did not affect the devices. An exemplary control measurement is shown in Figure 54. It can be seen that there was no cell attached to the sensing area at the beginning of the measurement (Figure 54a), and

naturally this did not change after the trypsinization (Figure 54b). The measured spectra show at best insignificant changes due to the process of chemical cell removal or the measurement method (Figure 54c and Figure 54d).

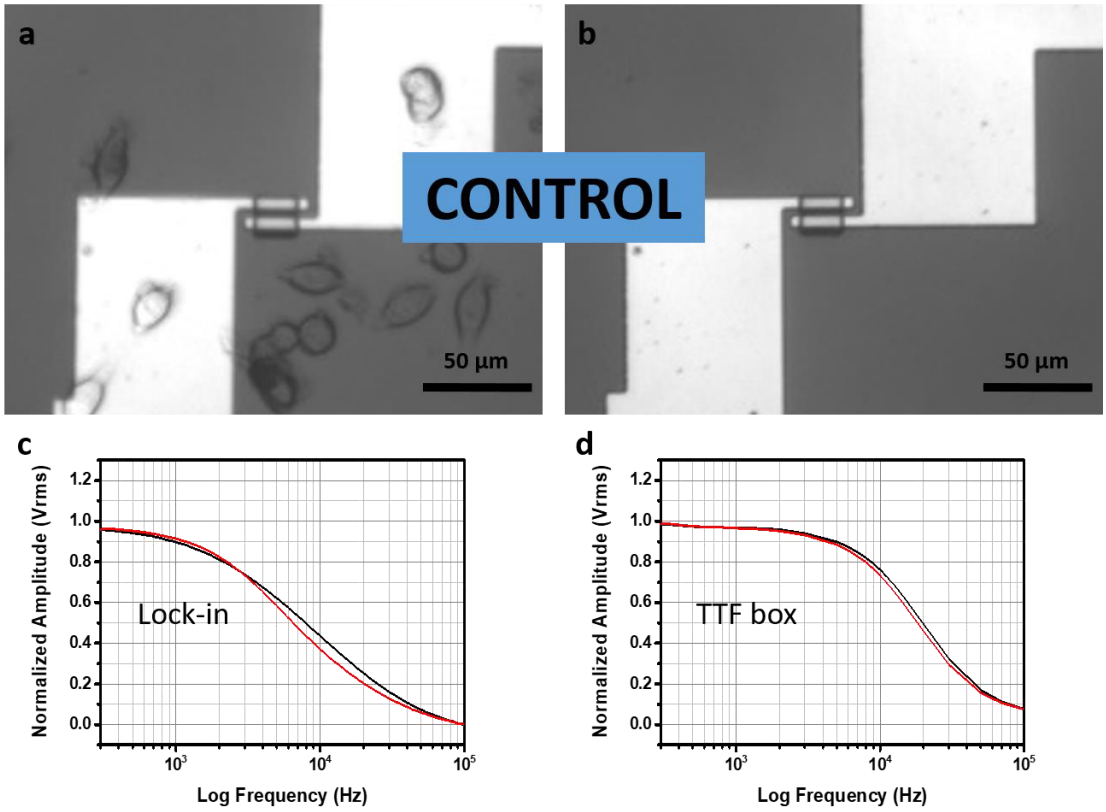

Figure 54: Microscopic image of an 20×20 µm² OECT as a control measurement with a) and b) showing no adherent cell before and after trypsin treatment, respectively, and the measured spectra for those two states c) measured by the lock-in amplifier (black: with adherent cell, red: with removed cell); d) measured by the TTF box (black: with adherent cell, red: with removed cell).

For the control channels the cutoff frequency was the same before and after the measurement. The lock-in amplifier achieved a value of 3400 Hz, while the TTF box measured a value of 11,225 Hz as the cutoff frequency. Overall a high consistency over the tested devices was found. The shifts in the frequency were confirmed for single cell measurements when chemical removal of the cells was performed.

In order to detect the detachment of individual cells, a patch clamp setup was used to remove a single cell from the OECT surface mechanically. This method guarantees that the measured effect is solely attributed to cell adhesion. The devices were prepared the same way as described before. The medium of the cells was changed 30 minutes before the measurements were performed. The medium did not have to be changed after cell removal since nothing was changed during the measurements.

The spectra were measured under the microscope in order to observe the cells and to be able to remove them with the patch clamp pipette (Figure 55).

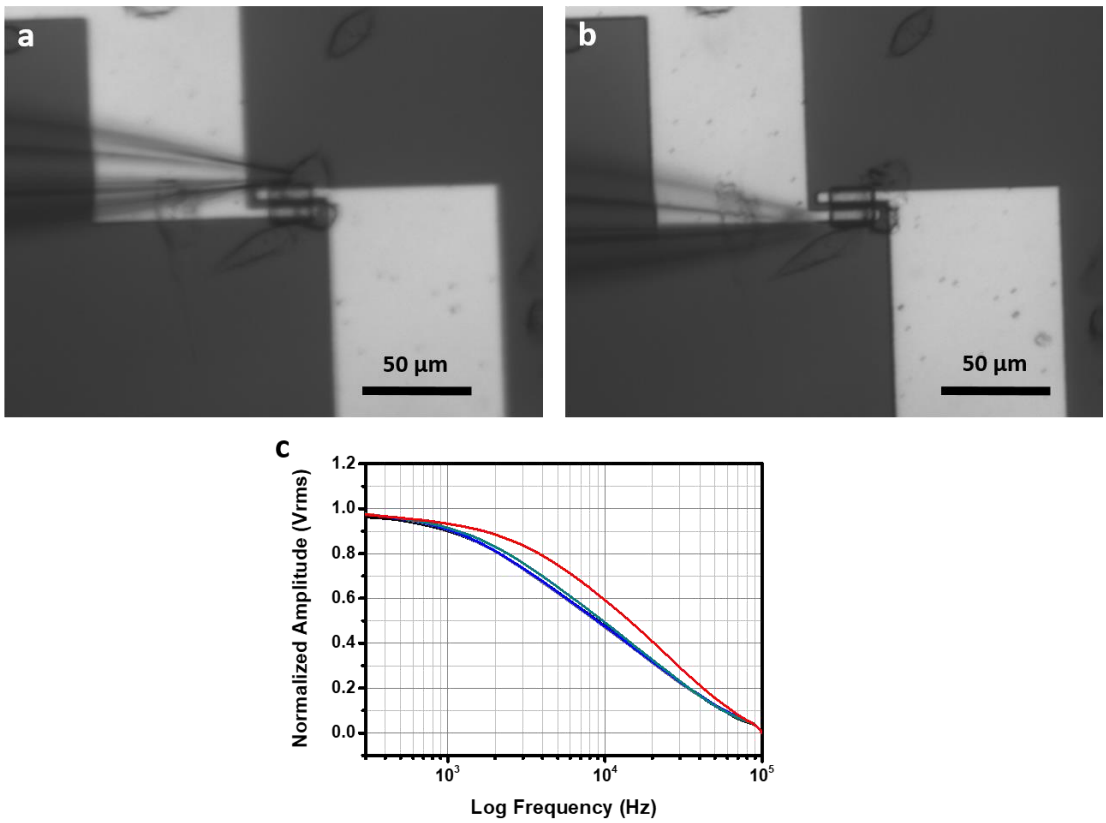

Figure 55: Microscopic images of two adherent cells on an OECT a) patch pipette immersed in the cell culture medium before the cell removal, b) the cells moved from the sensing area but not detached from the surface, c) corresponding spectra measured by a lock-in amplifier for different stages of the measurement with the microscope light switched on and off, with the patch pipette immersed in the medium and outside of the medium. The graphs overlay perfectly with the blue curves showing the measurements with an adherent cell and the red curve shows the measurements after the cell was removed. The light and the presence of a pipette in the liquid do not influence the measurements.

In Figure 55a two cells can be seen on one sensing area, both cells do not cover the OECTs sensing area completely, in Figure 55b the cells were mechanically moved to the side, with the lower cell still touching a small part of the sensing area. For the performed measurements, not only the process of cell attachment and cell detachment was measured as can be seen in Figure 55c. The OECT was measured twice under the microscope with the light and the patch-clamp manipulators switched off. Then the OECT was measured with the light switched on once and afterward again with the patch pipette immersed in the culture medium while the setup for the patch-clamp manipulators was running. The last measurements were performed after the moving of the cells with the light and the running patch-clamp setup, after the removal of the patch pipette from the liquid and after the switching off of the light and the patch clamp setup. The data shows no influence of the light, the measurement setup, or the presence of the patch pipette on the measurements, which creates the possibility to film or observe the cells during the measurements.

Since not a single adherent cell was at the OECTs sensing area, the direct influence of the cell adhesion could not be observed in a defined way. In addition, the cells were not picked up by the patch pipette but were pushed away. An ideal experiment is shown in Figure 56, where a single cell was attached to the sensing area (Figure 56a), which was removed by the patch pipette (Figure 56b). The spectra showed a big change for the two stages of cell attachment (Figure 56c). It can be assumed that the perfect coverage of the sensing area leads to a maximum change in frequency response. With the adherent cell the cutoff frequency was measured at 1869 Hz and changed to 11,622 Hz after the cell was removed from the sensing area. When compared to previously shown data with partially covered sensing areas, the effect shown in Figure 56c is bigger.

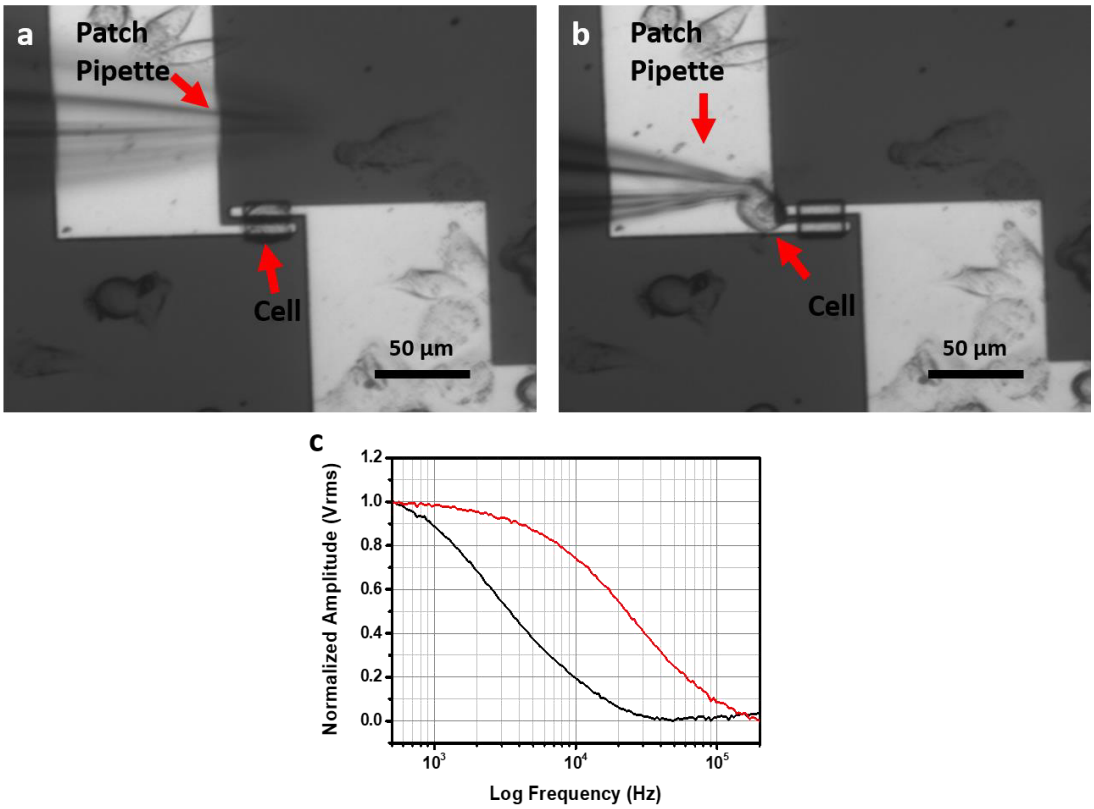

Figure 56: Microscopic images of an adherent single cell on an OECT a) before removal with the patch pipette already immersed in the cell culture medium, b) the cell lifted from the sensing area still sticking to the patch pipette, c) corresponding spectrum measured by a lock-in amplifier (black: Adherent cell, red: Removed cell).

When comparing different gathered results, it could be seen that the coverage of the sensing area influences the measured spectra. A good coverage of the sensing area is desirable in order to detect the maximum effect, even though the partial attachment of a cell to the sensing area can still be measured clearly. Unfortunately, the coverage of the sensing areas in the experiments is always random so that only a huge amount

of experiments would be able to gather data from all possible adhesion stages. The coverage of the whole sensing area with a single cell is difficult to achieve with the HEK cells, due to their size. Therefore, an experimental configuration was planned to visualize this effect by using a PDMS droplet which was pressed onto the device surface covering a single sensing area while being gradually released from the surface. This experiment should provide insight into the measurement principle and the effects caused by the attachment/detachment of the cells. The experiment was performed with a patch-clamp setup and its micromanipulators. A PDMS droplet was attached to a thin wire which allowed the droplet to be pressed onto the device surface. The force used to press the PDMS drop could not be measured in this configuration, but the parallel electronic measurements were used to visualize the cell release as it might happen on the device (Figure 57a and Figure 57b).

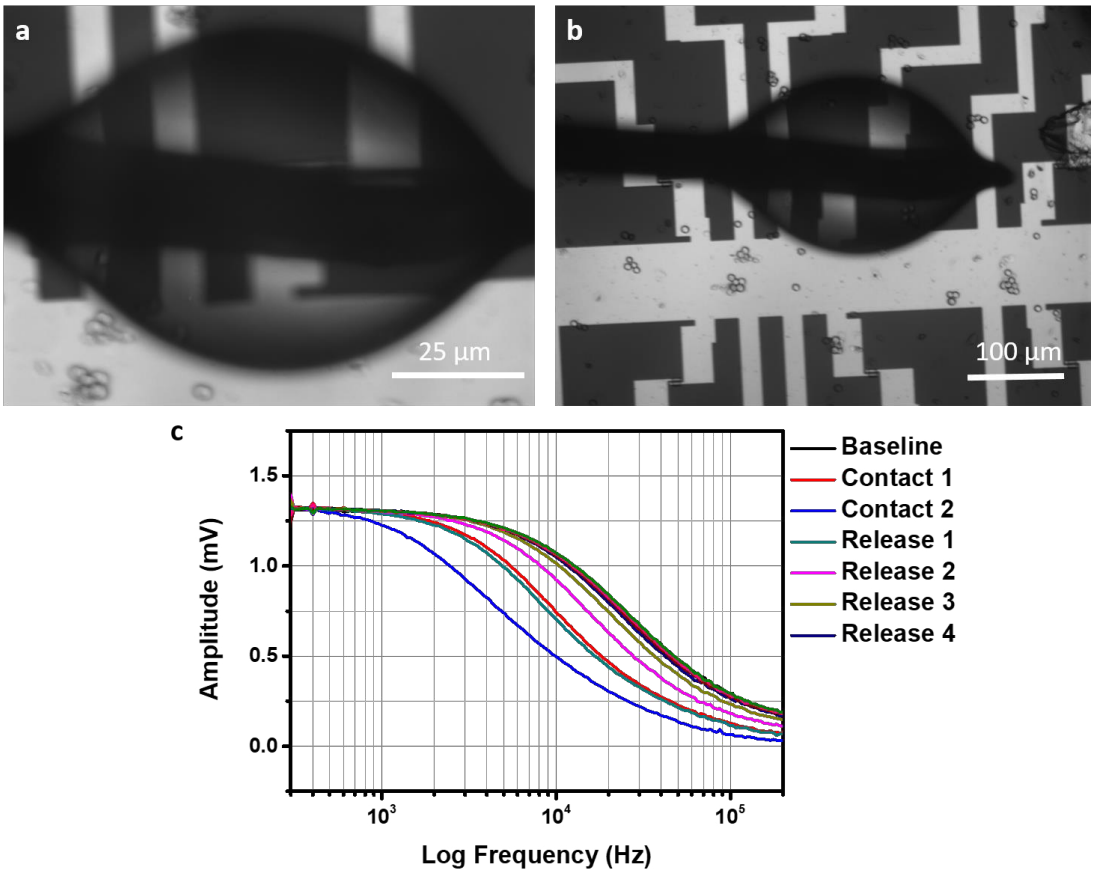

Figure 57: Microscopic images of a PDMS droplet on a piece of wire a) and b) connected to a micromanipulator with c) the corresponding spectra. Baseline indicating the spectrum before the droplet was pressed onto the surface with two following steps where the droplet was lowered onto the device surface and the gradual release of the droplet.

The droplet used in this experiment was around 200 µm in diameter due to the simple setup. It was possible to cover only a single OECT sensing area with the droplet. As

can be seen in the recorded spectra of Figure 57c the curves follow the previously shown measurements with actual cells, showing how the cutoff frequency is shifting towards higher frequencies when a cell is removed chemically or mechanically from the surface. The initial value of the baseline is reached again after the droplet is completely removed from the OECT surface and remains even when the droplet is taken out of the liquid. A control was performed where no changes appeared due to the presence of the droplet, as long as the droplet was not in contact with the respective sensing area. The overall change in the spectrum is bigger than it was measured with an actual cell. This effect can be attributed to the area of coverage being bigger for the PDMS droplet in comparison to a cell. The PDMS droplet can, in theory, seal the sensing area completely from the surrounding medium, creating the measured effect. The experiment should be seen as an approximate representation of the cell measurements, not only following the simple cell removal but also the gradual release of a cell from the surface as it was also experimentally observed. This data also suggests the device behavior for experiments with other cell lines. Especially cells with tight gap junctions can be expected to deliver similar results as long as the sensing area is completely covered by cells, as it would happen with MDCK cells.

3.6.3 MDCK Cell Junction Measurements

Since the sensing area of the OECTs for single cell experiments showed g_m values exceeding ISFETs of similar proportions by a factor of ten, the devices were tested for a whole different purpose with the use of MDCK cells. Unlike HEK cells, MDCK cells form gap junctions in between individual cells. The results should, therefore, resemble the measurements performed in Figure 57 with the PDMS droplet that was pressed on the sensing area. The MDCK cell type determines the resistance through this junction. However, the addition of EGTA to the cells enables the opening of these gap junctions, which is measurable as a decrease in the resistance of the gap junctions. This process is reversible and does not harm the cells. By utilizing this cell line, it is possible to show the capability of the OECTs for detecting the opening and closing of the gap junctions in cells, while remaining a small sensing area.

The MDCK cells were grown on the OECTs with a high density (50,000 cells in 100 µl per chip) and measured after three days *in vitro* when the sensing areas were covered. Before the actual measurement, the medium was changed to fresh, pre-warmed medium, and the cells were kept in an incubator for 30 minutes for acclimatization.

This point marked the initial spectrum of the measurements. Afterward, EGTA was added to the medium to achieve a concentration of 100 mM EGTA. The medium was once again replaced with fresh, pre-warmed medium, and the OECTs were kept in an incubator for 1 hour in order for the cells to recover their gap junction resistance. In a final step, the cells were removed from the surface by trypsinization. Afterward, the measured data was plotted. Figure 58 shows one performed measurement. The shift in the spectrum from the adherent cells (black) to the measurement after the EGTA opened the gap junctions (red) can be seen. The cutoff frequency is shifted to higher frequencies. This effect was reversible after the medium was changed to the normal culture medium for 1 hour (blue) and a maximum shift was achieved after the chemical removal of the cells from the surface (pink).

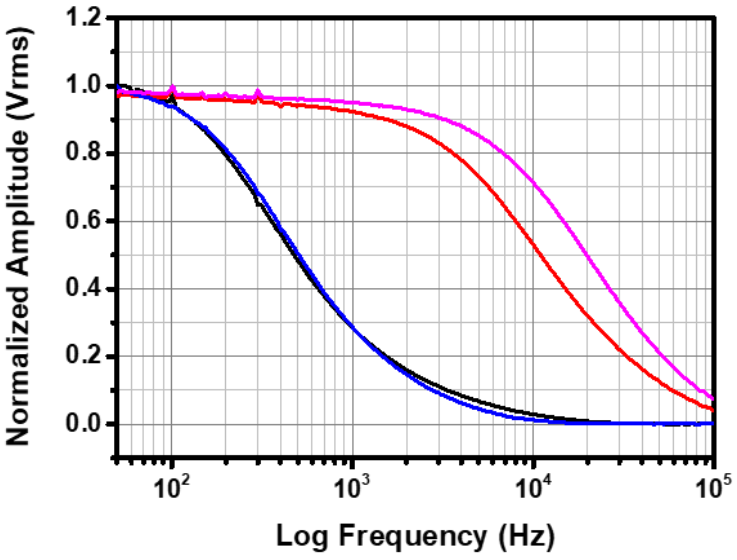

Figure 58: Recorded spectra for the MDCK cells on the 20×20 µm² OECTs measured with a lock-in amplifier (black: Adherent cell in medium, red: Adherent cell after 15 minutes in EGTA medium, blue: Adherent cell after 1 hour in normal medium, pink: After the cell is removed by trypsinization).

With the cells attached a cutoff frequency of 273 Hz was measured, after the addition of EGTA this value changed to 5480 Hz. As can be seen in Figure 58, the initial cutoff frequency was restored after the medium was changed. Once the cell was removed a cutoff frequency of 10,188 Hz was measured.

Control measurements were performed for each experiment in a configuration that had cells grown on the devices, but instead of the diluted EGTA, only DI water with the same volume was added to the cultures while the rest of the procedures remained the same (Figure 59).

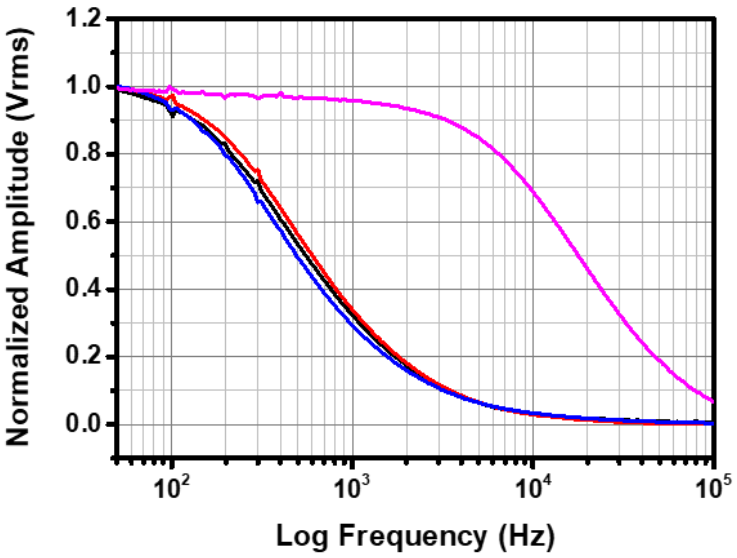

Figure 59: Spectrum of a MDCK control measurement where adherent cells are present on the OECT surface, but no EGTA is added. All the other experimental procedures were performed the same. When the medium was changed for the other devices the medium was changed with this device as well to keep the treatment conditions constant (black: Measurement in normal medium, red: Measurement after 15 minutes in normal medium with DI water instead of EGTA, blue: Measurement after 1 hour in normal medium, pink: After cell is removed by trypsinization).

Figure 59 shows, that the parameters of the experiment have no effect on the measured spectra. The cutoff frequencies for the spectra were measured at 292 Hz and the removal of the cells changed the cutoff frequency to 9273 Hz. DI water as part of the EGTA solution did not show an effect on the cells.

The performed measurements showed a variation in the frequency spectra with the corresponding cutoff frequencies for different devices. It cannot be identified where this variation is coming from with the performed measurements.

In addition, it had to be shown that the measurements were not showing a deterioration of the polymer itself, so controls were performed without cells, still following all the experimental steps that were performed on the devices with adherent cells (Figure 60). The incubation times and media changes were kept exactly the same. EGTA was added the same way as it was performed with the other devices. Should the handling or device treatment have any effects on the measured results it would be shown with this measurement.

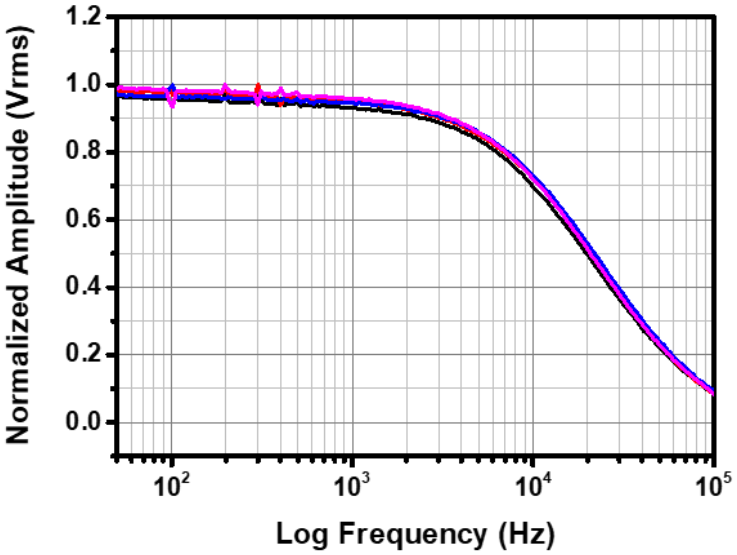

Figure 60: Spectrum of a MDCK control measurement where no cells are located on the OECT surface. All the other experimental procedures were performed the same (black: Measurement in normal medium, red: Measurement after 15 minutes in medium with EGTA, blue: Measurement after 1 hour in normal medium, pink: Measurement after trypsinization in normal medium).

Figure 60 shows, that there is no change in the frequency response when EGTA is added to the device. The cutoff frequency was at a stable 10,350 Hz for all measurements. Both control experiments clarify, that the changes in the measured frequency spectra can be contributed to the effects of EGTA on the cells. The other parameters of the experiments did not cause any shifts in the spectra.

3.6.4 Conclusion

Cell impedance experiments were first performed with HEK cells which do not form gap junctions. Confluent cell layers were tested with the OECTs with adherent cells and after cell removal. The measurements showed the differences in the spectra caused by the cell adhesion. When cells are located at the OECTs sensing areas the impedance spectrum is showing a shift of the cutoff frequency to lower frequency values, therefore, the removal of the cells increases the cutoff frequency. The necessary control measurements were performed to exclude the effects of the measurement medium or by the added chemicals on the OECT function. Especially for the measurements with confluent cell layers, an inhomogeneity between the 16 sensing areas on one device can be seen which can be attributed to the number of adherent cells as well as the coverage of the sensing area.

By reducing the sensing area size and lowering the number of cells, single cell experiments could be performed where the effect of the removal of one single cell could be investigated. These experiments confirmed the importance of the cell placement on the gate for the measurements, where a maximum difference between the spectra for a fully covered sensing area was detected. A schematic representation of the measurement effect is shown in Figure 61. The blockage of the ion movement, when obstructed with a cell is the effect that can be measured as soon as the polymer layer is covered. This also explains why the coverage of the PEDOT:PSS is one important factor since the ions are hindered in their path towards the polymer. Due to the high sensitivity of the tested devices, partial coverage of the sensing areas also resulted in clear effects.

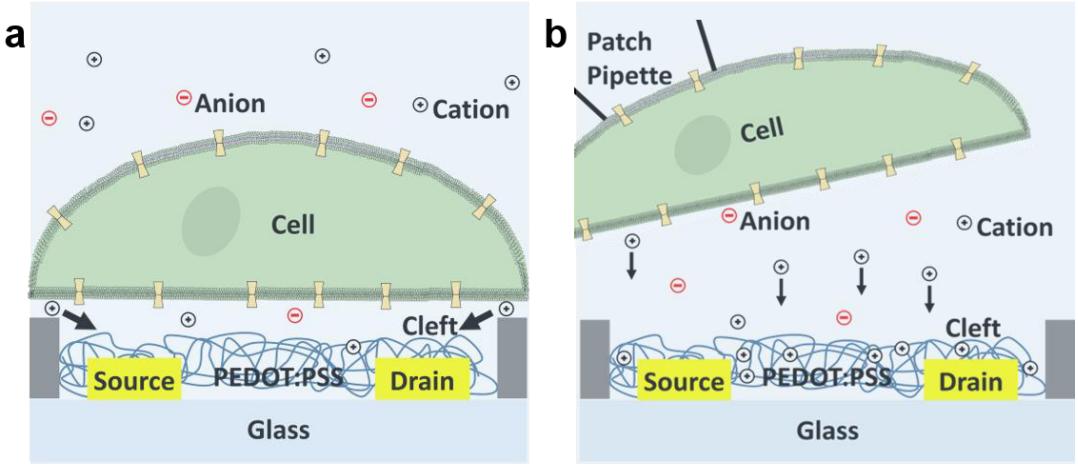

Figure 61: Schematic illustration of the principle of the ion movement for a measurement setup, where a) a single cell is obstructing the ion movement towards the polymer and b) the cell is removed, opening the path for the ions. The increased resistance for the ion movement is measured as a shift to lower frequencies when a cell is adherent.

In contrast to the HEK cells, the MDCK cells form gap junctions between the cells, which enables a tight seal of the sensing areas on an OECT and allows for big spectra changes due to cell adhesion. The chemical opening of the gap junctions shows exactly this phenomenon where the spectra are shifted to higher cutoff frequencies due to the opening of an electrical pathway between the cells without changing their adhesion behavior. This is demonstrated schematically in Figure 62.

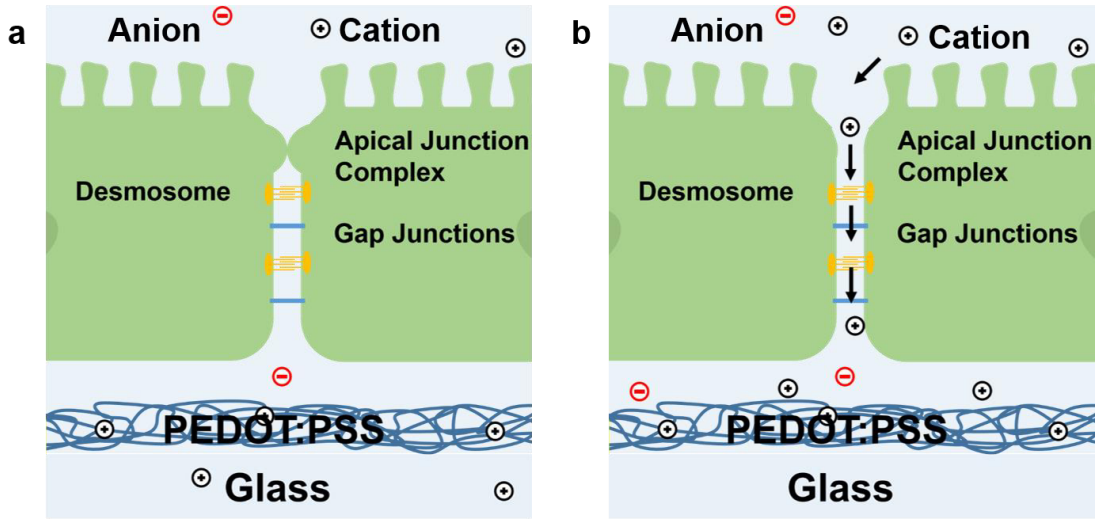

Figure 62: Schematic illustration of the principle of the ion movement for a measurement setup, where a) two MDCK cells are obstructing the ion movement towards the polymer and b) the gap junctions are chemically opened. The increased resistance for the ion movement is measured as a shift to lower frequencies.

Even though the mechanism, based on the obstruction of the ions is the same, the difference in adhesion of the cells can be seen with the electrical measurements. The MDCK cells create a tighter seal around the sensing areas when compared to the HEK cells. Therefore, a lower cutoff frequency is measured for the MDCK cells. The chemical opening of the gap junctions creates an effect that is similar to the removal of the cells but this effect is reversible. After the EGTA is removed from the cell medium the initial frequency spectrum for adherent cells is measured.

3.7 Mathematical Modeling of the Devices

The data presented in the previous chapters were used to create a mathematical representation of the measurement setup in combination with the OECTs. When using a mathematical model of the system, all relevant components of the system can be represented with a value. In this case, the integration of a PEDOT:PSS based device with an adherent cell was achieved. The focus on single cell measurements was crucial in order to generate a model, since only one cell had to be taken into account. However, an additional component was added to represent cellular junctions as they appear in a variety of cells. A mathematical model does not have to provide an exact representation of the observed system but should be viewed as a tool to understand simple connections and processes as they happen during electrical measurements. If done properly, the trends of the measured data should be explainable with the presented model. However, the complexity of a biological system when interfacing an electrical system poses a challenge for accurate modeling.

3.7.1 Mathematical Representation of the Measurement Setup

For the mathematical representation of the OECTs, an established model (SUSLOPAROVA, 2016) was adjusted to study the shift of the cut-off frequency due to cell adhesion. The model combines the device related parameters with the transimpedance-circuit parameters and the cell related parameters. A schematic of the electrical equivalent circuit of the measurement setup is shown in Figure 63. The cell part is described by the junction resistance (R_J), the seal resistance (R_{Seal}) and the membrane capacitance (C_M). The PEDOT:PSS is described by the Warburg element (Z_W), the bulk capacitance (C_b), the transconductance (g_m) and the output resistance (R_{DS}). Parasitic parameters are considered as the capacitance and the resistance of the source contact (C_{Source}, R_{Source}) and the capacitance and the resistance of the drain contact (C_{Drain}, R_{Drain}). The reference electrode and the electrolyte solution are combined to a resistance (R_{el}). A transimpedance amplifier circuit is represented by an operational amplifier and a feedback resistance ($R_{feedback}$).

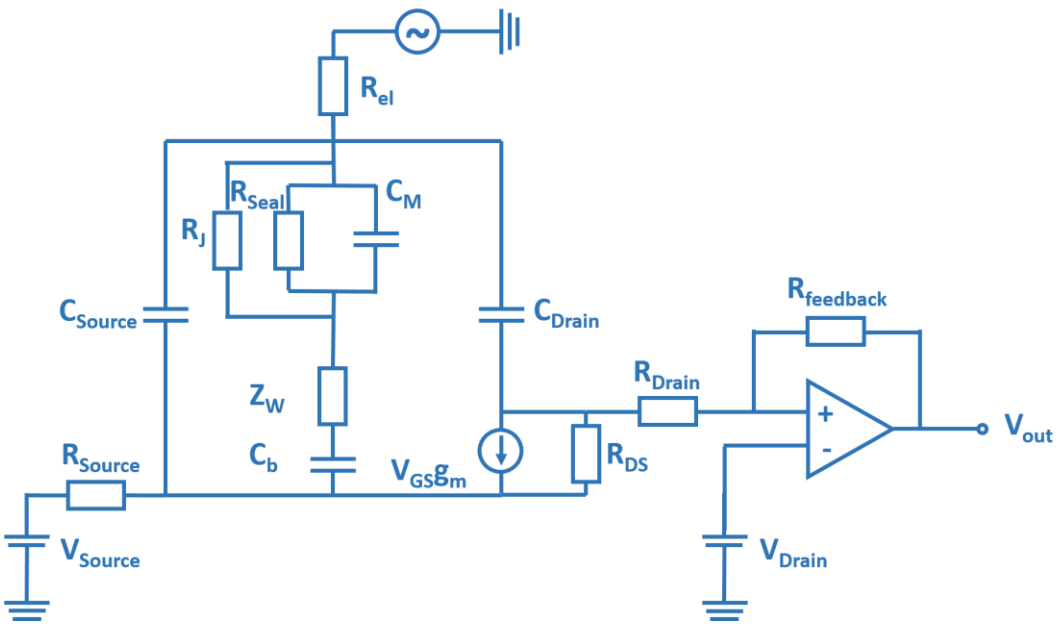

Figure 63: Electrical equivalent circuit for the OECT measurement setup.

By making the circuit, as shown in Figure 63, an analytical expression could be derived by using Kirchhoff's law and the rules for the combination of impedances. The transfer function H(jw) is given by Equation (3.1):

$$H(jw) = \frac{V_{out}(jw)}{V_{in}(jw)} \tag{3.1}$$

In this equation, w represents the angular frequency and j the imaginary unit. A sinusoidal voltage $V_{in}(jw)$ is applied to the reference electrode with the output voltage $V_{out}(jw)$ being measured after the transimpedance amplifier. $V_{out}(jw)$ can be described by Equation (3.2) using the $R_{feedback}$ and the drain-source current (I_{DS}):

$$V_{out}(jw) = -R_{feedback}\, I_{DS}(jw) \tag{3.2}$$

I_{DS} can be described as Equation (3.3) (SUSLOPAROVA, 2016):

$$I_{DS}(jw) = g_m V_{GS} - jwC_d V_1(jw) \tag{3.3}$$

With the corresponding g_m, the gate-source voltage (V_{GS}), C_d as the contact line capacitance of the drain and V_1 as the voltage across C_d.

In the following steps, the impedances (Z) of the individual parts of the electrical equivalent circuit were determined and combined according to the mathematical rules for impedances in line and in parallel. The impedance of a cell is given by Equation (3.4).

$$Z_1 = R_J + \left(\frac{R_{Seal}}{1 + R_{Seal}C_M}\right) \tag{3.4}$$

In the case of single cell experiments, R_j has a value of zero and is therefore not considered for resolving the equation. The impedance of the capacitor separating the electrodes from the liquid is shown in Equation (3.5).

$$Z_2 = \frac{1}{jwC_b} \tag{3.5}$$

PEDOT:PSS is represented by a diffusion resistance (R_D) and diffusional time constant (t_D) in Equation (3.6) (BOBACKA et al., 2000; DANIELSSON et al., 2004).

$$Z_3 = \frac{R_D \coth\left(jwt_D\right)^{\frac{1}{2}}}{\left(jwt_D\right)^{\frac{1}{2}}} \tag{3.6}$$

The impedances are added to Equation (3.7).

$$Z_4 = Z_2 + Z_3 \tag{3.7}$$

In order to find the value of V_{GS} a first voltage divider is applied based on Figure 64 resulting in Equation (3.8):

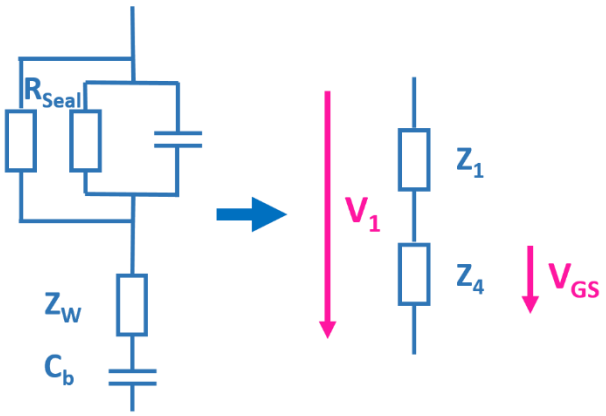

Figure 64: First voltage divider based on the impedances by the cell and the polymer.

$$\frac{V_1(jw)}{V_{GS}(jw)} = \frac{Z_1 + Z_4}{Z_4} \tag{3.8}$$

Where V_{GS} can then be represented by Equation (3.9):

$$V_{GS}(jw) = V_1(jw)\ \frac{Z_4}{Z_1 + Z_4} \tag{3.9}$$

Which combined with Equation (3.3) results in Equation (3.10):

$$I_{DS}(jw) = g_m V_1(jw)\ \frac{Z_4}{Z_1 + Z_4} - jwC_d V_1(jw) \tag{3.10}$$

This term is then inserted in (3.2) and creates Equation (3.11):

$$V_{out}(jw) = -R_{feedback} g_m V_1(jw)\ \frac{Z_4}{Z_1 + Z_4} - jwC_d V_1(jw) \tag{3.11}$$

Together with (3.1) H(jw) can be written as Equation (3.12):

$$H(jw) = R_{feedback} g_m \frac{V_1(jw)}{V_{in}(jw)} \left(\frac{Z_4}{Z_1 + Z_4} - jwC_d V_1(jw) \right) \tag{3.12}$$

In order to determine V_1(jw) another voltage divider has to be utilized (Figure 65). First, the impedances are combined with the sum of C_d as shown in Equation (3.13)

$$Z_5 = \frac{1}{jw2C_d + \frac{1}{Z_4 + Z_1}} \tag{3.13}$$

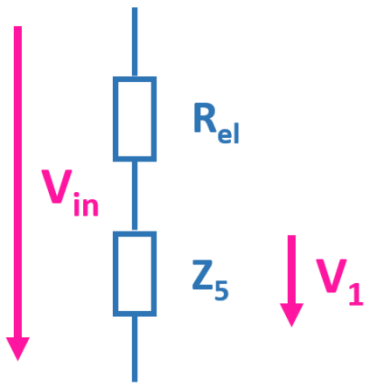

Figure 65: Second voltage divider utilizing the sum of all the impedances following R_{el}.

The sum of the individual impedances is then used in the voltage divider in Equation (3.14) with R_{el}:

$$\frac{V_{in}(jw)}{V_1(jw)} = \frac{R_{el} + Z_5}{Z_5} \tag{3.14}$$

Resulting in Equation (3.15):

$$\frac{V_1(jw)}{V_{in}(jw)} = \frac{Z_5}{R_{el} + Z_5} \tag{3.15}$$

combined with Equation (3.12), Equation (3.16) is derived:

$$H(jw) = R_{feedback} g_m \left(\frac{Z_5}{R_{el} + Z_5} \left(\frac{Z_4}{Z_1 + Z_4} - \frac{jwC_d}{g_m} \right) \right) \tag{3.16}$$

Considering the low pass characteristics of the measurement setup, the final equation containing the individual impedances can be written as Equation (3.17):

$$y = R_{feedback} g_m \left(\frac{Z_5}{R_{el} + Z_5} \left(\frac{Z_4}{Z_1 + Z_4} - \frac{jwC_d}{g_m} \right) \right) \frac{1}{\sqrt{\left(1 + \frac{f}{fg}\right)^2}} \tag{3.17}$$

Here the cutoff frequency of the operational amplifier (f_g) and the frequency (f) are considered. By separating the individual parts of the circuit in impedances the equation can be tested with different parameters. The presented equation was able to deliver accurate fitting results for single-cell experiments, where the cell part has only to account for a single cell and its membrane. The addition of a junction resistance for MDCK cells does not account for the adhesion of several cells that do not form a junction, as would be the case for the OECTs with big sensing areas with adherent HEK cells. The proposed equation was developed mainly to focus on single cell experiments rather than on a system with many cells.

In addition, another mathematical way can be used to determine the distance between the cell and the sensing area as an approximation. R_{Seal} can be calculated by Equation (3.18) (PABST et al., 2007), which was derived to calculate R_{Seal} for cell-transistor coupling.

$$R_{Seal} = \frac{k_B T}{4\pi e_0^2 n_{tot}^B D_{K^+} h}\left[1 + 4\frac{L_D^2}{r^2}\left(\frac{1}{I_0(r/L_D)} - 1\right)\right] \quad (3.18)$$

Included in the equation are the Boltzmann constant (k_B), the temperature (T), the elementary charge (e_0), the ion density of the surrounding bath solution (n_{tot}^B) and the diffusion coefficient of potassium (D_{K+}). The two main parameters influencing R_{Seal} are then the cleft height (h) and the ion density. A correction term in the right part of the equation, including I_0 as the modified Bessel function, is important if the cell radius (r) has a similar size as the Debye length (L_D). When measuring in a physiological medium, L_D will be in the nanoscale, with a cell size in the micro-scale. Therefore, the expression in brackets will be equal to one, and the equation condenses to Equation (3.19).

$$R_{Seal} = \frac{k_B T}{4\pi e_0^2 n_{tot}^B D_{K^+} h} = \frac{k_B T}{e_0^2 n_{tot}^B}\,\frac{1}{4\pi D_{K^+} h} \quad (3.19)$$

With the L_D in the solution given by Equation (3.20):

$$L_D = \sqrt{\frac{\varepsilon_0 \varepsilon_r k_B T}{e_0^2 n_{tot}^B}} \quad (3.20)$$

With the permittivity of the vacuum (ε_0) and the dielectric constant (ε_r). When Equation (3.20) is included in Equation (3.19) a representation for R_{Seal} in the physiological buffer can be written as Equation (3.21):

$$R_{Seal} = \frac{L_D^2}{4\pi \varepsilon_0 \varepsilon_r D_{K^+} h} \quad (3.21)$$

In order to determine the Debye length of the measurement solution, the n_{tot}^B has to be calculated using Equation (3.22):

$$n_{tot}^B = 2 N_A I \quad (3.22)$$

Avogadro's number (N_A) and the ionic strength (I), which can be calculated by Equation (3.23):

$$I = \frac{1}{2}\sum c_i z_i^2 \quad (3.23)$$

This equation contains the concentration (c) and the valency of the ions (z). With the calculation L_D for the cell medium, the calculation of h for different R_{Seal} values can be made. Due to the fitting with Equation (3.17), R_{Seal} can be controlled, and the approximate distance between cell and sensing area can be calculated.

3.7.2 Modeling of the Cell Coupling

In this paragraph, the actual fitting procedure will be demonstrated using measured data. For the experiments, the OECTs can have three states: OECTs with cell-free sensing areas, OECTs with cell-covered sensing area, and OECTs with cell-covered sensing area with open gap junctions. First, to enable the fitting some of the fixed parameters concerning the measurement setup and the devices had to be calculated. For the parasitic capacitances of the source and drain contact lines ($C_{Source/Drain}$), a plate capacitor can be used, as shown in Equation (3.24):

$$C_{source/drain} = \frac{\varepsilon_0 \varepsilon_{ox} A_{Source/Drain}}{d} \tag{3.24}$$

With ε_0 = 8.8542×10^{-12} As/Vm, and the relative permittivity of the silicon dioxide passivation (ε_{0x} = 3.9), the area of the source or drain contact lines ($A_{Source/Drain}$) and the thickness d of the passivation layer.

The g_m for the measured device was determined before the measurements in order to set the working point of the devices in the lock-in amplifier.

R_{el} was set to 1 kΩ as an approximate value. However, the impact of this factor was small and could be used like this for the fitting. $R_{feedback}$ was set in the lock-in amplifier software at a value of 1 kΩ, which resulted in a f_g of 10 kHz.

In order to test the model for cell coupling, several individual tasks were performed. First, the model was applied to cell-free OECTs, which resulted in the impedance of the cell part to be set to zero. Since most of the device related parameters could be calculated and measured easily, some of the polymer related parameters had to be established before the fitting of the cell measurements could be performed. R_j was only fitted for cells that develop gap junctions and otherwise set to zero. The model was applied to the TTF box measurements as well as to the lock-in data.
Figure 66 shows the OECT sensing area, which was measured with an adherent HEK cell with both measurement setups. The established equation was used to fit the data.

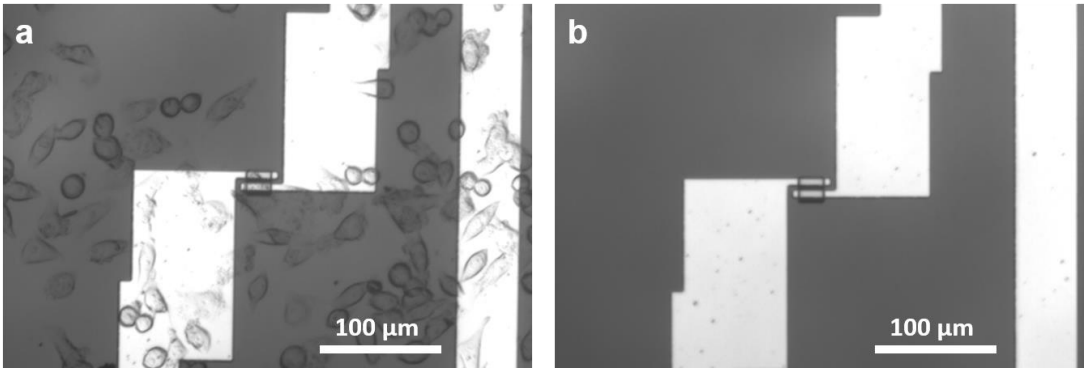

Figure 66: Microscopic image of a 20×20 µm² OECT a) with adherent HEK cells on one single sensing area, b) after the chemical removal of the cells with trypsin.

Figure 67 shows the measured data for the TTF box with a) sensing area without a cell, after cell removal, b) sensing area with adherent cell and c) combined data of the measurements. The graphs show the data as it was measured with the system and their respective fits by applying the mathematical model. Overall a nice fit was calculated when applying the derived equation.

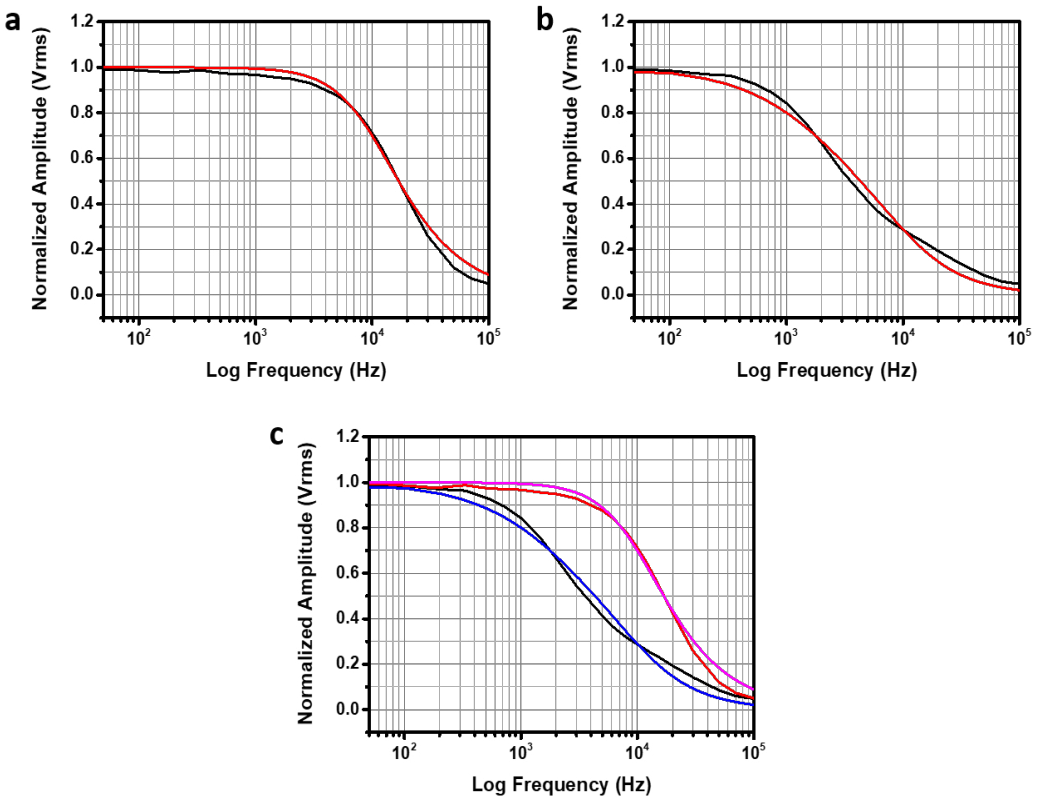

Figure 67: Plotted data of a 20×20 µm² OECT consisting of the measured data of the TTF box and their corresponding fits for HEK cells, a) sensing area without cell, after cell removal (black: Measured data, red: Fitted data), b) sensing area with adherent cell (black: Measured data, red: Fitted data) and c) combined data in one single plot (black: Measured data with adherent cell, red: Measured data with removed cell, blue: Fitted data with adherent cell, pink: Fitted data with removed cell).

The values used to calculate the fitting curve for the data are summarized in Table 5. Only the cell-related parameters were fitted. The values calculated by the software for R_{Seal} and C_M were 4.13×10^7 Ω and 3.29×10^{-13} F, respectively.

Table 5: Values for the fitted curve in Figure 67

Parameter	Value without cell	Value with cell
t_D	0.5 s	0.5 s
R_d	1000 Ω	1000 Ω
R_{el}	1000 Ω	1000 Ω
R_{Seal}	**0 Ω**	**4.13×10^7 Ω**
C_M	**0 F**	**3.29×10^{-13} F**
C_d	6.17×10^{-11} F	6.17×10^{-11} F
g_m	1 mS	1 mS
$R_{feedback}$	1000 Ω	1000 Ω
j	6.33	6.33
C_b	1×10^{-12} F	1×10^{-12} F
fg	10,000 Hz	10,000 Hz
R_j	0 Ω	0 Ω

For the lock-in amplifier, a change in cutoff frequency in comparison to the TTF box was observed. This is based on the used hardware since the device itself did not change. Therefore, f_g had to be adjusted. Figure 68 shows the data with a) sensing area without a cell, after cell removal, b) sensing area with adherent cell and c) combined data of the measurements. In accordance with the experiment, the device-related parameters were not changed, and only f_g was adjusted for the setup-related parameters so that the model should deliver functional fits with the alteration of the cell-related parameters.

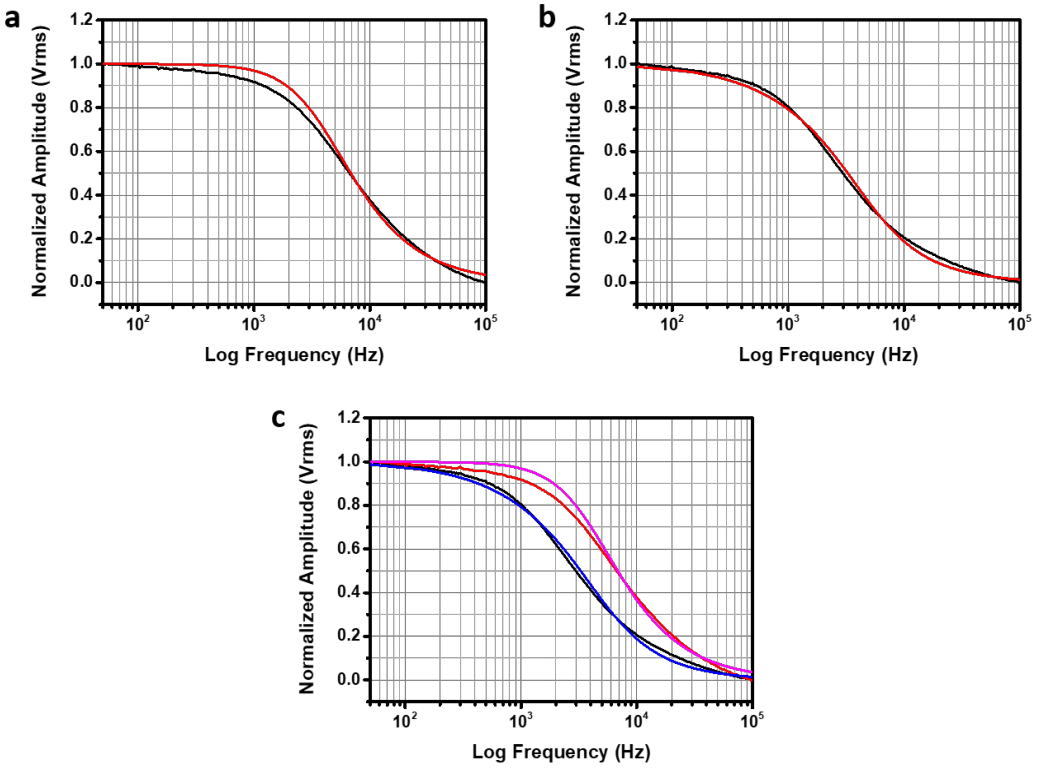

Figure 68: Plotted data of a 20×20 µm² OECT consisting of the measured data of the lock-in amplifier and their corresponding fits for HEK cells, a) sensing area without cell, after cell removal (black: Measured data, red: Fitted data), b) sensing area with adherent cell (black: Measured data, red: Fitted data) and c) combined data in one single plot (black: Measured data with adherent cell, red: Measured data with removed cell, blue: Fitted data with adherent cell, pink: Fitted data with removed cell).

The calculated values are summarized in Table 6. Similar values for the measurement with the TTF box were derived with an R_{Seal} at 4.13×10^{7} Ω and a C_M of 6.85×10^{-13} F which should be the case since the exact same conditions were measured with the different setups.

Table 6: Fitted values for the cell related parameters relating to Figure 68

Parameter	Value without cell	Value with cell
t_D	0.5 s	0.5 s
R_d	1000 Ω	1000 Ω
R_{el}	1000 Ω	1000 Ω
R_{Seal}	**0 Ω**	**4.13×10^{7} Ω**
C_M	**0 F**	**6.85×10^{-13} F**
C_d	6.17×10^{-11} F	6.17×10^{-11} F
g_m	1 mS	1 mS
$R_{feedback}$	1000 Ω	1000 Ω
j	6.33	6.33
C_b	1×10^{-12} F	1×10^{-12} F
fg	4000 Hz	4000 Hz
R_j	0 Ω	0 Ω

Since the parameters for the measurement setup and for the devices do not change while performing different experiments, the derived equation could be used for the fitting throughout the performed experiments.

In order to apply this model for the MDCK cell measurements, R_J had to be fitted as well. The values gathered for empty sensing areas were set to be the same as for the previously performed experiments, which allowed the cell related parameters to be set to zero. For the state of adherent cells in this experimental configuration, single cell adhesion cannot be guaranteed. The ideal case would be the adhesion of two cells with the gap junction crossing the sensing area of the OECT. However, this state cannot be confirmed without staining methods. For the fitting procedures with adherent cells, the equation was used, and the cell related parameters were fitted. The adhesion of the MDCK cell might be changed by the addition of EGTA, which is supposed to open the gap junctions, but the overall adhesion and placement of the cells will not be affected.

This meant that the opening of the gap junctions should show a major change in R_J, while the change in R_{Seal} and C_M should be small.

Figure 69 shows an exemplary result of the performed measurements with MDCK cell on a 20×20 μm^2 device where the gap junction resistance was altered with EGTA.

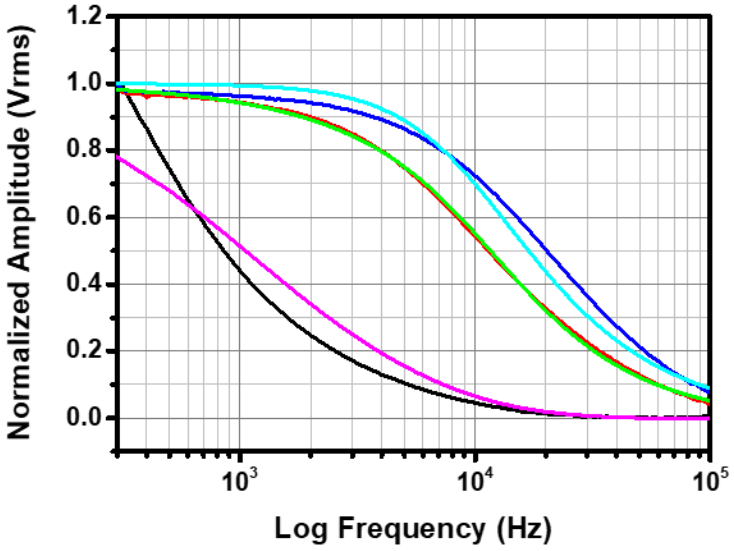

Figure 69: Measurement of MDCK cells on an OECT with the fitted curves (black: Measured data with cells, red: Measured data after EGTA was applied, blue: Measured data after cell removal, pink: Fitted data with adherent cell, green: Fitted data after EGTA was applied, cyan: Fitted data after cell removal).

The black, red, and blue curves of the graph show the measured values with the pink, green, and purple curves representing the fitted values. Overall a clear tendency of the fitted curves could be seen. As already shown with the single cell experiments, the occurring shift to cell adhesion could be calculated as well, even though R_J was included in the equation. R_J should have a higher value when compared to R_{Seal}, which was the case for the fitted values shown in Table 7. R_J was fitted with a value of 1.44×10^8 Ω and R_{Seal} was at 3.09×10^6 Ω.

Table 7: Fitted values for the data shown in Figure 69 for adherent MDCK cells

Parameter	Value
R_{Seal}	3.09106×10^6 Ω
C_M	1×10^{-13} F
R_J	1.44507×10^8 Ω

A bigger R_J would result in a preferred current pathway through R_{Seal}.
But with the opening of the gap junctions, this should be inverted, as can be seen in the measured spectra, where the curve is closer to the measured spectrum for the empty sensing area. This suggests a decrease in the resistive path in a similar fashion that would be caused by the detachment of the cell.
When fitted with the equation, the values shown in Table 8 are generated.

Table 8: Fitted values for the data shown in Figure 69 for adherent MDCK cells with EGTA to open the gap junctions

Parameter	Value
R_{Seal}	9.33769×10^{6} Ω
C_M	2.54066×10^{-12} F
R_J	483.640×10^{3} Ω

A significant drop in R_J was calculated, while R_{Seal} was almost not affected. For this measurement, R_J was calculated with 483 MΩ, and R_{Seal} was at 9.33×10^{6} Ω. The huge drop in R_J can explain the measured spectrum with the shift to higher frequencies.
The showed measurements for the MDCK cells show a clear limit of the derived equation when applied for several cells. A simple addition of a junction resistance cannot represent all possible cases that might occur during an experiment. In this case, it would be possible that several gap junctions are present on the sensing area or that no gap junction is present. This can easily explain the differences between the fitted values and the measured data.

3.7.3 Calculated Distance Between Cell and OECT

The fitted values can be used to calculate the distance between the cells and the OECTs according to the equations introduced in Chapter 3.7.1. The distance between the cell and the polymer layer directly correlates to R_{Seal} with an increase in h, causing a decrease in R_{Seal}. This might be used to confirm the values calculated by the fitting procedure for R_{Seal}. Since the two equations can be used to calculate the same value, the distance has to be in a logical order. Following Equation (3.18), first Equation (3.22) and Equation (3.23) have to be solved for the case of cell culture medium. The ionic strength of the medium is calculated by the ions which are present. The contents of the used medium is shown in Table 9.

Table 9: Components of inorganic salts in the HEK medium in mg/l

Component	mg/l
Calcium chloride x $2H_2O$	264.92
Magnesium sulfate	97.67
Potassium chloride	400.00
Sodium chloride	6,300.00
Sodium dihydrogen phosphate x H_2O	140.00

Following Equation (3.23) the ionic strength of the culture medium is calculated by converting the values in Table 9 into the concentration of the ions in the culture medium with a volume of 500 µl. This leads to a value for the ionic strength of I = 0.00152 mol/l. In order to determine the ion density for this case, Equation (3.22) is applied. With Avogadro's number N_A = 6.02×10^{23} 1/mol the ion density is calculated with n_{tot}^B = 1.84×10^{21} $1/m^3$.

With the necessary components summarized in Table 10, the equation can be solved to calculate R_{Seal} when values for h are selected, or based on the fitted values for R_{Seal}, h can be calculated.

Table 10: Constants used to calculate R_{Seal} and h

Parameter	Value
ε_0	8.85×10^{-12} As/Vm
ε_r	78 As/Vm
k_B	1.38×10^{-23}
T	310.15 K
D_{I+}	1.33×10^{-9} m^2/s
e_0	1.60×10^{-19} C

Inserting R_{Seal} = 4.13×10^7 Ω results in a calculated distance between cell and OECT of h = 89.6 nm. This applies for the medium used with the HEK cells where a distance between 50 nm and 200 nm was expected, depending on the device surface and a possible modification to promote cell adherence. These calculations show that the fitted values by the established equation result in realistic values for the cell to OECT distance, which is a confirmation for the accuracy of the developed model. The fitting of R_{Seal}, therefore, enables a mathematical check for the cell adhesion affinity where cells tend to adhere stronger on certain surfaces due to their modification with fibronectin, poly-D-lysine, poly-L-lysine or others. At the same time, cell-death assays can be analyzed with this method to observe the gradual increase of h with progressing cell detachment.

As a proof of concept, the data gathered with the pressing and release of a PDMS droplet on the sensing area from Chapter 3.6.2 can be used. In Table 11, the fitted R_{Seal} values are summarized.

Table 11: Fitted R_{Seal} with calculated h values indicating the distance between a PDMS droplet when pressed/released from the sensing area of an OECT

Step	R_{Seal} (Ω)	h (nm)
Baseline	0	> 100,000
Pressing 1	5.58×10^{6}	665
Pressing 2	2.04×10^{7}	37
Release 1	7.36×10^{6}	495
Release 2	1.40×10^{6}	3000
Release 3	0	> 100,000
Release 4	0	> 100,000
Release 5	0	> 100,000
Release 6	0	> 100,000

The data showed the baseline as a value without any attachment to the sensing area. By pressing the droplet to the surface, a subsequent increase in spectrum shift was measured indicating the increase in R_{Seal} which is also showing in the h values, where the increase in R_{Seal} is causing a decrease in h. The release of the droplet results in a decreasing value for R_{Seal} with a matching increase of h. This effect represents the behavior of a cell that is being released from the device surface, increasing its distance from the surface during the detachment.

3.7.4 Conclusion

The model as established in this chapter is based on already established models representing in themselves the measurement setup as well as the polymer layer. It should be noted that there is a variety of mathematical representations for polymer devices, none of which is representing OECTs for TTF measurements. The proposed mathematical model is considering setup-related parameters, as well as device-related parameters and cell-based parameters combined in one electrical equivalent circuit. The equation was used for simulations and fittings of measured data, which resulted in nice fits. For some of the data, the match was almost exact, while for other data some offsets, for example in the exact point of the frequency cutoff occurred. It was demonstrated that the measured shift in the spectra, which is caused by cell attachment/detachment can be varied in the equation solely by the cell-related parameters of the fitting function, as it should be. The fitted data was matching the results of the same cell lines as calculated with other devices (e.g. ISFETs) and can, therefore, be assumed to work as an indicator of the actual situation. Additional equations can be used to calculate the distance between the cell and the OECT out of

the fitted data. The calculated values match published data for other devices using similar cell lines, which confirms the applicability of the used model. Mathematical representations of elaborate electrochemical mechanisms as presented here, always suffer due to the complex nature of the processes and should be used carefully when interpreting data. The same has to be considered for the presented equation and its derived results. Based on the actual biological system that is measured, the data should be used as an approximation rather than as a definitive representation.

4 Discussion

4.1 A Critical View of the Obtained Results

The fabrication method introduced in Chapter 2.1 is a new way of creating PEDOT:PSS based OECTs. However, other platforms using PEDOT:PSS as transducer material have been established as well. A variety of fabrication methods were used to fabricate OECTs. There is no unified method of evaluating the device performance thus far even though one method was recently proposed (INAL et al., 2017). Judging by this state of research, it is not possible to compare the devices which are fabricated in different research groups as of now. It has to be taken into consideration that minor changes in chemical composition or post-treatment might drastically alter the characteristics of the devices.

The proposed fabrication method with chemical post-treatment is only providing a single method which has been established over the course of this thesis which might not represent the most optimized method. In addition, more methods emerge to enhance device properties while also reducing the mentioned drawbacks.

It should be noted that the established fabrication method is limited to solid substrates and cannot be transferred directly to flexible substrates. The use of an ONO stack as the passivation layer prevents the application on flexible substrates. Another passivation method would have to be established in order to transfer the process for the application on flexible substrates. For the scope of this work and the performing of *in vitro* measurements, stable solid devices enable easier handling and are therefore the method of choice.

The same applies to the size/volume of the deposited polymer. Alternatives in fabrication can provide better or more stable results or enhance the properties of the OECTs. Several chemical post-treatment methods have been established for PEDOT:PSS, as briefly described in Chapter 1.2. This only goes to underline the unique properties of PEDOT:PSS with the possibility to tailor the polymer for certain applications. As was shown, divinyl sulfone might enhance the g_m of the devices (MANTIONE et al., 2017) while a higher amount of GOPS could increase the stability in liquid (HÅKANSSON et al., 2017). Just a comparison of all additives as proposed by other groups in combination with different post-treatment would be a very complex task.

The stability of the devices was found to be excellent for the performed experiments. However, the stability of the devices is one of the most critical points of measurements with OECTs. An electronic deterioration can be seen by applying higher voltages either on drain-source or gate-source. There might be a deterioration based on repetitive measurements as well. Similarly, a deterioration might be observed by the immersion of the devices in liquid. These points are often not discussed in the literature but play a crucial role in the performance of the experiments. As it was shown in this work the electrical stability, as well as the stability of the devices in liquid, was very suitable for the performed experiments with only minor variations. It has to be considered, however, that some of the measured effects can be attributed to a deterioration process. These effects occur with a reduction of the g_m values that are measured, which leads to a shift in the working point. Intensive research would have to be conducted before devices could be used in other applications, such as implants or for cell cultures, which require a longer culturing period.

Based on the achieved results the drastic effect of the ionic strength of the measurement electrolyte on the devices was shown. By increasing the conductivity of the electrolyte the measured I_{DS} decreases. This is an effect that can also be observed when the electrolyte is added to the devices with the same conductivity, thus increasing the volume of the electrolyte. This effect is attributed to the increase of cations in the electrolyte, which causes a faster decrease in the conductivity of the PEDOT:PSS.

The used cell lines only provide an example of the capabilities of the fabricated devices. All the used cells (HL-1, HEK, and MDCK) provide a well-established and well-understood platform for cell-based research. Control measurements were integrated into all measurements to ensure that the resulting data was accurate. As shown in Chapter 3.6, the coverage of the sensing area is crucial to the measured spectra. Since the control of cellular adhesion is limited, the measured data can vary between experiments. This means that statistical analysis cannot be performed. However, this affects all measurement methods that involve random factors. It was shown before that the distance between the cell and the device surface can vary between 50 and 200 nm for HEK cells (WROBEL et al., 2008). The distance between cell and OECT can scale R_{Seal}. Also, the coverage of the sensing area by the cell is crucial since only a full coverage would result in a maximum value of R_{Seal}. The exact distance between the polymer layer and the cell would have to be confirmed optically to prove the accuracy of the calculation. Since the devices do not offer a flat surface the calculated value probably represents more of an average distance value.

The proposed mathematical model is based on the work done with a similar measurement setup using silicon-based ISFETs as performed by Susloparova et al. (SUSLOPAROVA, 2016; SUSLOPAROVA et al., 2015) and utilizes a finite length Warburg element as a representation for the PEDOT:PSS in the circuitry (DANIELSSON et al., 2004). The measurement of the transistor-transfer function for OECTs with dimensions down to single cells is shown for the first time. One of the most common representations in an electrical equivalent circuit for these devices is the modified Randles circuit as a means to describe the behavior of the devices for impedance measurements. Many efforts have been made to describe polymer devices, and several approaches have been tested. Therefore, the proposed circuit can only be seen as an approximation to describe the device in certain circumstances. The conditions for the highest accuracy of this model are single cell measurements *in vitro*. The finite length Warburg element was chosen since the events that alter the PEDOT:PSS conductivity are diffusion driven. However, many other factors may apply to the measured spectra that are not yet considered in the equation. This also comes down to the use of a simplified point-contact model as a base for the fittings. The resistance of the electrolyte in series with the reference electrode is represented by R_{el}, which is a value that has to be adjusted according to the used electrolyte. As shown in Chapter 3.2, the ionic composition of the electrolyte is an important factor to consider while measuring. R_{el} as a factor does not consider changes in the electrolyte as they may occur and can therefore only be considered as a guideline.

A similar effect might be observed with a possible deterioration since no implemented factor is regarded for the effects described in Chapter 3.3, where an I_{DS} increase was found after the immersion of the devices in liquid for three days. These effects are not well understood yet and while explanations have been proposed, such as the removal of surface-bound PSS (YAN, OKUZAKI, 2009) and the swelling of the material (BIEßMANN et al., 2018), these factors are not considered in the equation as of yet.

Also, the description of the cell is simplified by using a single resistor and capacitor as well as the junction resistance. This method can be applied for impedimetric measurements without considering other cellular properties. The proposed model cannot be used for electrically active cells to calculate the development of action potentials. Effects that electrically active cells might have on the number of ions in the cleft between cell and polymer, might alter the measured spectra. These influences of the cells are not implemented in this equation. In addition, the model was developed for the fitting of measurements for single cells and has proven to deliver results with high accuracy when compared to the measured spectra. In the case of several cells overlapping the sensing area, the model can only be applied cautiously. This may

apply to the devices with small sensing areas but is especially a problem for bigger sensing areas with sizes more than ten times larger than a single cell. In these cases, a multiplying factor might be added, or a new solution would have to be found. A similar problem occurs with the fitting of MDCK cells where the individual cells cannot be spotted directly. The exact position of the individual cells with the corresponding position of the gap junctions is crucial to the measurements and might be the reason for the fitting procedure not representing the measured curve in full detail. As it was shown before the coverage of the sensing area is one of the most important features to ensure a significant change in the spectrum between cell-free and cell-covered sensing area.

4.2 Discussion of the Results in the State of the Art and Outlook

In the present work, the fabrication, characterization, and application of PEDOT:PSS based OECTs for biological cell measurements from confluent cells down to single cells is shown for the first time. Four major steps were performed throughout the project duration:

1: Successful fabrication of OECTs by new, reliable, and reproducible techniques.
2: Detailed characterization of the developed devices concerning performance and stability to deepen the understanding of the device operation.
3: Successful application of the devices for different cell-based assays, combining the common measurement methods in a new platform.
4: Improved mathematical representation of the OECTs for detailed analysis of performed assays.

Even though many different versions of OECTs utilizing PEDOT:PSS as transducer material exist in the literature (LIN, YAN, 2012; MABECK, MALLIARAS, 2006), there is a huge amount of information to be processed to find suitable devices to perform cell-based assays. Many research groups developed devices based on former expertise or tailored to a specific need and conduct research in a specific field, which means that these devices are not fully tested in other fields or applications. At the same time, understanding only the device function, as well as the performed measurements, does not suffice for the modeling of the device behavior since this requires additional knowledge about the measurement system that is being used. The devices presented in this work show a new, reliable, adaptable, and easy way of fabrication, together with all the necessary measurements in order to use these devices for numerous cell-based applications ranging from confluent layers down to the observation of the behavior of a single cell.

Material printing was performed, and a cleanroom process was established. While the material printing offered the deposition of PEDOT:PSS on any substrate and device platform with relative ease, there was a lack of comparability and performance of the devices. Hence, the development of a more homogeneous, reliable and stable fabrication method was of paramount importance for reliable cellular assays.

The established cleanroom fabrication protocol enables the processing of thin film polymer devices without the need for specific machines since standard cleanroom equipment was used. With this new fabrication method, the contact of the polymer with

chemicals and UV light was avoided, and a maximum performance was achieved. The wafers were diced before PEDOT:PSS was deposited in order to avoid contact of the polymer layer with the protective photoresist during cutting. Otherwise, a photoresist would have had to be used as a protective layer since the water cooling during the dicing would immediately remove the polymer from the wafer surface. Since many photoresists can be used as a simple protection layer for wafer cutting, this problem might have been overcome by choosing a different protective resist. Especially for this purpose, specific photoresists were developed (TAYLOR et al., 2009) to allow for the application on top of the PEDOT:PSS layer without causing residues. It was also found that some curing temperatures have negative effects on the combination of PEDOT:PSS and photoresists not only concerning possible residues but also insolubility of the PEDOT:PSS compound as well as possible thermal degradation (VITORATOS et al., 2009). The proposed method is a very easy approach and enables a process where no damaging contact between PEDOT:PSS and any kind of photoresist has to be made. Additionally, the contact of PEDOT:PSS with high power UV light was avoided completely since the spin coating step was performed as the last step of fabrication. This was a precaution as almost all intrinsically conductive polymers have been shown to present a UV degradation effect (CRISPIN et al., 2003; DAWIDCZYK et al., 2008; MARCINIAK et al., 2004; TEHRANI et al., 2007). In the case of PEDOT:PSS the UV light induces photo-oxidation of the conjugated PEDOT chains, which in turn reduces the conjugation lengths based on sulfone group formation and the addition of carbonyl and carboxyl groups. These effects lower the conductivity of the polymer films drastically and irreversibly. It should be mentioned, that it has been shown that UV irradiation can have positive effects on the PEDOT:PSS conductivity (XING et al., 2014; YING-JIE et al., 2014) at certain wavelengths if performed for several hours. However, the increase in conductivity due to UV radiation is only happening at specific wavelengths with other wavelengths having negative effects on the polymer. When fabricating the devices, the damage would be way bigger than the minimal increase in conductivity. Furthermore, the exposure of the wafers for several hours is not a viable option for the reported, relatively small conductivity increase.

The established process can be used for any solid substrate and as a result, the PEDOT:PSS only had to be in contact with acetone in order to remove the sacrificial layer. Research showed no impact of acetone on PEDOT:PSS, on the contrary, acetone was found to slightly increase the conductivity in PEDOT:PSS layers (XIA, OUYANG, 2012). It was found that the image reversal resist (AR-U-4030) was very suitable for this task.

The fabricated devices showed uniformity within the wafer concerning the electrical properties in a way that the 16 channels on each chip were comparable to each other with only minor variations in properties (Chapter 3.3). This was also achieved for different batches of wafers where a high level of reproducibility was attained. Different sensing area sizes were chosen for the OECTs. The IDE configuration of the first devices was already established with various finger sizes and areas. To simplify the approach and gather a higher yield in fabricated devices, only two sizes were combined on a single wafer, with 20×20 μm^2 being the smallest tested area. While the area could be reduced further, the finger size of 5 µm would have to be altered, or a completely different design would have been necessary. The parameters, in this case, were chosen based on the reliability of the fabrication. 5 µm finger sizes with 5 µm distance granted a yield where no defects occurred. The size of the sensing area and more importantly, the volume of the polymer layer are the determining factor for the device performance. As already stated briefly in previous chapters, the g_m of the devices is increased with an increased volume of the PEDOT:PSS as can be seen from the performed characterization measurements. Keeping the fabrication protocol the same throughout this thesis, the thickness changes were minimal, but the changes in sensitivity and frequency response showed exactly the mentioned effects. It was observed that the biggest sensing areas resulted in the highest g_m values, but the smallest sensing areas showed the best frequency response with the highest cutoff frequency at the half-power point. This effect can be explained by the faster dedoping of the polymer layer due to its lower volume (KHODAGHOLY et al., 2013). Basically, the penetration and binding of cations can happen in a faster way all over the polymer layer with a lower amount of ions needed to switch off the OECTs. This results in a higher speed as measured by the frequency response. At the same time, a decrease in I_{DS} is observed which causes a decrease in g_m. In addition, the working point is also shifting with the area of the polymer layer, with bigger areas having a working point in higher V_{GS} ranges and smaller devices showing the maximum g_m at V_{GS} = 0 V. Using this effect, device characteristics can be manipulated by simply adjusting the volume of the OECTs (RIVNAY et al., 2013).

In the current configuration, the IDE fingers are always fully covered with the polymer in a way that a shift during the fabrication steps would not affect the configuration. Other electrode configurations have been tested already (KHODAGHOLY et al., 2013) with the polymer only touching the electrodes on the sides of the sensing area, making the sensing area completely transparent, as opposed to the IDE configuration. In theory, any electrode configuration could be realized with the OECTs following the described protocol. It is difficult to compare the different possibilities regarding the

source and drain electrodes and estimate their impact on the device behavior. Some electrodes would show advantages for optical assays or the use of the devices as implants. The use of IDEs in this particular case was based on the properties set by the electrode structures as it occurs with these devices. As already established, the properties of the OECT depend on the volume of the deposited PEDOT:PSS and the cutoff frequency depends on the thickness of the polymer layer. The desirable devices should, therefore, show a thin polymer layer with big lengths and widths in order to obtain the best electrical properties. While the volume of the polymer layer can stay constant, the contacting of the layer may change. When the polymer layer is contacted only on the sides by “stripes” of electrodes instead of being contacted by IDEs, the distance between the electrodes is increased. This results in a higher resistance based on the resistivity of the transducer material. Therefore, in order to reduce the distance between the electrodes while keeping the area of the polymer constant, an IDE configuration can be used. An additional advantage is the consistency of the gold electrode area in contact with the polymer in this fabrication method, where the alignment of the PEDOT:PSS does not change the contacted electrode area, even if a misalignment would occur.

A chemical post-treatment was chosen to modify the OECTs towards higher conductivity and stability. Many different chemical modifications can be performed which alter the properties of the devices (DIMITRIEV et al., 2009; MANTIONE et al., 2017; OUYANG, 2013). The established protocol is offering a high g_m and sufficient stability due to the application of EG. However, other chemical compounds might offer even higher achievable g_m values with the same configuration (MANTIONE et al., 2017). EG was used due to the easy implementation of the treatment into the fabrication process.

The vast amount of publications does not allow for an efficient comparison between already established devices, based on device dimensions, fabrication methods, and used dopants. Based on these differences varying voltages and g_m values are used, which often lack dedicated and detailed examinations of the used devices concerning their stability. The stability of PEDOT:PSS based OECTs has to be examined exactly under the experimental conditions in order to ensure the accuracy of the measurements. Degradation occurs when in contact with liquids, ambient air, UV radiation, heat and of course due to mechanical stress etc. (FRIEDEL et al., 2009; HÅKANSSON et al., 2017; HUANG et al., 2003; KAWANO et al., 2006; NILSSON et al., 2002; TEHRANI et al., 2007; VITORATOS et al., 2009).

Devices were characterized in different ways to evaluate their performances and capabilities for the intended measurements. Every gathered result was valuable in order to identify the assays that can be performed on the developed platform.

Overall there are huge advantages of PEDOT:PSS based devices over other established platforms with their tunable, high g_m and cutoff frequency, their low noise and drift, cost-effective fabrication, and transparency.

In the scope of this thesis, the g_m, as well as the frequency response, were the major points of interest. The g_m is commonly used to describe the sensitivity of field-effect based devices and describes the sensitivity based on the difference between output and input signal while the cutoff frequency gives an idea of how the devices would perform in detecting high-frequency action potentials.

A huge advantage of the OECTs is the possibility to measure cellular action potentials as well as cell attachment/detachment due to their characteristics (HEMPEL et al., 2017b). When measuring action potentials of cells, a high cutoff frequency with a low noise level are crucial (YAO et al., 2015). The presented OECTs showed clear signals for the measured HL-1 cells, but with the slow signal components covered by the noise of the system. This effect can be attributed to the relatively large sensing areas of the devices that were used for these experiments. Since many adherent cells were localized at the sensing area, the measurements were a combination of surface effects and cellular signals as a mixed output (CLAYCOMB et al., 1998). This could be avoided by reducing the sensing area size as it would reduce the measured interference caused by the cells drastically. This, of course, could be applied to all electrogenic cells as long as they exhibit action potentials that are showing higher amplitudes than the noise level of the OECTs. PEDOT:PSS has been shown to benefit neuronal outgrowth (CELLOT et al., 2016) and shows clear capabilities to perform such measurements (GKOUPIDENIS et al., 2015). What separates the shown OECTs from other platforms is the combination of two measurement principles, where not only action potentials can be measured but also impedimetric data can be recorded. The impedimetric measurements showed the capability of the devices to detect cells based on their attachment and detachment. Bigger sensing areas with very high g_m can deliver impedance data about cell populations as done with migration studies (LO et al., 1995; WEGENER et al., 2000; XIAO et al., 2002). Of course, the gathered data involves all the adherent cells on the polymer layer and the effect that single cells and their proliferation have on the output signal cannot be determined reliably. This is where a major limitation of planar gold electrodes can be overcome. Gold electrodes suffer from an increase in impedance when the size is reduced, that is why nanofabrication is used to increase the surface to volume ratio in order to allow for

miniaturization (SCHRÖPER et al., 2008). In this thesis, it was shown how it is possible to miniaturize the OECTs sensing areas, without decreasing the sensitivity in a novel way. The developed devices even surpass the sensitivity values of traditional silicon-based devices with similar gate size (KHODAGHOLY et al., 2013; SUSLOPAROVA et al., 2015). While the measurement of cell populations also inhibit important data, as was shown in Chapter 3.6, the reduction down to single cell level inherits many interesting parameters that are extremely relevant. The amount of publications for OECTs for single cell analysis is scarce, and the presented devices show a means to fill this gap. The observance of MDCK cells on the devices showed the possibility to measure membrane effects on a very small scale other than previously shown, where the sensing area sizes were exceeding the shown devices by far (RAMUZ et al., 2014; RAMUZ et al., 2015; TRIA et al., 2013).

So what is the advantage of the analysis on a single cell level? To this day single cell analysis is performed with optical assays even though micro- and nanofabricated devices showed the potential to replace or aid these kinds of assays (ANDERSSON, VAN DEN BERG, 2004; WANG, BODOVITZ, 2010). At the same time, the OECT platform allows for the measurement of impedance data as well as the detection of changes in extracellular field potentials. Single-cell analysis is researched as a promising tool for many possible applications that need the high-resolution detection of single cells. Single-cell impedance measurements have already shown their value for the detection of drugs and pharmaceutical compounds (YE et al., 2003), detection of infections (VERMA, SINGH, 2003; YANG et al., 2006), environmental detection (GILCHRIST et al., 2005), and toxicity assays (GIAEVER, KEESE, 1992). The leading method for these measurements is the ECIS method, which has shown applications to differ between various cell types (RIGAUD et al., 1996) since the cellular impedance directly correlates to the mechanical, physical and biochemical functions of the measured cell (CHUANG et al., 2009). This allows for the differentiation between different cell types, as was shown with cancer cells (QIAO et al., 2010). At low frequencies, the conductance of cells is typically very low which makes the cell behave like a non-conductor (OREN et al., 2004) so that the majority of the current flows around the cell. Therefore, when measured at high frequencies where cells become current conductors, the electrical properties can be examined.

With the OECTs developed in this thesis, a major step towards single-cell impedance experiments for cultured cells was made. The presented experiments already show the possibility to not only detect the impedimetric behavior of a single cell but also the detection of cell-cell interactions was possible, as shown with the MDCK cells on a very small scale.

Another strong point can be found in the proposed mathematical model of the OECTs in combination with a cell and the readout system. The mathematical representation that is mainly found in publications is the modified Randles circuit to fit the impedance data measured with PEDOT:PSS based OECTs (INAL et al., 2017; KARIMULLAH et al., 2013; VYAS, WANG, 2010). However, these circuits lack in many points as an accurate description of the devices. In many cases, the diffusion element (Warburg element) in the circuitry is simply used to shape the curve of the measured data in a specific way which can be seen as a 45-degree angle in the data of the impedance measurements in its simplest iteration. The model as it is presented in this work has not been published so far with all the shown components in order to obtain information not only about the cell attachment and detachment, but also offers the possibility to calculate the cell distance and the cell shape (SUSLOPAROVA et al., 2015). The combination of the modified circuit for OECT sensors offers the possibility to be easily adjusted for several materials or material combinations by exchanging the impedances.

For future applications, the design of the devices could be adjusted to allow for easier implementation of optical assays. By increasing the distance between the gold-electrode fingers, fluorescent signals could be observed better. The devices could be used more intensively in investigating cellular action potential signals on single cell level, since the OECTs should be able to allow these experiments. It could be possible to detect the change of ionic composition in the cleft between the cell and the polymer layer, when the cell membrane is covering the sensing area. This would open new ways of detection and it would have to be investigated if even small amounts of ions could be used. With an experiment individual ion channels and their drug-induced opening and closing could be investigated.

The data presented in this thesis can be used to tailor OECTs towards specific applications or as a manual to investigate the effect of measurement parameters on the results. The established fabrication method can easily be used by research groups and the data should enable a better understanding of PEDOT:PSS based devices in general.

5 Supplementary Information

Supplementary 1: Protocol for the cleanroom fabrication steps for the OECTs

Wafer cleaning

Step	System / Process	Material	Parameters
1	Spin rinse dryer	DI water	700 rpm, 3 min; DI; 2000 rpm; 4 min; N_2
2	Piranha solution	H_2SO_4 95%; H_2O_2 30%	115 °C; 10 min; add 20-40 ml H_2O_2 to solution
3	Quick dump rinser	DI water	3 min
4	Spin rinse dryer	DI water	700 rpm, 3 min; DI; 2000 rpm; 4 min; N_2
5	Plasma stripper	O_2	40% O_2; 350 W, 5 min

Lithography of contact lines

Step	System / Process	Material	Parameters
6	Spin coater	AR-U 4030	3 ml / 7 sec, 100 rpm; 60 sec, 2000 rpm
7	Hotplate		85 °C; 2 min
8			10 min cooldown
9	Mask aligner	Mask 1	10 sec; 6 mW; hard contact mode
10	Hotplate		115 °C; 5 min
11			10 min cooldown
12	Mask aligner, exposure		25 sec; 6 mW
13	Developer bench	AR 300-26; DI	1:3; ca. 10 sec.
14	Spin dryer		3000 rpm, 30 sec
15	Microscopic control of structures	Microscope	

Metallization

Step	System / Process	Material	Parameters
	Plasma stripper	O_2	40% O_2; 50 W, 0,5 min
16	Thermal evaporator	Ti, Au	**Ti**: 100 Å, 2 Å/s, power 47%, **Au**: 3000 Å, 5 Å/s, power 51%

Lift-off

Step	System / Process	Material	Parameters
17	Ultrasound	Acetone beaker 1 Acetone beaker 2	5 min; 60 W 1 min; fresh acetone
18	Cleaning bench	Isopropanol	5 min
19	Quick dump rinser	DI water	2 min

20	Spin rinse dryer	DI water	700 rpm, 3 min; DI; 2000 rpm; 4 min; N_2
21	Plasma stripper	O_2	40% O_2; 350 W, 5 min

Passivation

Step	System / Process	Material	Parameters
22	Plasma-enhanced chemical vapor deposition	Si_xN_y SiO_2	**SiN**: 150 nm 9 min 30 sec; HF 20 sec. 43 W; LF 6 sec. 43 W; 650 mTorr; 20 sccm SiH_4; 20 sccm NH_3; 800 sccm N_2 **SiO2:** 100 nm / 200 nm 2 min 30 sec / 5 min; HF 20 W; 1000 mTorr; 20 sccm SiH_4; 20 sccm N_2O; 800 sccm N_2

Lithography for opening sensing area and contact pads

Step	System / Process	Material	Parameters
23	Spin coater	AR-U 4030	3 ml / 7 sec, 100 rpm; 60 sec, 2000 rpm
24	Hotplate		85 °C; 2 min
25			10 min cool down
26	Mask aligner	Mask 2	10 sec; 6 mW; hard contact mode
27	Hotplate		115 °C; 5 min
28			10 min cool down
29	Mask aligner, exposure		25 sec; 6 mW
30	Developer bench	AR 300-26; DI	1:3; ca. 10 sec.
31	Spin dryer		3000 rpm, 30 sec
32	Microscopic control of structures	Microscope	

Contact opening

Step	System / Process	Material	Parameters
33	Plasma stripper	O_2	40% O_2; 50 W, 0,5min
34	Reactive ion etching		CF_4 25 sccm, O_2 3,1 sccm, 13,3 Pa, 100 W, 10 min
35	Microscopic control of structures	Microscope	
36	Cleaning bench	Acetone; Isopropanol	5 min each
37	Cleaning bench	DI water	5 min
38	Spin rinse dryer	DI water	700 rpm, 3 min; DI; 2000 rpm; 4 min; N_2
39	Microscopic control of structures	Microscope	

Wafer cutting

Step	System / Process	Material	Parameters
40	Spin coater	AZ-520D	5 ml; 3000 rpm; 60 sec
41	Hotplate		170 °C; 1 min
42	Cutting foil		
43	Wafer saw	GA 851	5 mm/s y1 = 40 mm; y2 = 39 mm; z1 =80 µm; z2 =2 mm
44	Cleaning bench	Acetone; Isopropanol, DI.	5 min each

Sacrificial layer

Step	System / Process	Material	Parameters
45	Spin coater	AR-U 4030	3 ml / 7 sec, 100 rpm; 60 sec, 2000 rpm
46	Hotplate		85 °C; 2 min
47			10 min cool down
48	Mask aligner	Mask 2	10 sec; 6 mW; hard contact mode
49	Hotplate		115 °C; 5 min
50			10 min cool down
51	Mask aligner, exposure		25 sec; 6 mW
52	Developer bench	AR 300-26; DI	1:3; ca. 10 sec.
53	Spin dryer		3000 rpm, 30 sec
54	Microscopic control of structures	Microscope	

PEDOT:PSS spin coating

Step	System / Process	Material	Parameters
55	Plasma stripper	O_2	40% O_2; 250 W, 0,5 min
56	Spin coater	PEDOT:PSS	3 ml, 100 rpm; 5 sec, 3000 rpm 30 sec
57	Hotplate		50 °C, 5 min
58	Ultrasound	Acetone	5 min; 40 W
59	Cleaning bench	N_2	2 min

Supplementary 2: Media used for the different cells with their detailed contents

Cells	Medium	Distributor	Content	Distributor
HL-1	Claycomb medium	51800C Merck, Germany	10 % fetal calf serum	P30-3702 PAN Biotech, Germany
			1 % penecillin/streptomycin	P06-07100 PAN Biotech, Germany
			1 % norepinephrine	N5785 Merck, Germany
			1 % L-glutamine	P04-80100 PAN Biotech, Germany
HEK 293	M10 minimal essential medium	P04-08250 PAN Biotech, Germany	10 % fetal calf serum	P30-3702 PAN Biotech, Germany
			1 % penecillin/streptomycin	P06-07100 PAN Biotech, Germany
			1 % L-glutamine	P04-80100 PAN Biotech, Germany
			1 % non-essential amino acids	P08-32100 PAN Biotech, Germany
			1 % Paneticin G418	P06-17200 PAN Biotech, Germany
MDCK	M10 minimal essential medium	P04-08250 PAN Biotech, Germany	10 % fetal calf serum	P30-3702 PAN Biotech, Germany
			1 % penecillin/streptomycin	P06-07100 PAN Biotech, Germany
			1 % L-glutamine	P04-80100 PAN Biotech, Germany
			1 % non-essential amino acids	P08-32100 PAN Biotech, Germany

6 References

1. Andersson H, van den Berg A (2004) Microtechnologies and nanotechnologies for single-cell analysis. Current opinion in biotechnology 15:44-49
2. Asphahani F, Zhang M (2007) Cellular impedance biosensors for drug screening and toxin detection. Analyst 132:835-841
3. Bakkum DJ, Frey U, Radivojevic M, Russell TL, Müller J, Fiscella M, Takahashi H, Hierlemann A (2013) Tracking axonal action potential propagation on a high-density microelectrode array across hundreds of sites. Nature communications 4:2181
4. Balasubramanian K, Burghard M (2006) Biosensors based on carbon nanotubes. Analytical and bioanalytical chemistry 385:452-468
5. Berggren M, Richter-Dahlfors A (2007) Organic bioelectronics. Advanced Materials 19:3201-3213
6. Bergveld P (1972) Development, operation, and application of the ion-sensitive field-effect transistor as a tool for electrophysiology. IEEE Transactions on Biomedical Engineering:342-351
7. Bergveld P, Wiersma J, Meertens H (1976) Extracellular potential recordings by means of a field effect transistor without gate metal, called OSFET. IEEE Transactions on Biomedical Engineering:136-144
8. Bernards DA, Macaya DJ, Nikolou M, DeFranco JA, Takamatsu S, Malliaras GG (2008a) Enzymatic sensing with organic electrochemical transistors. Journal of Materials Chemistry 18:116-120
9. Bernards DA, Owens RM, Malliaras GG (2008b) Organic semiconductors in sensor applications, Springer).
10. Bießmann L, Kreuzer LP, Widmann T, Hohn N, Moulin J-F, Muller-Buschbaum P (2018) Monitoring the Swelling Behavior of PEDOT: PSS Electrodes under High Humidity Conditions. ACS applied materials & interfaces
11. Bobacka J, Lewenstam A, Ivaska A (2000) Electrochemical impedance spectroscopy of oxidized poly (3, 4-ethylenedioxythiophene) film electrodes in aqueous solutions. J Electroanal Chem 489:17-27
12. Bolin MH, Svennersten K, Nilsson D, Sawatdee A, Jager EW, Richter-Dahlfors A, Berggren M (2009) Active Control of Epithelial Cell-Density Gradients Grown Along the Channel of an Organic Electrochemical Transistor. Advanced Materials 21:4379-4382
13. Cellot G, Lagonegro P, Tarabella G, Scaini D, Fabbri F, Iannotta S, Prato M, Salviati G, Ballerini L (2016) PEDOT: PSS interfaces support the development of neuronal synaptic networks with reduced neuroglia response in vitro. Frontiers in neuroscience 9:521
14. Chuang C-H, Wei C-H, Hsu Y-M, Huang H-S, Hsiao F-B (2009). Impedance sensing of bladder cancer cells based on a single-cell-based DEP microchip. Paper presented at: Sensors, 2009 IEEE (IEEE).
15. Claycomb WC, Lanson NA, Stallworth BS, Egeland DB, Delcarpio JB, Bahinski A, Izzo NJ (1998) HL-1 cells: a cardiac muscle cell line that contracts and retains phenotypic characteristics of the adult cardiomyocyte. Proceedings of the National Academy of Sciences 95:2979-2984

16. Crispin X, Marciniak S, Osikowicz W, Zotti G, van der Gon A, Louwet F, Fahlman M, Groenendaal L, De Schryver F, Salaneck WR (2003) Conductivity, morphology, interfacial chemistry, and stability of poly (3, 4-ethylene dioxythiophene)–poly (styrene sulfonate): A photoelectron spectroscopy study. Journal of polymer science Part B: Polymer physics 41:2561-2583
17. Cunningham B, Lin B, Qiu J, Li P, Pepper J, Hugh B (2002) A plastic colorimetric resonant optical biosensor for multiparallel detection of label-free biochemical interactions. Sensors and Actuators B: Chemical 85:219-226
18. Danielsson P, Bobacka J, Ivaska A (2004) Electrochemical synthesis and characterization of poly (3, 4-ethylenedioxythiophene) in ionic liquids with bulky organic anions. J Solid State Electrochem 8:809-817
19. Dawidczyk TJ, Walton MD, Jang W-S, Grunlan JC (2008) Layer-by-layer assembly of UV-resistant poly (3, 4-ethylenedioxythiophene) thin films. Langmuir 24:8314-8318
20. de Izarra A, Park S, Lee J, Lansac Y, Jang YH (2018) Ionic Liquid Designed for PEDOT: PSS Conductivity Enhancement. Journal of the American Chemical Society 140:5375-5384
21. Deng Y, Zhang Y, Sun S, Wang Z, Wang M, Yu B, Czajkowsky DM, Liu B, Li Y, Wei W (2014) An integrated microfluidic chip system for single-cell secretion profiling of rare circulating tumor cells. Scientific reports 4:7499
22. Dimitriev O, Grinko D, Noskov YV, Ogurtsov N, Pud A (2009) PEDOT: PSS films—Effect of organic solvent additives and annealing on the film conductivity. Synthetic metals 159:2237-2239
23. Ding L, Du D, Zhang X, Ju H (2008) Trends in cell-based electrochemical biosensors. Current medicinal chemistry 15:3160-3170
24. Döbbelin M, Marcilla R, Salsamendi M, Pozo-Gonzalo C, Carrasco PM, Pomposo JA, Mecerreyes D (2007) Influence of ionic liquids on the electrical conductivity and morphology of PEDOT: PSS films. Chemistry of materials 19:2147-2149
25. Donahue MJ, Williamson A, Strakosas X, Friedlein JT, McLeod RR, Gleskova H, Malliaras GG (2018) High-Performance Vertical Organic Electrochemical Transistors. Advanced Materials 30:1705031
26. Doris SE, Pierre A, Street RA (2018) Dynamic and Tunable Threshold Voltage in Organic Electrochemical Transistors. Advanced Materials 30:1706757
27. Duan X, Gao R, Xie P, Cohen-Karni T, Qing Q, Choe HS, Tian B, Jiang X, Lieber CM (2012) Intracellular recordings of action potentials by an extracellular nanoscale field-effect transistor. Nature nanotechnology 7:174
28. Elschner A, Loevenich W, Eiling A, Bayley J (2012) ITO Alternative: solution deposited Clevios TM PEDOT: PSS for transparent conductive applications. Heraeus trade article
29. Fan B, Mei X, Ouyang J (2008) Significant conductivity enhancement of conductive poly (3, 4-ethylenedioxythiophene): poly (styrenesulfonate) films by adding anionic surfactants into polymer solution. Macromolecules 41:5971-5973
30. Fanigliulo A, Accossato P, Adami M, Lanzi M, Martinoia S, Paddeu S, Parodi M, Rossi A, Sartore M, Grattarola M (1996) Comparison between a LAPS and an FET-based sensor for cell-metabolism detection. Sensors and Actuators B: Chemical 32:41-48

31. Finn A, Alderman J, Schweizer J (2002) Towards an Optimization of FET-Based Bio-Sensors. European Cells and Materials 4:21-23
32. Franke F, Jäckel D, Dragas J, Müller J, Radivojevic M, Bakkum D, Hierlemann A (2012) High-density microelectrode array recordings and real-time spike sorting for closed-loop experiments: an emerging technology to study neural plasticity. Frontiers in neural circuits 6:105
33. Friedel B, Keivanidis PE, Brenner TJ, Abrusci A, McNeill CR, Friend RH, Greenham NC (2009) Effects of layer thickness and annealing of PEDOT: PSS layers in organic photodetectors. Macromolecules 42:6741-6747
34. Giaever I, Keese C (1992) Toxic? Cells can tell. Chemtech 22:116-125
35. Gilchrist KH, Giovangrandi L, Whittington RH, Kovacs GT (2005) Sensitivity of cell-based biosensors to environmental variables. Biosensors and Bioelectronics 20:1397-1406
36. Gkoupidenis P, Schaefer N, Garlan B, Malliaras GG (2015) Neuromorphic functions in PEDOT: PSS organic electrochemical transistors. Advanced Materials 27:7176-7180
37. Greco F, Zucca A, Taccola S, Menciassi A, Fujie T, Haniuda H, Takeoka S, Dario P, Mattoli V (2011) Ultra-thin conductive free-standing PEDOT/PSS nanofilms. Soft Matter 7:10642-10650
38. Gualandi I, Scavetta E, Mariani F, Tonelli D, Tessarolo M, Fraboni B (2018) All poly (3, 4-ethylenedioxythiophene) organic electrochemical transistor to amplify amperometric signals. Electrochimica Acta 268:476-483
39. Håkansson A, Han S, Wang S, Lu J, Braun S, Fahlman M, Berggren M, Crispin X, Fabiano S (2017) Effect of (3-glycidyloxypropyl) trimethoxysilane (GOPS) on the electrical properties of PEDOT: PSS films. Journal of Polymer Science Part B: Polymer Physics 55:814-820
40. Hempel F, Law JK-Y, Nguyen TC, Munief W, Lu X, Pachauri V, Susloparova A, Vu XT, Ingebrandt S (2017a) PEDOT: PSS organic electrochemical transistor arrays for extracellular electrophysiological sensing of cardiac cells. Biosens Bioelectron 93:132-138
41. Hempel F, Law JK-Y, Nguyen TC, Munief W, Lu X, Pachauri V, Susloparova A, Vu XT, Ingebrandt S (2017b) PEDOT: PSS organic electrochemical transistor arrays for extracellular electrophysiological sensing of cardiac cells. Biosensors and Bioelectronics 93:132-138
42. Hodgkin AL, Huxley AF (1952) A quantitative description of membrane current and its application to conduction and excitation in nerve. The Journal of physiology 117:500-544
43. Hong J, Kandasamy K, Marimuthu M, Choi CS, Kim S (2011) Electrical cell-substrate impedance sensing as a non-invasive tool for cancer cell study. Analyst 136:237-245
44. Huang J, Miller P, De Mello J, De Mello A, Bradley D (2003) Influence of thermal treatment on the conductivity and morphology of PEDOT/PSS films. Synthetic Metals 139:569-572
45. Inal S, Malliaras GG, Rivnay J (2017) Benchmarking organic mixed conductors for transistors. Nature communications 8:1767
46. Ingebrandt S, Yeung C-K, Krause M, Offenhäusser A (2001) Cardiomyocyte-transistor-hybrids for sensor application. Biosensors and Bioelectronics 16:565-570

47. Ingebrandt S, Yeung C, Staab W, Zetterer T, Offenhäusser A (2003) Backside contacted field effect transistor array for extracellular signal recording. Biosensors and bioelectronics 18:429-435
48. Ingebrandt S, Yeung C-K, Krause M, Offenhäusser A (2005) Neuron–transistor coupling: interpretation of individual extracellular recorded signals. European biophysics journal 34:144-154
49. Ito S, Yeh F-C, Hiolski E, Rydygier P, Gunning DE, Hottowy P, Timme N, Litke AM, Beggs JM (2014) Large-scale, high-resolution multielectrode-array recording depicts functional network differences of cortical and hippocampal cultures. PloS one 9:e105324
50. Jäckel D, Bakkum DJ, Russell TL, Müller J, Radivojevic M, Frey U, Franke F, Hierlemann A (2017) Combination of High-density Microelectrode Array and Patch Clamp Recordings to Enable Studies of Multisynaptic Integration. Scientific reports 7:978
51. Jönsson S, Birgerson J, Crispin X, Greczynski G, Osikowicz W, Van Der Gon AD, Salaneck WR, Fahlman M (2003) The effects of solvents on the morphology and sheet resistance in poly (3, 4-ethylenedioxythiophene)–polystyrenesulfonic acid (PEDOT–PSS) films. Synthetic Metals 139:1-10
52. Karimullah AS, Cumming DR, Riehle M, Gadegaard N (2013) Development of a conducting polymer cell impedance sensor. Sensors and Actuators B: Chemical 176:667-674
53. Kawano K, Pacios R, Poplavskyy D, Nelson J, Bradley DD, Durrant JR (2006) Degradation of organic solar cells due to air exposure. Solar energy materials and solar cells 90:3520-3530
54. Kergoat L, Piro B, Berggren M, Horowitz G, Pham M-C (2012) Advances in organic transistor-based biosensors: from organic electrochemical transistors to electrolyte-gated organic field-effect transistors. Analytical and bioanalytical chemistry 402:1813-1826
55. Khodagholy D, Rivnay J, Sessolo M, Gurfinkel M, Leleux P, Jimison LH, Stavrinidou E, Herve T, Sanaur S, Owens RM (2013) High transconductance organic electrochemical transistors. Nature communications 4
56. Kim D-J, Lee N-E, Park J-S, Park I-J, Kim J-G, Cho HJ (2010) Organic electrochemical transistor based immunosensor for prostate specific antigen (PSA) detection using gold nanoparticles for signal amplification. Biosensors and Bioelectronics 25:2477-2482
57. Kim JH, Jang J, Lee D-Y, Zin W-C (2002) Thickness and composition dependence of the glass transition temperature in thin homogeneous polymer blend films. Macromolecules 35:311-313
58. Kuş M, Okur S (2009) Electrical characterization of PEDOT: PSS beyond humidity saturation. Sensors and Actuators B: Chemical 143:177-181
59. Lan S, Veiseh M, Zhang M (2005) Surface modification of silicon and gold-patterned silicon surfaces for improved biocompatibility and cell patterning selectivity. Biosensors and Bioelectronics 20:1697-1708
60. Lang U, Müller E, Naujoks N, Dual J (2009) Microscopical investigations of PEDOT: PSS thin films. Advanced Functional Materials 19:1215-1220
61. Lee C-S, Kim SK, Kim M (2009) Ion-sensitive field-effect transistor for biological sensing. Sensors 9:7111-7131
62. Lei Y, Mulchandani P, Chen W, Wang J, Mulchandani A (2004) Whole cell–enzyme hybrid amperometric biosensor for direct determination of

organophosphorous nerve agents with p-nitrophenyl substituent. Biotechnology and bioengineering 85:706-713
63. Li J, Li R, Zheng L, Wang Y, Xie S, Lin J (2016). Detection of mast cell secretion by using surface enhanced Raman scattering. Paper presented at: Optics in Health Care and Biomedical Optics VII (International Society for Optics and Photonics).
64. Lim FJ, Ananthanarayanan K, Luther J, Ho GW (2012) Influence of a novel fluorosurfactant modified PEDOT: PSS hole transport layer on the performance of inverted organic solar cells. Journal of Materials Chemistry 22:25057-25064
65. Lin P, Yan F, Yu J, Chan HL, Yang M (2010) The application of organic electrochemical transistors in cell-based biosensors. Advanced Materials 22:3655-3660
66. Lin P, Luo X, Hsing I, Yan F (2011) Organic electrochemical transistors integrated in flexible microfluidic systems and used for label-free DNA sensing. Advanced Materials 23:4035-4040
67. Lin P, Yan F (2012) Organic thin-film transistors for chemical and biological sensing. Advanced materials 24:34-51
68. Lipomi DJ, Lee JA, Vosgueritchian M, Tee BC-K, Bolander JA, Bao Z (2012) Electronic properties of transparent conductive films of PEDOT: PSS on stretchable substrates. Chemistry of Materials 24:373-382
69. Liu Q, Wang P (2009) Cell-based biosensors: principles and applications, Artech House).
70. Lo C-M, Keese CR, Giaever I (1995) Impedance analysis of MDCK cells measured by electric cell-substrate impedance sensing. Biophysical journal 69:2800-2807
71. Lowe CR (2007) Overview of biosensor and bioarray technologies. Handbook of Biosensors and Biochips
72. Lucarelli F, Tombelli S, Minunni M, Marrazza G, Mascini M (2008) Electrochemical and piezoelectric DNA biosensors for hybridisation detection. analytica chimica acta 609:139-159
73. Luo J, Billep D, Waechtler T, Otto T, Toader M, Gordan O, Sheremet E, Martin J, Hietschold M, Zahn DR (2013) Enhancement of the thermoelectric properties of PEDOT: PSS thin films by post-treatment. Journal of Materials Chemistry A 1:7576-7583
74. Mabeck JT, Malliaras GG (2006) Chemical and biological sensors based on organic thin-film transistors. Analytical and bioanalytical chemistry 384:343-353
75. Macchia E, Ghittorelli M, Torricelli F, Torsi L (2017). Organic electrochemical transistor immuno-sensor operating at the femto-molar limit of detection. Paper presented at: Advances in Sensors and Interfaces (IWASI), 2017 7th IEEE International Workshop on (IEEE).
76. Mantione D, del Agua I, Schaafsma W, ElMahmoudy M, Uguz I, Sanchez-Sanchez A, Sardón H, Castro B, Malliaras GG, Mecerreyes D (2017) Low temperature cross-linking of PEDOT: PSS films using divinylsulfone. ACS Applied Materials & Interfaces
77. Marciniak S, Crispin X, Uvdal K, Trzcinski M, Birgerson J, Groenendaal L, Louwet F, Salaneck WR (2004) Light induced damage in poly (3, 4-ethylenedioxythiophene) and its derivatives studied by photoelectron spectroscopy. Synthetic metals 141:67-73

78. Müller J, Ballini M, Livi P, Chen Y, Radivojevic M, Shadmani A, Viswam V, Jones IL, Fiscella M, Diggelmann R (2015) High-resolution CMOS MEA platform to study neurons at subcellular, cellular, and network levels. Lab on a Chip 15:2767-2780
79. Nardes AM, Kemerink M, De Kok M, Vinken E, Maturova K, Janssen R (2008) Conductivity, work function, and environmental stability of PEDOT: PSS thin films treated with sorbitol. Organic electronics 9:727-734
80. Niles AL, Moravec RA, Hesselberth PE, Scurria MA, Daily WJ, Riss TL (2007) A homogeneous assay to measure live and dead cells in the same sample by detecting different protease markers. Analytical biochemistry 366:197-206
81. Nilsson D, Kugler T, Svensson P-O, Berggren M (2002) An all-organic sensor–transistor based on a novel electrochemical transducer concept printed electrochemical sensors on paper. Sensors and Actuators B: Chemical 86:193-197
82. Normann RA, Warren DJ, Ammermuller J, Fernandez E, Guillory S (2001) High-resolution spatio-temporal mapping of visual pathways using multi-electrode arrays. Vision research 41:1261-1275
83. Obien MEJ, Deligkaris K, Bullmann T, Bakkum DJ, Frey U (2015) Revealing neuronal function through microelectrode array recordings. Frontiers in neuroscience 8:423
84. Offenhäusser A, Sprössler C, Matsuzawa M, Knoll W (1997) Field-effect transistor array for monitoring electrical activity from mammalian neurons in culture. Biosensors and Bioelectronics 12:819-826
85. Offenhäusser A, Knoll W (2001) Cell-transistor hybrid systems and their potential applications. TRENDS in Biotechnology 19:62-66
86. Oren Y, Freger V, Linder C (2004) Highly conductive ordered heterogeneous ion-exchange membranes. Journal of membrane science 239:17-26
87. Ouyang J, Guo T-F, Yang Y, Higuchi H, Yoshioka M, Nagatsuka T (2002) High-performance, flexible polymer light-emitting diodes fabricated by a continuous polymer coating process. Advanced Materials 14:915
88. Ouyang J, Xu Q, Chu C-W, Yang Y, Li G, Shinar J (2004) On the mechanism of conductivity enhancement in poly (3, 4-ethylenedioxythiophene): poly (styrene sulfonate) film through solvent treatment. Polymer 45:8443-8450
89. Ouyang J (2013) “Secondary doping” methods to significantly enhance the conductivity of PEDOT: PSS for its application as transparent electrode of optoelectronic devices. Displays 34:423-436
90. Pabst M, Wrobel G, Ingebrandt S, Sommerhage F, Offenhäusser A (2007) Solution of the Poisson-Nernst-Planck equations in the cell-substrate interface. The European Physical Journal E 24:1-8
91. Pancrazio J, Whelan J, Borkholder D, Ma W, Stenger D (1999) Development and application of cell-based biosensors. Annals of biomedical engineering 27:697-711
92. Perumal V, Hashim U (2014) Advances in biosensors: Principle, architecture and applications. Journal of Applied Biomedicine 12:1-15
93. Pine J (1980) Recording action potentials from cultured neurons with extracellular microcircuit electrodes. Journal of neuroscience methods 2:19-31
94. Price DT, Rahman ARA, Bhansali S (2009) Design rule for optimization of microelectrodes used in electric cell-substrate impedance sensing (ECIS). Biosensors and Bioelectronics 24:2071-2076

95. Qiao G, Duan W, Chatwin C, Sinclair A, Wang W (2010). Electrical properties of breast cancer cells from impedance measurement of cell suspensions. Paper presented at: Journal of Physics: conference series (IOP Publishing).
96. Ramuz M, Hama A, Huerta M, Rivnay J, Leleux P, Owens RM (2014) Combined optical and electronic sensing of epithelial cells using planar organic transistors. Advanced Materials 26:7083-7090
97. Ramuz M, Hama A, Rivnay J, Leleux P, Owens R (2015) Monitoring of cell layer coverage and differentiation with the organic electrochemical transistor. Journal of Materials Chemistry B 3:5971-5977
98. Regehr WG, Pine J, Cohan CS, Mischke MD, Tank DW (1989) Sealing cultured invertebrate neurons to embedded dish electrodes facilitates long-term stimulation and recording. Journal of neuroscience methods 30:91-106
99. Rigaud B, Morucci J-P, Chauveau N (1996) Bioelectrical impedance techniques in medicine. Part I: Bioimpedance measurement. Second section: impedance spectrometry. Critical reviews in biomedical engineering 24:257-351
100. Rivnay J, Leleux P, Sessolo M, Khodagholy D, Hervé T, Fiocchi M, Malliaras GG (2013) Organic electrochemical transistors with maximum transconductance at zero gate bias. Advanced Materials 25:7010-7014
101. Rivnay J, Leleux P, Ferro M, Sessolo M, Williamson A, Koutsouras DA, Khodagholy D, Ramuz M, Strakosas X, Owens RM (2015) High-performance transistors for bioelectronics through tuning of channel thickness. Science advances 1:e1400251
102. Schäfer S, Eick S, Hofmann B, Dufaux T, Stockmann R, Wrobel G, Offenhäusser A, Ingebrandt S (2009) Time-dependent observation of individual cellular binding events to field-effect transistors. Biosensors and bioelectronics 24:1201-1208
103. Schröper F, Brüggemann D, Mourzina Y, Wolfrum B, Offenhäusser A, Mayer D (2008) Analyzing the electroactive surface of gold nanopillars by electrochemical methods for electrode miniaturization. Electrochimica acta 53:6265-6272
104. Shim NY, Bernards DA, Macaya DJ, DeFranco JA, Nikolou M, Owens RM, Malliaras GG (2009) All-plastic electrochemical transistor for glucose sensing using a ferrocene mediator. Sensors 9:9896-9902
105. Spira ME, Hai A (2013) Multi-electrode array technologies for neuroscience and cardiology. Nature nanotechnology 8:83
106. Susloparova A, Koppenhöfer D, Law J, Vu X, Ingebrandt S (2015) Electrical cell-substrate impedance sensing with field-effect transistors is able to unravel cellular adhesion and detachment processes on a single cell level. Lab on a Chip 15:668-679
107. Susloparova A (2016) Impedimetric detection of anticancer drug action on individual tumor cells using field-effect transistor devices.
108. Tang H, Yan F, Lin P, Xu J, Chan HL (2011) Highly sensitive glucose biosensors based on organic electrochemical transistors using platinum gate electrodes modified with enzyme and nanomaterials. Advanced Functional Materials 21:2264-2272
109. Tao W, Lin P, Hu J, Ke S, Song J, Zeng X (2017) A sensitive DNA sensor based on an organic electrochemical transistor using a peptide nucleic acid-modified nanoporous gold gate electrode. RSC Advances 7:52118-52124

110. Taylor PG, Lee JK, Zakhidov AA, Chatzichristidi M, Fong HH, DeFranco JA, Malliaras GG, Ober CK (2009) Orthogonal patterning of PEDOT: PSS for organic electronics using hydrofluoroether solvents. Advanced Materials 21:2314-2317
111. Tehrani P, Kanciurzewska A, Crispin X, Robinson ND, Fahlman M, Berggren M (2007) The effect of pH on the electrochemical over-oxidation in PEDOT: PSS films. Solid State Ionics 177:3521-3527
112. Teichler A, Perelaer J, Schubert US (2013) Inkjet printing of organic electronics–comparison of deposition techniques and state-of-the-art developments. Journal of Materials Chemistry C 1:1910-1925
113. Thedinga E, Kob A, Holst H, Keuer A, Drechsler S, Niendorf R, Baumann W, Freund I, Lehmann M, Ehret R (2007) Online monitoring of cell metabolism for studying pharmacodynamic effects. Toxicology and applied pharmacology 220:33-44
114. Tian B, Cohen-Karni T, Qing Q, Duan X, Xie P, Lieber CM (2010) Three-dimensional, flexible nanoscale field-effect transistors as localized bioprobes. Science 329:830-834
115. Tria S, Jimison LH, Hama A, Bongo M, Owens RM (2013) Sensing of EGTA mediated barrier tissue disruption with an organic transistor. Biosensors 3:44-57
116. Verma N, Singh M (2003) A disposable microbial based biosensor for quality control in milk. Biosensors and bioelectronics 18:1219-1224
117. Vitoratos E, Sakkopoulos S, Dalas E, Paliatsas N, Karageorgopoulos D, Petraki F, Kennou S, Choulis SA (2009) Thermal degradation mechanisms of PEDOT: PSS. Organic Electronics 10:61-66
118. Vosgueritchian M, Lipomi DJ, Bao Z (2012) Highly conductive and transparent PEDOT: PSS films with a fluorosurfactant for stretchable and flexible transparent electrodes. Advanced functional materials 22:421-428
119. Vyas RN, Wang B (2010) Electrochemical analysis of conducting polymer thin films. International journal of molecular sciences 11:1956-1972
120. Wagenaar DA, Pine J, Potter SM (2004) Effective parameters for stimulation of dissociated cultures using multi-electrode arrays. Journal of neuroscience methods 138:27-37
121. Wang D, Bodovitz S (2010) Single cell analysis: the new frontier in ‘omics’. Trends in biotechnology 28:281-290
122. Wang P, Xu G, Qin L, Xu Y, Li Y, Li R (2005a) Cell-based biosensors and its application in biomedicine. Sensors and Actuators B: Chemical 108:576-584
123. Wang P, Xu G, Qin L, Xu Y, Li Y, Li R (2005b) Cell-based biosensors and its application in biomedicine. Sensors and Actuators B: Chemical 108:576-584
124. Wegener J, Keese CR, Giaever I (2000) Electric cell–substrate impedance sensing (ECIS) as a noninvasive means to monitor the kinetics of cell spreading to artificial surfaces. Experimental cell research 259:158-166
125. Wrobel G, Seifert R, Ingebrandt S, Enderlein J, Ecken H, Baumann A, Kaupp UB, Offenhäusser A (2005) Cell-transistor coupling: Investigation of potassium currents recorded with p-and n-channel FETs. Biophysical journal 89:3628-3638
126. Wrobel G, Höller M, Ingebrandt S, Dieluweit S, Sommerhage F, Bochem HP, Offenhäusser A (2008) Transmission electron microscopy study of the cell–sensor interface. Journal of The Royal Society Interface 5:213-222

127. Xia Y, Ouyang J (2009) Salt-induced charge screening and significant conductivity enhancement of conducting poly (3, 4-ethylenedioxythiophene): poly (styrenesulfonate). Macromolecules 42:4141-4147
128. Xia Y, Ouyang J (2010a) Significant conductivity enhancement of conductive poly (3, 4-ethylenedioxythiophene): poly (styrenesulfonate) films through a treatment with organic carboxylic acids and inorganic acids. ACS applied materials & interfaces 2:474-483
129. Xia Y, Ouyang J (2010b) Anion effect on salt-induced conductivity enhancement of poly (3, 4-ethylenedioxythiophene): poly (styrenesulfonate) films. Organic Electronics 11:1129-1135
130. Xia Y, Zhang H, Ouyang J (2010) Highly conductive PEDOT: PSS films prepared through a treatment with zwitterions and their application in polymer photovoltaic cells. Journal of Materials Chemistry 20:9740-9747
131. Xia Y, Ouyang J (2011) PEDOT: PSS films with significantly enhanced conductivities induced by preferential solvation with cosolvents and their application in polymer photovoltaic cells. Journal of Materials Chemistry 21:4927-4936
132. Xia Y, Ouyang J (2012) Highly conductive PEDOT: PSS films prepared through a treatment with geminal diols or amphiphilic fluoro compounds. Organic Electronics 13:1785-1792
133. Xiao C, Lachance B, Sunahara G, Luong JH (2002) An In-Depth Analysis of Electric Cell− Substrate Impedance Sensing To Study the Attachment and Spreading of Mammalian Cells. Analytical Chemistry 74:1333-1339
134. Xie X, Stüben D, Berner Z, Albers J, Hintsche R, Jantzen E (2004) Development of an ultramicroelectrode arrays (UMEAs) sensor for trace heavy metal measurement in water. Sensors and actuators B: Chemical 97:168-173
135. Xing Y, Qian M, Wang G, Zhang G, Guo D, Wu J (2014) UV irradiation induced conductivity improvement in poly (3, 4-ethylenedioxythiophene): poly (styrenesulfonate) film. Science China Technological Sciences 57:44-48
136. Xiong C, Qu H, Chen W, Zhang L, Qiu L, Zheng L, Xia F (2017) Real-time detection of Cu (II) with PEDOT: PSS based organic electrochemical transistors. Science China Chemistry 60:1205-1211
137. Xu Y, Xie X, Duan Y, Wang L, Cheng Z, Cheng J (2016) A review of impedance measurements of whole cells. Biosensors and Bioelectronics 77:824-836
138. Yan H, Okuzaki H (2009) Effect of solvent on PEDOT/PSS nanometer-scaled thin films: XPS and STEM/AFM studies. Synthetic Metals 159:2225-2228
139. Yang Y, Wang J, Yu G, Niu F, He P (2006) Design and preliminary evaluation of a portable device for the measurement of bioimpedance spectroscopy. Physiological Measurement 27:1293
140. Yao C, Li Q, Guo J, Yan F, Hsing I-M (2015) Rigid and flexible organic electrochemical transistor arrays for monitoring action potentials from electrogenic cells. Advanced healthcare materials 4:528-533
141. Ye L, Martin TA, Parr C, Harrison GM, Mansel RE, Jiang WG (2003) Biphasic effects of 17-β-estradiol on expression of occludin and transendothelial resistance and paracellular permeability in human vascular endothelial cells. Journal of cellular physiology 196:362-369

142. Ying-Jie X, Min-Fang Q, Deng-Zhu G, Geng-Min Z (2014) Increased work function in PEDOT: PSS film under ultraviolet irradiation. Chinese Physics B 23:038504
143. Zare RN, Kim S (2010) Microfluidic platforms for single-cell analysis. Annual review of biomedical engineering 12:187-201
144. Zhao Y, Inayat S, Dikin D, Singer J, Ruoff R, Troy J (2008) Patch clamp technique: review of the current state of the art and potential contributions from nanoengineering. Proceedings of the Institution of Mechanical Engineers, Part N: Journal of Nanoengineering and Nanosystems 222:1-11
145. Ziegler C (2000) Cell-based biosensors. Fresenius' journal of analytical chemistry 366:552-559

7 Publications

Felix Hempel, Thanh Chien Nguyen, Jessica Ka Yan Law, and Sven Ingebrandt. The influence of medium conductivity on ECIS measurements with field-effect transistor arrays. Physica Status Solidi (a)212.6 (2015): 1260-1265

Jessica Ka Yan Law, Anna Susloparova, Xuan Thang Vu, Xiao Zhou, Felix Hempel, Bin Qu, Markus Hoth, Sven Ingebrandt. Human T cells monitored by impedance spectrometry using field-effect transistor arrays: A novel tool for single-cell adhesion and migration studies. Biosensors and Bioelectronics, 67 (2015): 170-176

Felix Hempel, Jessica Ka Yan Law, Thanh Chien Nguyen, Walid Munief, Xiaoling Lu, Vivek Pachauri, Xuan Thang Vu and Sven Ingebrandt. PEDOT: PSS organic electrochemical transistor arrays for extracellular electrophysiological sensing of cardiac cells. Biosensors and Bioelectronics (2016)

Felix Hempel, Jessica Ka Yan Law, Sven Ingebrandt. Transistor-Based Impedimetric Monitoring of Single Cells. (2018) Bioanalytical Reviews. Springer, Berlin, Heidelberg

Walid-Madhat Munief, Florian Heib, Felix Hempel, Xiaoling Lu, Miriam Schwartz, Vivek Pachauri, Rolf Hempelmann, Michael Schmitt and Sven Ingebrandt. Silane Deposition via Gas-Phase Evaporation and High-Resolution Surface Characterization of the Ultrathin Siloxane Coatings. Langmuir 34, 35 (2018): 10217-10229

Walid-Madhat Munief, Xiaoling Lu, Tobias Teucke, Jannick Wilhelm, Anette Britz, Felix Hempel, Ruben Lanche, Miriam Schwartz, Jessica Ka Yan Law, Samuel Grandthyll, Frank Müller, Jens-Uwe Neurohr, Karin Jacobs, Michael Schmitt, Vivek Pachauri, Rolf Hempelmann, Sven Ingebrandt. Reduced graphene oxide biosensor platform for the detection of NT-proBNP biomarker in its clinical range. Biosensors and Bioelectronics, 126 (2019): 136-142

8 Acknowledgments

I want to thank my family for all the support that I received over the years.
My mother and father showed a lot of interest and a sympathetic ear, all the joy and pride that I felt based on my academic achievements helped me a lot to focus and continue with my work. Without the continuous support of my mother, I would have never achieved as much as I did, and I will always be grateful for that.
I want to thank my brother for his support and willingness to listen to my results, the good ones and the bad ones. He was a special support for me during my time at the university.

I want to dedicate this work to my wife and daughter without whom this whole thesis would be meaningless. I cannot express the amount of gratitude my wife deserves. I am certain that our discussions and exchange about my work had a huge impact on this thesis. Without her understanding for this process, this thesis would have surely never been finished. The influence my daughter had on this thesis cannot be expressed, and I hope that one day she will read these lines and know that without her this work probably would have never been finished.

In addition, I want to express my gratitude to everybody that showed their support during my time in research. I would like to specifically thank Sven and his whole research group. Sven took me in as a student and I really enjoyed working with him and his team. Sven was a special mentor to me throughout my studies. From the Biomedical Signaling Group I would like to specifically thank Ruben and Walid for their support.
A special thanks goes to Markus, who was willing to take me as a Ph.D. student into his group and gave me the opportunity to make this thesis happen.